Impact of Weak Interfaces and Layered Rock Properties on Hydraulic Fracture Containment and Height Growth

by

Qiao Lu

B.S. Petroleum Engineering, University of Wyoming, 2014

M.S. Petroleum Engineering, University of Pittsburgh, 2016

Submitted to the Graduate Faculty of the

Swanson School of Engineering in partial fulfillment

of the requirements for the degree of

Doctor of Philosophy

University of Pittsburgh

2022

UNIVERSITY OF PITTSBURGH

SWANSON SCHOOL OF ENGINEERING

This dissertation was presented

by

Qiao Lu

It was defended on

March 23, 2022

and approved by

Brigham, John C, PhD, Associate Professor, Civil and Environmental Engineering

Enick, Robert M, PhD, Professor, Chemical and Petroleum Engineering

Lin, Jeen-Shang, PhD, Associate Professor, Civil and Environmental Engineering

Dissertation Director: Bunger, Andrew, P, PhD, Associate Professor, Civil and Environmental Engineering, Chemical and Petroleum Engineering

Impact of Weak Interfaces and Layered Rock Properties on Hydraulic Fracture Containment and Height Growth

Qiao, Lu, PhD

University of Pittsburgh, 2022

Hydraulic fracturing and waterflooding are both widely applied methods for improving the recovery of oil and gas resources. These methods have increasing commonality because many waterfloods are being carried out at high enough pressure to generate hydraulic fractures. Therefore, a common goal is to connect hydrocarbon-bearing layers to the well but impose pressure limits that avoid breaking through into water-bearing layers or otherwise non-producing layers adjacent to it. However, when using classical but highly simplified height growth models, the pressure limits can be far too conservative, leading to much lower recovery rates and inefficient use of resources invested in developing producing reservoirs.

In this context, this research contributes experiments and numerical simulations on the role of stresses, weak interfaces, and mechanical properties of a three-layer system in promoting containment or height growth from a central reservoir to neighboring barrier layers. In all cases, the experiments and simulations agree that the pressure required to induce substantial height growth exceeds the stress applied to the barrier layers and is far above classical predictions. When the reservoir layer is softer than the barriers, the containment is sustained to even higher pressures than for layers with similar material properties. Besides, the experiments show that permeability of the barrier layer can enable containment at higher pressures than at comparable cases with impermeable materials, but with a strikingly more sudden transition to uncontrolled height growth when instability is eventually induced.

In a complementary effort, lattice-type Distinct Element Method (DEM) simulation results show a high level of consistency with experimental lab data. By leading to increased confidence in the model, this comparison suggests it could provide an efficient and sufficiently accurate platform for providing the key link between the laboratory results and the applicability of the work in field-scale operations. Thus, this research comprises a uniquely important step forward in elucidating essential mechanisms that govern hydraulic fracture containment and height growth in layered reservoirs.

Table of Contents

List of Tables

List of Figures

Preface

Looking back these years, I will never say this is an easy journey, but finally, I make it here. In the meantime, I clearly realize that so many people should take credit for helping me reach this achievement.

First of all, I want to thank my advisor Dr. Andrew Bunger, who gives me enormous help and instructions during this journey. Undoubtedly, his profound knowledge and inspiring suggestion are among the most important factors that led me to this achievement. More than that, my admiration for him comes from not only his specialty but also his charisma. His gentleness and open-mindedness will deeply affect my future life and career.

Next, I want to thank all my committee professors Dr. Brigham, John C, Dr. Enick, Robert M, and Dr. Lin, Jeen-Shang, Dr. Luis Vallejo (retired), who are willing to spend their valuable time sitting around the table and providing their specialized suggestions. Besides, special credit should be granted to Mr. Hager Charles Clemenes for providing essential laboratory support and services. Meanwhile, I want to thank all my team colleagues who also gives me nonnegligible help and suggestions to finish the research. It is such a pleasant experience to study and work with you guys all. I also want to acknowledge the research sponsor party, Chevron Energy Technology Company. Especially, I want to thank Mr. Amr El-Fayoumi, Mr. Jose Adachi, and Mr. Karim Zaki for providing significant outline guidance and coordination. Besides, it is an honor to work with you during my summer internship.

Finally, I will never forget the people I should be grateful for most. My parents give me unconditional trust and endless support. And my girlfriend, Meng Zhao, who is by my side during this journey and willing to take a new role as my wife for the rest of my life.

Back to this dissertation, besides the information and knowledge covered in this paper, a related EP3D modeling analysis tool can be accessed at:

https://d-scholarship.pitt.edu/view/divisions/sch=5Feng=5Fcivilenvironmental/2022.html

Nomenclature

σ_r	Reservoir stress
σ_b	Barrier stress
σ_v	Vertical stress
$\Delta\sigma = \sigma_b - \sigma_r$	Confining stress contrast
P_f	Injection wellbore pressure
$P_{net} = P_f - \sigma_r$	Net wellbore pressure
P_{fc}	Critical wellbore pressure
$P_{net,c}$	Critical net wellbore pressure
E_r	The Young’s Modulus of the reservoir layer
E_b	The Young’s Modulus of the barrier layer
$e = E_r / E_b$	Elasticity/Young's modulus ratio
Q_0	Injection flow rate
μ	Injection flow viscosity
l	Lateral fracture length
h	Half fracture height
H	Half reservoir layer thickness
$\Delta h = h - H$	Fracture height growth
$\lambda = \Delta h / H$	Relative height
W	Fracture aperture/width
W_0	The maximum fracture width within the reservoir layer

W_1	The maximum fracture width within the barrier layer
$\omega = W_0 / W_1$	Fracture width ratio

1.0 Overview and Motivation

1.1 Overview

Hydraulic fracturing has been widely applied in unconventional oil and gas production to enhance the recovery rate for over seven decades [Montgomery & Smith 2010]. A successful fracture treatment can effectively increase the overall conductivity of the reservoir by making high conductivity flow channels that connect to the well. In a related application, hydraulic fracture development can also be a by-product during waterflooding treatments, which is also widely applied to enhance oil and gas recovery in conventional and unconventional reservoirs by sweeping hydrocarbons from injector to producer well(s). The generation of the hydraulic fracture may be beneficial or harmful to waterflooding performance, depending on the nature of the various layers.

For various scenarios, a common goal of hydraulic fracturing is to connect hydrocarbon-bearing layers to the well without breaking through into water-bearing layers or otherwise non-producing layers adjacent to it. Thus motivated, a variety of experiments [e.g., El Rabaa, 1987; Teufel & Clark,1984; Jeffrey & Bunger, 2009; Ning et al. 2018] and modeling efforts [Simonson et al. 1978; Gu & Siebrits, 2008; Zhang et al., 2017] have been undertaken, aiming at accurately predicting fracture behavior within multiple formation layers. In this context, the unique contribution of this dissertation research is to experimentally consider hydraulic fracture vertical growing in a system with three layers separated by weak horizontal interfaces and where the layers are comprised of different materials, including both permeable and impermeable materials. Also unique to this work, fully coupled numerical simulations are carried out in conjunction with the experiments, providing a wider range of parametric study than is possible in the lab and providing experimental validation of the numerical simulation method. Therefore, the research is a uniquely important step forward to elucidate essential mechanisms that govern hydraulic fracture containment and height growth in layered reservoirs, providing valuable guidance for future study.

1.2 Motivation

Traditionally in waterflooding, the wellbore injection pressure is limited below the level that would cause fracturing [Bennion et al., 1998]. In contrast, many (if not most) waterfloods are now carried out above fracturing pressure [Noirot et al., 2003; de Souza et al., 2005; Hustedt et al., 2008], but with injection pressure limitations set to avoid fracture vertically growing into adjacent water-bearing formation(s). However, when using classical but highly simplified height growth models, the pressure limits can be far too conservative, leading to much lower recovery rates and inefficient use of resources invested in developing producing reservoirs. Thus, it is essential to investigate the critical factors and criteria affecting vertical fracture propagation.

In hydraulic fracturing for reservoir stimulation, classical models that overpredict height growth can also be problematic. On the one hand, they can lead to overly conservative design in cases where the desire is to avoid growth into water-bearing or non-producing layers. On the other hand, when the desire is to generate height growth to connect productive layers, the design could fall short of identifying the requirements for generating the targeting height growth.

Therefore, the current research is primarily motivated by a demand to predict hydraulic fracture height growth for safe and effective reservoir stimulation and waterflooding operations. However, in the meantime, we should also realize that the main challenge for investigating the vertical fracture propagation in layered formation is the interplay among multiple physical processes. For instance, fracture growth is impacted by factors such as in-situ stresses, mechanical and hydraulic properties of the layers, and strength of interfaces between layers, leading to coupled processes involving fracture-induced stresses, fluid flow, and inelastic deformation, especially on pre-existing discontinuities. All of this leads to a complex, multi-physics problem.

Past simulations and experiments show, as an overall trend, that fracture height growth is controlled, to leading order, by stress contrast between the reservoir and the bounding layers [e.g., Simonson et al. 1978; Warpinski & Teufel 1987; Nolte & Smith 1981; Nolte & Economides 2000]. Laboratory experiments for planar, zero toughness hydraulic fractures [Jeffrey & Bunger 2009; Wu et al., 2008] illustrate the profound difference between height growth in the presence of low stress and high stress in the bounding layers. While the stress contrasts may often determine the leading behavior of the height growth, other parameters, such as interlayer contrasts in stiffness (i.e., Young's modulus, e.g., [Simonson et al., 1978]), permeability [Quinn, 1994; de Pater & Dong, 2009], and weak bedding planes [Daneshy, 1978, 2009] can also have a strong impact on hydraulic fracture behavior.

Notably, past studies have made it clear that weak bedding planes can significantly limit height growth and introduce a range of possible outcomes that include crossing, blunting, or T-shaped growth [Thiercelin et al., 1987]. Relevant research includes model predictions [Daneshy, 1978], field observations [Warpinski & Teufel, 1987], and laboratory experiments [El-Rabaa, 1987; Teufel & Clark, 1984]. However, only the recent work of [Xing et al., 2018a, b] considers sharp stress contrasts between layers combined with the impact of weak interfaces between the layers. Even so, this prior work was limited to stress ranges that are low compared to field-relevant values. Besides, it considered only impermeable materials with a fixed combination of elastic properties for the reservoir and adjacent layers.

While a detailed literature review will be saved for Chapter 2, the summary is that several important knowledge gaps remain about how the hydraulic fracture will behave within a multi-layer formation. More specifically, it is not known how to promote or limit vertical fracture propagation by considering the effect of weak bedding interfaces coupling with stress contrast, elasticity contrast, and permeable materials. By filling this knowledge gap, we can show a way forward to substantially improve the recovery efficiency from waterflooding and reservoir stimulation through the application of pressure limits that more fully consider the mechanisms controlling fracture containment and height growth in layered reservoirs.

2.0 Background and Objectives

Hydraulic fracture height growth prediction is one of the most essential and challenging topics that has been pursued by both industry and academia. Many of the hydraulic fracture numerical simulation challenges come from the complex fracture modeling configurations, with the presence of material heterogeneities and complex pre-existing and fracture-induced stress field. In some cases, the fracture geometries can be approximated by simplified models. For example, Khristianovich–Zheltov–Geertsma–De Klerk (KGD) model [Khristianovis & Zheltov, 1955] is the earliest one-dimensional fracture model (Figure 2-1a), which assumes that a hydraulic fracture propagates under plane strain conditions. In another word, the KGD model is valid when the fracture height H is much larger than the fracture length l. This model is usually applied to analyze cases with uniform material properties in a vertical direction or deal with fracture initiation and early-stage fracture propagation problems.

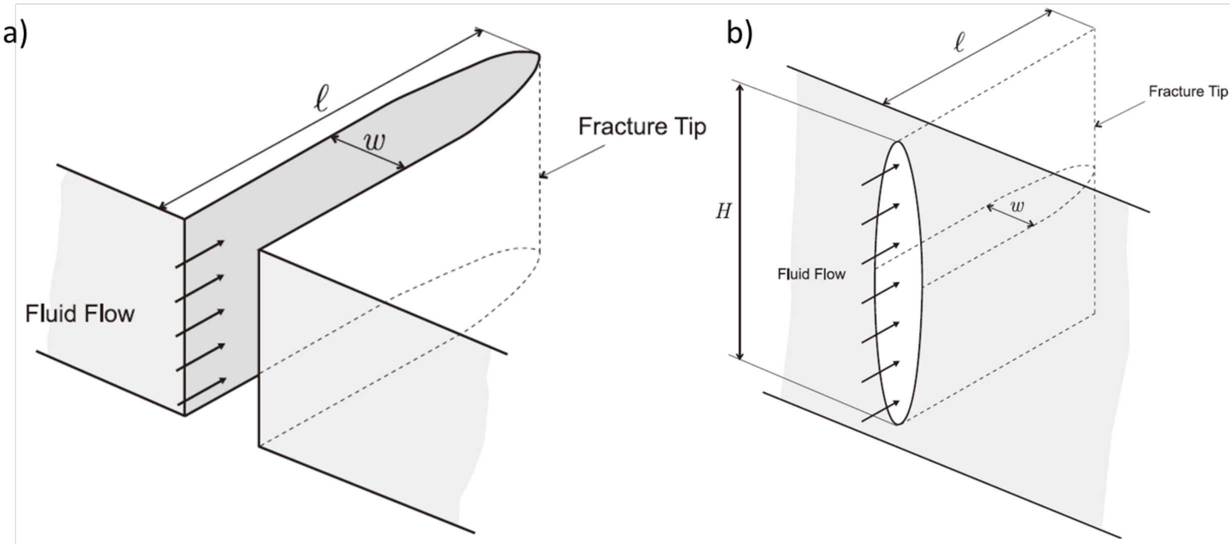

Figure 2-1. The plot shows the sketch of the a) KGD model and b) PKN model [Adachi et al., 2007].

In comparison with the KGD model, the Perkins - Kern - Nordgren (PKN) model [Perkins & Kern, 1961, Nordgren, 1972] was developed to solve the case when the geometry is better approximated by a planar hydraulic fracture with constant fracture height H, and the crack length l is much larger than the height (Figure 2-1b). For the PKN model, each vertical cross-section is assumed to be elliptical. In both KGD and PKN models, only horizontal flow q_x is considered.

Perhaps the most defining characteristic of these two classical models is that they assume the presence of multiple layers formation, with hydraulic fracture growth in a central reservoir layer that is bounded by perfectly-effective barrier layers laying above and below the reservoir layer. When the barrier layers completely prevent vertical hydraulic fracture growth, the height H is constant, and the case is considered to be ideally one of "containment" (Figure 2-2a). However, perfect containment is an idealization. In actuality, the fracture will typically penetrate into the barrier layers, generating so-called "height growth" (Figure 2-2b). Additionally, a third option is known as "T-shape growth" [El-Rabaa, 1987; Warpinski & Teufel, 1987] (Figure 2-2c) or "offset penetration" [Fu et al., 2018, 2019], but realized under conditions of relatively low vertical stress and will not be covered in the current research. The low vertical stress case can be referred from [Xing et al. 2018a].

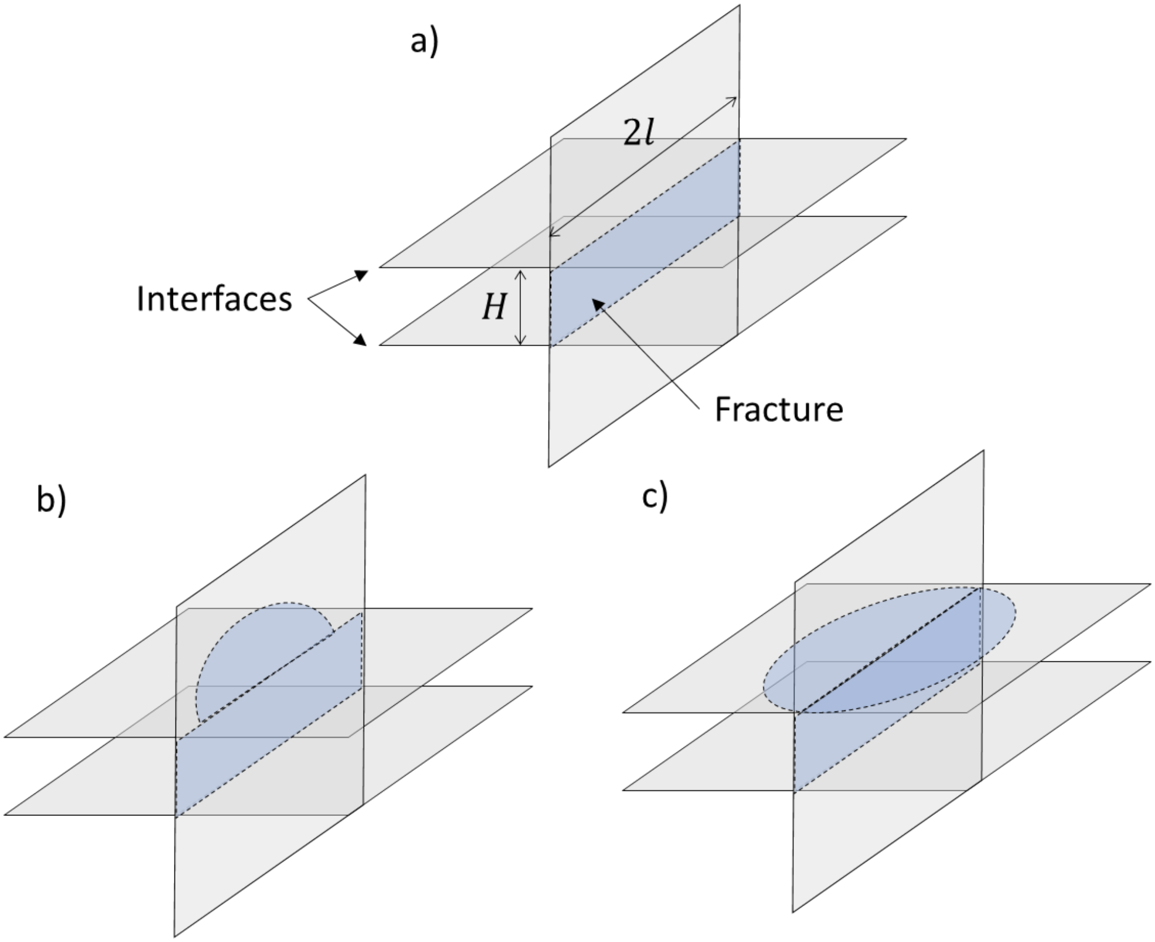

Figure 2-2. The sketches of different fracture geometry, a) containment, b) height growth, c) T-shape.

2.1 Equilibrium Height Growth Model

As a starting point for mechanical modeling of hydraulic fracture height growth, [Simonson et al. 1978] provides a fracture mechanics solution relevant to fracture propagation in a material with uniform mechanical properties but with layers under different stresses loadings (Figure 2-3a). This solution is developed under the assumption that the fluid pressure is uniform throughout the vertical cross-section, which is relevant when fluid flow is only in the horizontal direction. It also assumes a local plane strain condition, which is valid when the hydraulic fracture length dramatically exceeds its height [Adachi & Peirce, 2008]. Thus, Figure 2-3a shows a plane strain cross-section through the height of a fracture extending in and out of the page. Furthermore, it is assumed that the pressure varies along the hydraulic fracture length (in and out of the page in Figure 2-3a) but not in the height direction. Hence, the solution considers a uniformly pressurized crack initialized from the middle layer and gradually growing in height into adjacent layers (i.e., with vertical growth velocity much smaller than horizontal growth velocity). For convenience, we will name the middle layer as the reservoir layer, while the symmetric upper and lower layers are called barrier layers. The horizontal boundary stress applied on the barrier layers is σ_b. In contrast, the stress applied on the reservoir layer is σ_r, which satisfies

$$\sigma_r \leq \sigma_b$$

The reservoir layer has a height of H while the total crack length is h. Using readily-available solutions from Linear Elastic Fracture Mechanics (LEFM) [Tata et al., 2000], Simonson et al.[1978] compute the stress intensity factor, K_I, for this configuration. Then, to consider an upper bound on height growth, they specify the case when the fracture toughness of the rock (which resists height growth) is vanishingly negligible, that is, K_{IC} = 0. Under these conditions, the relationship between inner crack pressure P_f and crack length is

$$\frac{P_f - \sigma_r}{\sigma_b - \sigma_r} = -\frac{2}{\pi}\sin^{-1}\left(\frac{H}{h}\right) + 1 \qquad \text{Eq.2-1}$$

The dimensionless group on the left side of the equal sign only relates to the in-situ stresses (or boundary stresses in the case of laboratory experiments) and the inner pressure P_f.

A key result often used as a guide to determining pressure limits when height growth needs to be mitigated is that the fracture will not be dramatically growing into the barrier layers until the dimensionless stress group $\frac{P_f-\sigma_r}{\sigma_b-\sigma_r}$ exceeds 0.3~0.4. Specifically, the fracture will be first under a stable period, when the dimensionless stress group $\frac{P_f-\sigma_r}{\sigma_b-\sigma_r}$ is less than the critical value, leading to the fracture height *h* remaining relatively close to the (fixed) reservoir height *H*. Once the value is larger than the critical value, the fracture will transfer into a non-stable status and hence is predicted to rapidly grow with any small additional increase in the fluid pressure (Figure 2-3b).

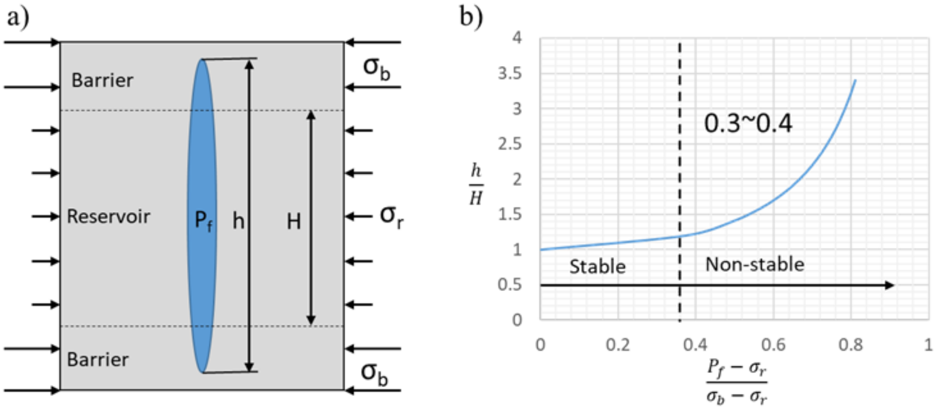

Figure 2-3 a) Internal crack propagation in a homogenous material with high barrier stress. b) Height growth will be in a stable period when the dimensionless group is less than 0.3~0.4 and the non-stable status once it exceeds that value.

Besides the pressure limit to avoid substantial height growth, it should be pointed out that only the stresses perpendicular to the crack are involved in the solution of [Simonson et al., 1978]. In other words, the impact of vertical stress (stress parallel to the crack while perpendicular to the interfaces), which we define here as σ_v, is considered irrelevant to the fracture growth. So, if one were to create a parametric space defining a region of containment from a region of significant height growth, with the y-axis of the space having some dimensionless group that depends on the vertical stress, one would get a plot that has a line perpendicular to the x-axis. For a homogeneous, brittle elastic material strictly following quasi-static linear elastic fracture mechanics theory, this independence of the height growth from the vertical stress could be valid. However, both field observation [Warpinski & Teufel, 1987] and laboratory studies [Daneshy, 1978; El-Rabaa, 1987; Teufel & Clark, 1984] have proved that the solution of [Simonson et al., 1978] is not sufficient to explain the situation encountered in a discontinuous medium. For instance, the appearance of the weak interface(s) that is/are perpendicular or oblique to the crack growth direction can increase the pressure needed to induce a fracture height growth due to the energy dissipated as the crack interacts with the interface. Besides, as mentioned above, weak interface(s) can also lead to alternative fracture geometry like blunting or T-shaped growth. All these uncertainties are mainly dependent on the interface strength [Renshaw & Pollard, 1995] and the vertical stress.

2.2 Pseudo 3D and Planar 3D Models

To better understand the fracture height growth, the so-called Pseudo-3D (P3D) model was first introduced in the 1980s [Settari & Cleary, 1982; Palmer & Carroll, 1983a,b] as an extension of the PKN model, developed to simulate the hydraulic fracture height growth. Like the PKN model, the P3D model is valid when fracture grows with a small height to length ratio (Figure 2-4a). In this case, the vertical fluid flux q_z is negligible compared to horizontal fluid flux q_x. While there exist a multiplicity of variations and implementations, it suffices as a summary to consider them to have in common that they leverage the length to height ratio and negligible vertical fluid velocity to justify treating every fracture cross-section as plane strain with uniform fluid pressure. Therefore, each section can have a computed height based on an equilibrium height growth model like Eq. (2-1) or some comparable generalization.

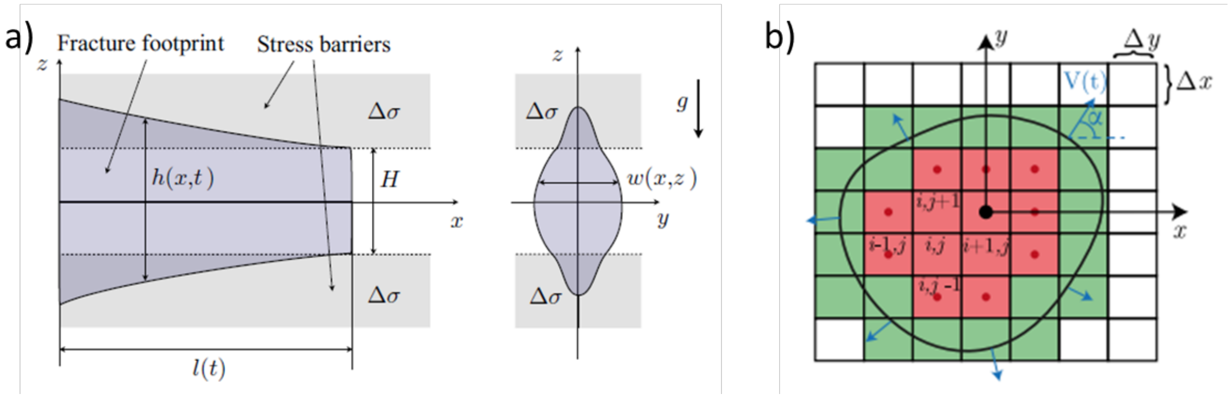

Figure 2-4. a) The footprint (left) and planar vertical cross-section (right) of the P3D model [from Dontsov & Peirce, 2015]. b) Schematic of the finite discretization of the fracture in the PL3D model [from Zia & Lecampion, 2020].

Although computationally efficient, the drawback of the P3D model can rapidly lose accuracy once the assumptions are not met. Coupled with the fact that the assumptions are never perfectly met and often are considerably divergent from reality, the P3D model can have very poor accuracy for many cases. Therefore, several decades of research have targeted improving the accuracy of height growth simulations. For instance, the P3D model is incorporated with a two-regions model which applies 2D flow [Weng, 1992]. More recently, a 1D non-local elasticity scaling analysis [Adachi et al., 2010] was conducted to investigate a more generic parameter solution. Based on that analysis, an enhanced P3D model (EP3D) model has been developed, which considers the viscous resistance to height growth and lateral fracture toughness [Dontsov & Peirce, 2015]. This EP3D model has been shown to provide a drastic improvement in agreement with high fidelity models when compared to classical P3D.

In all manifestations, P3D ignores or at least coarsely approximates the impacts of vertical fluid flow and the non-local nature of the elasticity equation. In a move towards high fidelity simulation, the fully-coupled planar 3D models (PL3D) were developed and implemented, which considers generalized fluid flow and a full solution to the elasticity equation [e.g., Peirce & Detournay, 2008; Zia & Lecampion, 2020]. It is considered a fracture constrained to planar growth in a three-dimensional domain (hence the name “Planar 3D”). PL3D models discretize the fracture footprint into 2D meshes for computing fluid flow (Figure 2-4b) and then solve 3D elastic equations using classical approaches such as Boundary Element Method or Finite Element Method. This way, 2D flow combining with a non-local 3D elastic relationship is considered.

Compared to the P3D model, the PL3D model has fewer limitations and significant improvement in the accuracy of the result. Indeed, height growth has been shown to match very well with experimental validation for PL3D [Wu et al., 2008; Dontsov & Peirce, 2015]. Related to our research, the PL3D model can effectively simulate the facture propagation within a discontinuous matrix, at least in principle. However, solving a problem in a non-homogeneous domain generally requires the implementation of a finite element method (FEM) simulator. While acknowledging that it might be possible to do this on a commercial FEM platform, in the current research, a different approach based on the Distinct Element Method (DEM) is chosen and will be described in detail in Chapter 4.

2.3 Recent Height Growth Experiments

A recent study used laboratory experiments and DEM simulations to investigate hydraulic fracture height growth in systems of impermeable materials separated by interfaces of varying strength Xing et al. [2018a, b]. This work provides an initial indication of the stress contrast effect while considering the presence of a weak interface. The laboratory experiments consider a three-layer setup with transparent, impermeable materials (Figure 2-5a). This design can effectively simulate a multiple-layer formation while keeping the advantage of visualizing the hydraulic fracture propagation procedure. Besides, two dimensionless parameters are proposed as

$$H_b = \frac{\sigma_b - \sigma_r}{P_{net}} \qquad \text{Eq. 2-2}$$

$$H_v = \frac{\sigma_v - \sigma_r}{P_{net}} \qquad \text{Eq. 2-3}$$

Here, P_{net} is the net wellbore pressure equal to P_f-σ_r. We can notice that the H_b defined here is actually the inverse of the parameter on the left side of Eq. 2-1. It is found that under a relatively low vertical stress (H_v<2), the fracture transitions from containment to height growth with H_b=0.4~0.6 (Figure 2-6), which corresponds to $\frac{P_f-\sigma_r}{\sigma_b-\sigma_r}$ equals 1.6~2.5. Hence there is a significant shift favoring containment compared to the prediction based on Eq. 2-1. However, even previous work has successfully built up a series of criteria to classify tests into different fracture geometries. There are still several essential knowledge gaps that remain unfilled.

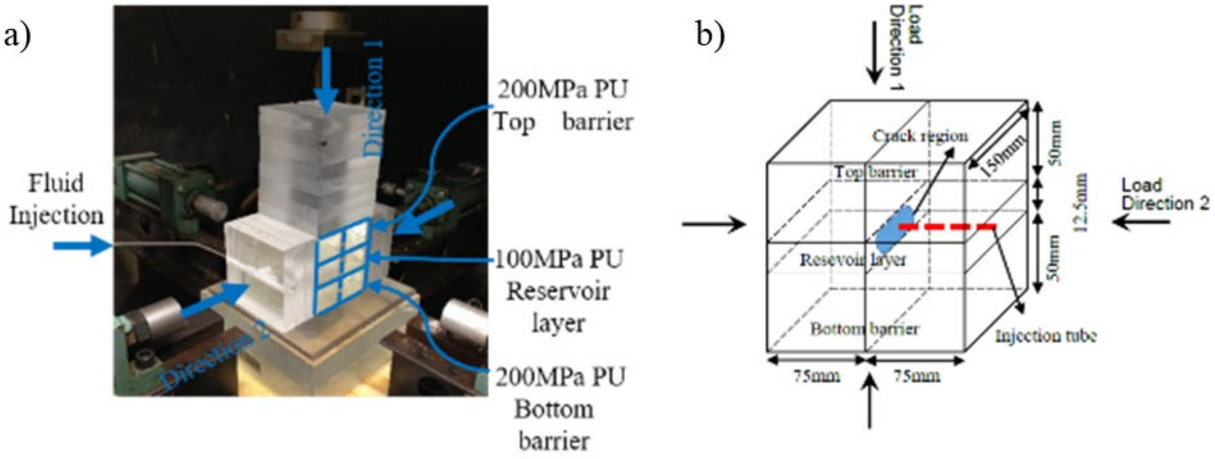

Figure 2-5 a) The experimental setup with transparent material from Xing's research. b) specimen sketch showing a hydraulic fracture containment geometry. [Xing et al., 2018a, b]

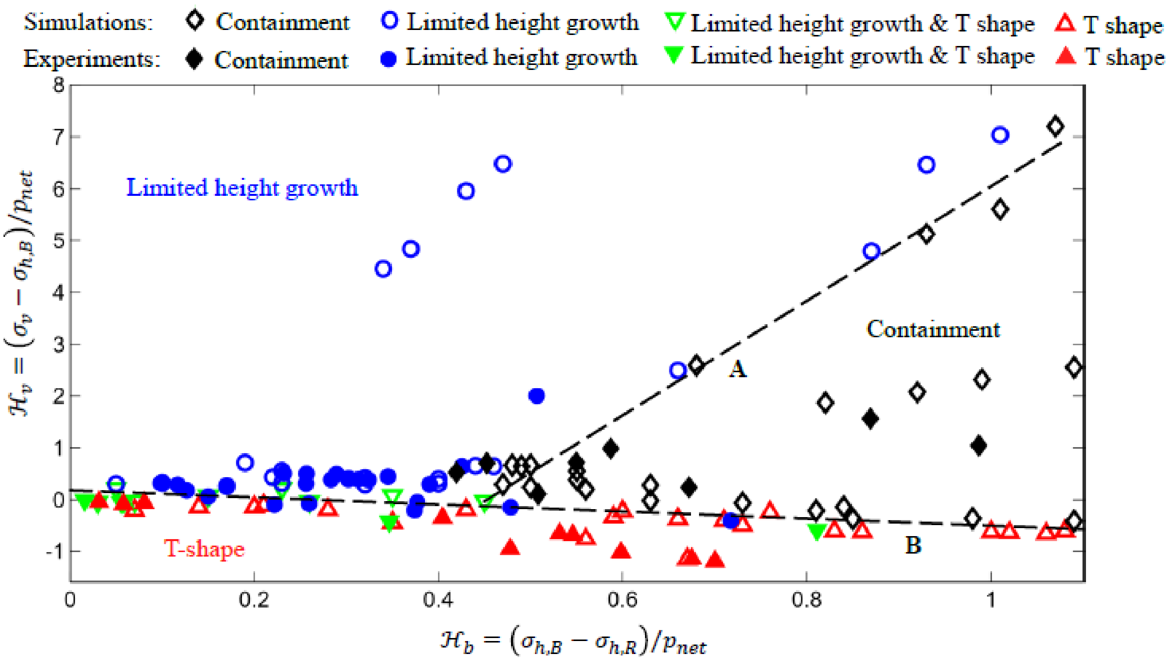

Figure 2-6. The parametric spaces plot for zero toughness interfaces shows the fracture geometry transition from containment to limited height growth at H_b around 0.4~0.6. [Xing et al., 2018a, b]

Firstly, upon careful examination of Figure 2-6, it becomes apparent that all experimental data points (solid marks) from this past research are located in a zone of relatively low vertical stress. In fact, all stresses in these experiments are limited to relatively low values due to the low Young's modulus of the material (it would deform problematically under larger stresses). The transition line in the high H_v zone is mainly predicted by the numerical simulation. Hence, without the experimental evidence support, it remains uncertain if there is a sloping boundary between regions of containment and height growth domains.

Secondly, only one non-uniform material combination was tested in this previous study, consisting of one manifestation of a soft reservoir and stiff barrier layers. It was a limitation of the experimental setup, wherein the stresses could not be applied independently in each layer like they are in the present work (as will be detailed in Chapter 3). Instead, the stress contrasts were generated by applying a uniform displacement to the boundary of the specimen, thus generating higher stress in the stiff barrier layers and lower stress in the reservoir. Because only one combination of stiffness was considered, the sensitivity of height growth to the elasticity contrast with weak bedding interfaces is still unclear.

2.4 Objectives

The overall goal of the research is to establish a series of experimental data sets along with a validated modeling method in order to guide the decision-making to limit extensive vertical fracture growth within the multiple-layer formation. To pursue this goal, the research will analyze the vertical fracture propagation from three perspectives: the pressure required to induce height growth, the evolution of height growth and its dependence on the pressure, and the impact of height growth on fracture width (aperture) both within the reservoir and the adjacent bounding layers.

The method of investigation entails analog laboratory experiments and numerical modeling, applying both in order to simulate how a hydraulic fracture behaves in a layered system. Both experiments and simulations investigate the sensitivity of height growth to varying stresses and layer properties in the presence of weak horizontal interfaces separating the layers. Laboratory experiments play the unique role of giving direct observation of a physical system under carefully controlled conditions. These results provide both conceptual basis and visible data for validating simulations. However, laboratory experiments are limited to laboratory scale, and they are too costly to run truly wide-ranging parametric studies.

On the other hand, numerical simulations can be carried out across a range of scales and can be used to efficiently investigate the sensitivity of hydraulic fracture growth to various parameters, but they require validation to experiments. Hence, bringing together both experiments and simulations is a preferred approach to relying on one or the other methods alone. With these methods, the scope of work includes:

- **Conduct lab-scale experiments with different stresses combinations in a three-layer system with all layers comprised of the same impermeable material.** Previous work was limited in the range of stresses that could be accessed, so this set of cases provides necessary validation data and a basis for comparing results from experiments with a more complicated system.
- **Expand three-layer experiments to include dissimilar impermeable and permeable materials.** The primary purpose of the impermeable experiments is to demonstrate the impact of contrasting mechanical properties on fracture geometry. Then, the role of fluid

loss in the porous host rock matrix is investigated by expanding consideration to permeable materials.

- **Apply numerical modeling to predict hydraulic fracture geometry in the presence of weak interfaces in a three-layer system of both similar and dissimilar materials.** The simulations provide micro-view information regarding the fracture growth (i.e., details of width in the reservoir and barrier layers) while macroscopically benchmarking with the laboratory experimental observation. Specifically, a commercially-available lattice-based hydraulic fracture simulator (XSite) is used, which can solve interactions between hydraulic fracture and pre-existing interfaces and handle variable layer properties and stresses while exacting a reasonable computational cost.

From an experimental perspective, the current study can extend the prior work to higher stress ranges (by using stiffer materials) and implement a method to independently apply stresses to all three layers, which thus can independently consider the sensitivity of height growth to stresses and mechanical properties of the layers. The present work also extends to permeable materials. In the meantime, to avoid making the topic too broad, it is important to also be clear about a few topics that, while interesting, are omitted from the current scope. These include:

- For both laboratory experiments and numerical simulations, the interfaces between different layers are left unbonded, thus considering only the limit of an interface with zero tensile strength and leaving the cases of intermediate tensile strength to future work.
- For the simulations, the fracture is assumed to propagate only in the plane that is perpendicular to the interfaces. The hydraulic fracture could generally propagate out of its original plane and, notably, into the weak interfaces themselves. However, in order to

maintain a manageable realm of simulation possibilities, the hydraulic fracture is allowed only to propagate in a pre-defined vertical plane.

- The numerical simulations do not extend to the cases of permeable materials. Instead, the permeable material cases are examined only via experiments. The simulator is, in principle, able to handle the case of fluid loss to the matrix but at an increased computational cost and expansion of scope that would be infeasible in the timeframe of the project.

The remainder of this thesis is organized to begin with a description of the experimental setup and characteristics of the results and observations (Chapter 3). Chapter 4 describes the setup and validation of the numerical simulator. Chapter 5 details numerical simulations of experiments, including validation through comparing the simulations with experimental data and an expanded parametric study at the experimental scale. After this, the overall conclusions of the work are summarized in Chapter 6.

3.0 Laboratory Experiments

Analogue experiments simulate a three-layer formation with a reservoir layer in the middle and barrier layers above and below. Various materials are combined to attain contrasts in material properties among the layers. Therefore, the experiments are conducted in groups based on different material combinations assigned to the analogue reservoir and barrier materials. Specifically, three types of non-permeable polymer materials and two types of permeable rock. The polymer and rock types are listed in Table 3-1, along with their Young's modulus and permeability. Here Young's moduli for impermeable materials are measured from uniaxial compression tests. The approximate values for the permeable materials can be obtained by referencing [Holder et al., 2001, Pagoulatos, 2004]. Besides, permeability can be obtained from the vendor's published data. Note that for all cases, the elastic modulus ratio e is defined as

$$e = \frac{E_r}{E_b}$$

where E_r and E_b correspond to the Young's modulus of reservoir and barrier layers, respectively.

As mentioned in the Introduction, the lab experiments focus more on the impermeable material groups, whose primary goal is to investigate the role of stress and Young's modulus contrasts on the fracture height growth. In contrast, the permeable material group is carried out as an exploratory exercise, focusing on qualitative fracture behavior once the reservoir and barrier layers are permeable.

Table 3-1 The Young's modulus and permeability of layer materials

Materials	Young's Modulus	Permeability
	GPa	md
Polypropene (PP)	2	Impermeable
Polycarbonate (PC)	2.7	Impermeable
Polymethyl Methacrylate (PMMA)	3.2	Impermeable
Scioto Sandstone	11.4	0.001-0.01
Berea Sandstone	20~25	100-250

3.1 Experimental Preparation

3.1.1 Specimen and Injection Fluid Preparation

Two pieces of material 'A' (specified as one of the materials from Table 3-1) are precisely machined 9.53×11.43×22.86 cm^3 dimensions in order to perform as barrier layers. Another sheet of material 'B' is machined to dimensions of 1.91×15.24×22.86 cm^3 and behaves as the analogue reservoir layer (Figure 3-1). In addition to the reservoir and barrier assembly, a 22.86×24.13×10.16 cm^3 PMMA block is used as a loading platen but with the added purpose of generating a transparent layer through which a camera can view from an oblique angle to the plane on which hydraulic fractures will grow. Next, all materials are further ground and polished to reduce friction and avoid open intervals from the bedding interfaces. Finally, a reference grid of 1.27cm is made on the observation block before each test to assist with extracting quantitative measurements of length and height from video images.

A glycerin-based fluid is used for generating hydraulic fractures. Because it has a higher viscosity than water, it is less prone to channeling through small imperfections in the machined surfaces. It is also much less prone to problematic levels of leakoff when experiments involve permeable layers, where we note that the available quarried sandstones (Table 3-1) have higher permeability than rocks that are most typically encountered in sedimentary sequences associated with hydrocarbon resources. Hence the elevated viscosity of the fluid provides some degree of physical similarity to a field scenario with lower permeability layers. In the formulation used for these experiments, blue food dye is mixed with glycerin with a 1:10 volume ratio, which gives us a mixture fluid with an approximately 0.3 Pa·s viscosity. Additionally, the rock specimens are fully saturated with water before each permeable material group test to reduce the fluid dissipation into the rock matrix, which will be explained in detail in the later section.

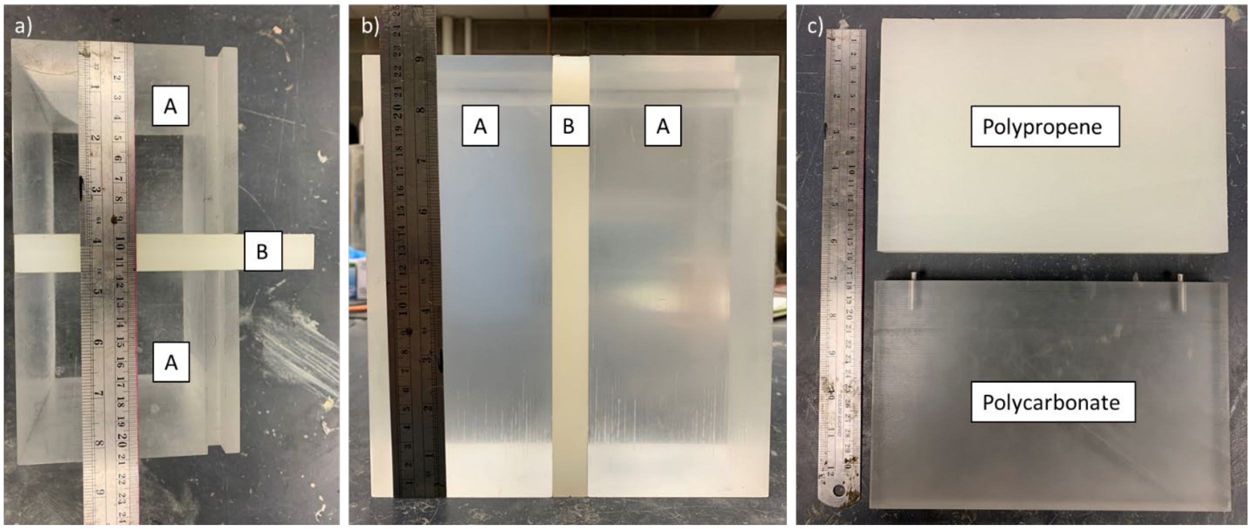

Figure 3-1. Specimen materials after being machined into desired sizes.

3.1.2 Experiment Setup and Loading Distribution

All three layers are assembled, as shown in Figures 3-2. They are firstly aligned on the left side, and then they are pushed against the PMMA observation block. Vertical interfaces (the interface between PMMA observation block and experimental specimens) and two analogue weak bedding plane interfaces (interfaces between reservoir layer and upper / lower barrier layers) are thus generated, as highlighted by the blue outline in Figure 3-2a. As mentioned earlier, all interfaces are left unbonded to implement zero-toughness interfaces, which can be expanded in future work to finite strength interfaces, for example, via controlled bonding described by Xing et al. (2018a).

A 0.3175 cm stainless steel tube is placed through the observation block, which acts as an analogue wellbore. The tubing outlet should face the geometrical center of the reservoir layer. Once assembled, stresses are generated using two axes of a true-triaxial loading frame, as shown in Figure 3-2c with accompanying detail in Figure 3-2b, which shows the cross-section of the experimental setup including applied stresses. It shows the result of ydraulic pistons applying the loads from the X and Y directions, equivalent to minor horizontal and vertical stresses, respectively. The Z-direction is taken as the orientation of major horizontal stress. Due to the restrictions on fracture growth direction provided by the specimen geometry, the stress in this direction can be taken as zero without impacting the fracture growth. In other words, because the fracture cannot reorient to that direction, geometric equivalence to a case with infinitely large maximum horizontal stress is achieved without the need for loading to actually be applied in the Z-direction. Note that special loading platens and loading processes are designed to generate stress contrast between barrier layers and reservoir, which will be illustrated in detail next section.

Typically, the barrier stress σ_b is set to be larger than the reservoir stress σ_r. The stress σ_v is the analogue vertical stress, which is directly applied to the top and bottom surfaces of the barrier layers and assumed to be uniformly distributed through the entire specimen.

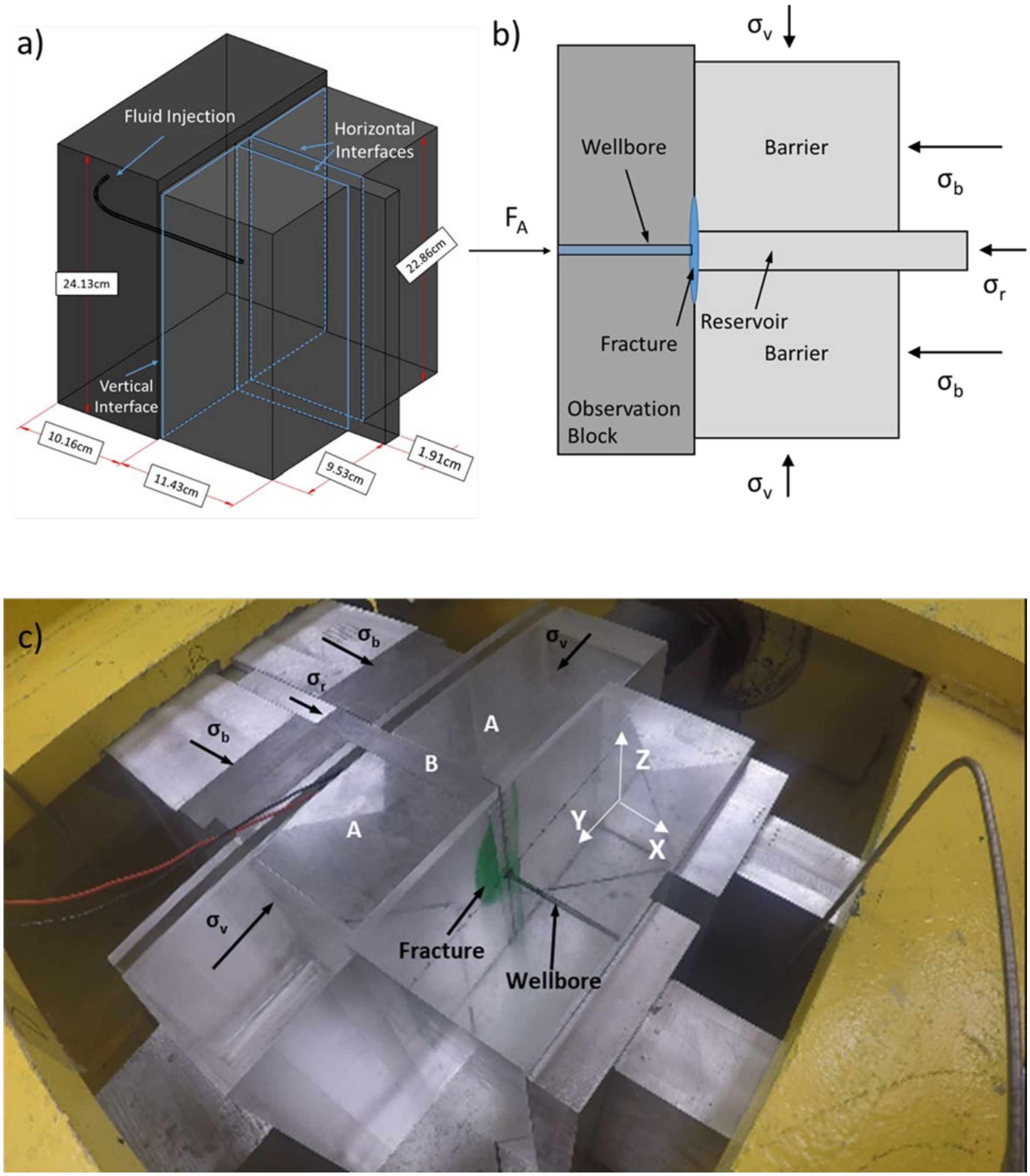

Figure 3-2. a) The sketch of the specimens set up, including the location of interfaces, which are indicated in the blue outline. b) Cross-section of the experimental setup and loading distribution. Note that "horizontal" and "vertical" refer to orientations in the analogue field setting with horizontally directed minimum stress, vertical hydraulic fracture orientation, and weak horizontal interfaces. c) An example experimental setup of PMMA-PMMA test.

3.2 Experimental Procedures

3.2.1 Loading Procedures

Firstly, all the hydraulic pistons and syringe pumps are wired to the data acquisition system, thus enabling monitoring and recording of applied loads and fluid injection pressure. As illustrated in Figure 3-3a, the loading procedure starts with the activating piston B controlled by a syringe pump, which is set behind the reservoir layer and presses the reservoir layer forward onto the observation block with loading σ_r. Then piston A is activated and pushed all three layers slowly backward to the right until the edge of the loading frame holds the spacers behind the barrier layers. Next, the desired load that piston A applies is taken as a force F_A, which satisfies:

$$F_A = \sigma_r A_r + 2\sigma_b A_b \qquad \text{Eq.3-1}$$

Here, A_r and A_b are the contact area of the reservoir layer and barrier layers. The syringe pump should be on and maintain constant pressure during the whole procedure (Figure 3-3b). Once the horizontal stresses are loaded, piston C and piston D are activated to apply σ_v to the specimens (Figure 3-3c). Finally, the horizontal stresses may be affected by the vertical stress due to the tri-axial loading. A micro-adjustment needs to be done before shutting down valves and locking the pressure. Due to the ductility of the injection system (pressure hoses, pistons), the actual confining pressure may drop below the scheduled one during the experiment. The post-data analysis will be based on the actual values recorded by the data acquisition system.

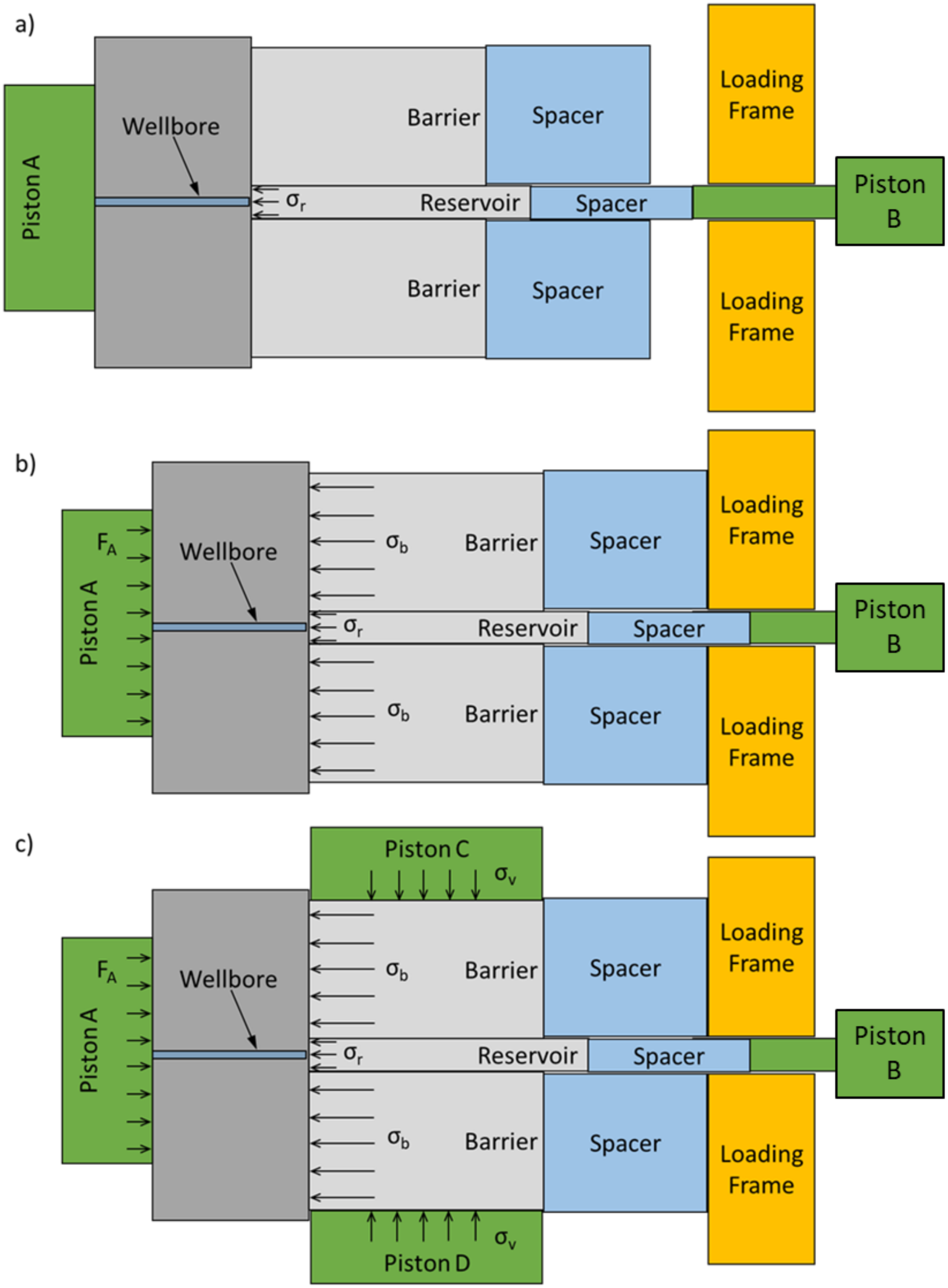

Figure 3-3. The sketch of experiment loading procedures includes a) running piston B which is controlled by syringe pump to apply σ_r, b) running piston A to apply σ_b, and c) running piston C and D to apply σ_v.

3.2.2 Injection Procedures

After finishing confining stresses loading, the injection procedures will be conducted. The same data acquisition system will monitor the pressure and flow rate of the injection syringe pump, which is connected to the wellbore pipe. Meanwhile, a video camera is mounted behind the observation block (similar angle as in the viewpoint of Figure 3-2c) to record hydraulic fracture growth evolution once the test starts. Then, the glycerin mixture is pumped into the wellbore with either constant pressure or upward step-wise pressure injection schedule.

Before continuing to illustrate typical behavior, it is worth a brief discussion of this choice of a pressure-type inlet boundary condition. In field hydraulic fracturing, the inlet boundary condition is typically obtained by setting an injection rate, not pressure. However, the choice of pressure boundary condition in the lab experiments is justified because:

1) One of the motivations of the present work is also related to water flooding at pressures above fracturing pressure, and in these cases, the injection rate is adjusted to achieve a certain maximum injection pressure that is constrained by factors that include preventing unwanted height growth.
2) From a practical perspective, in hydraulic fracturing operations, it is common for the rate to be adjusted in light of pressure limits. Also, because of the impact of flow through perforations and near-wellbore fracture tortuosity, it is often the case that injection pressure is effectively constant over practically-relevant portions of the treatment.
3) From the standpoint of implementing operational changes based on the outcomes of these experiments, it is anticipated that delineation of maximum injection pressure to avoid unwanted height growth would be readily adopted. With this goal, setting varying pressures

allows the most direct way of exploring the relationship between injection pressure and height growth.

3.2.3 Overall Observations

Generally speaking, hydraulic fracture propagation can be divided into three stages once the injection starts. Firstly, the hydraulic fracture initiates in the reservoir layer (Figure 3-4a). Over a range of low pressures, the injection fluid mainly flows along the length direction and barely into the barrier layers (Figure 3-4b), which gives rise to a contained hydraulic fracture. However, as the wellbore pressure increases, it eventually reaches a critical value P_{fc} (Figure 3-4c). After reaching this pressure, an unstable fracture height growth occurs (Figure 3-4d). The test is finished once the rapid fracture height growth takes place. Then, all related data (confining stresses, wellbore pressure, flow rate) are exported from the data acquisition system. By referring to the video record, the critical moments and corresponding values of the pressure and fracture geometry can be found, with the most critical being the wellbore pressure leading to rapid fracture height growth under different boundary conditions.

Figure 3-5 illustrates a typical injection record for experiments with impermeable materials. This record consists of the wellbore pressure P_f (MPa) and injection flow rate Q_0 (ml/min) versus the time (s). It is observed that from the beginning of injection until the wellbore pressure reaches 4.82MPa, the injection flow rates are extremely small, even below the syringe pump sensor tolerance (the negative values are due to the calibration error, but essentially because the readings are too small).

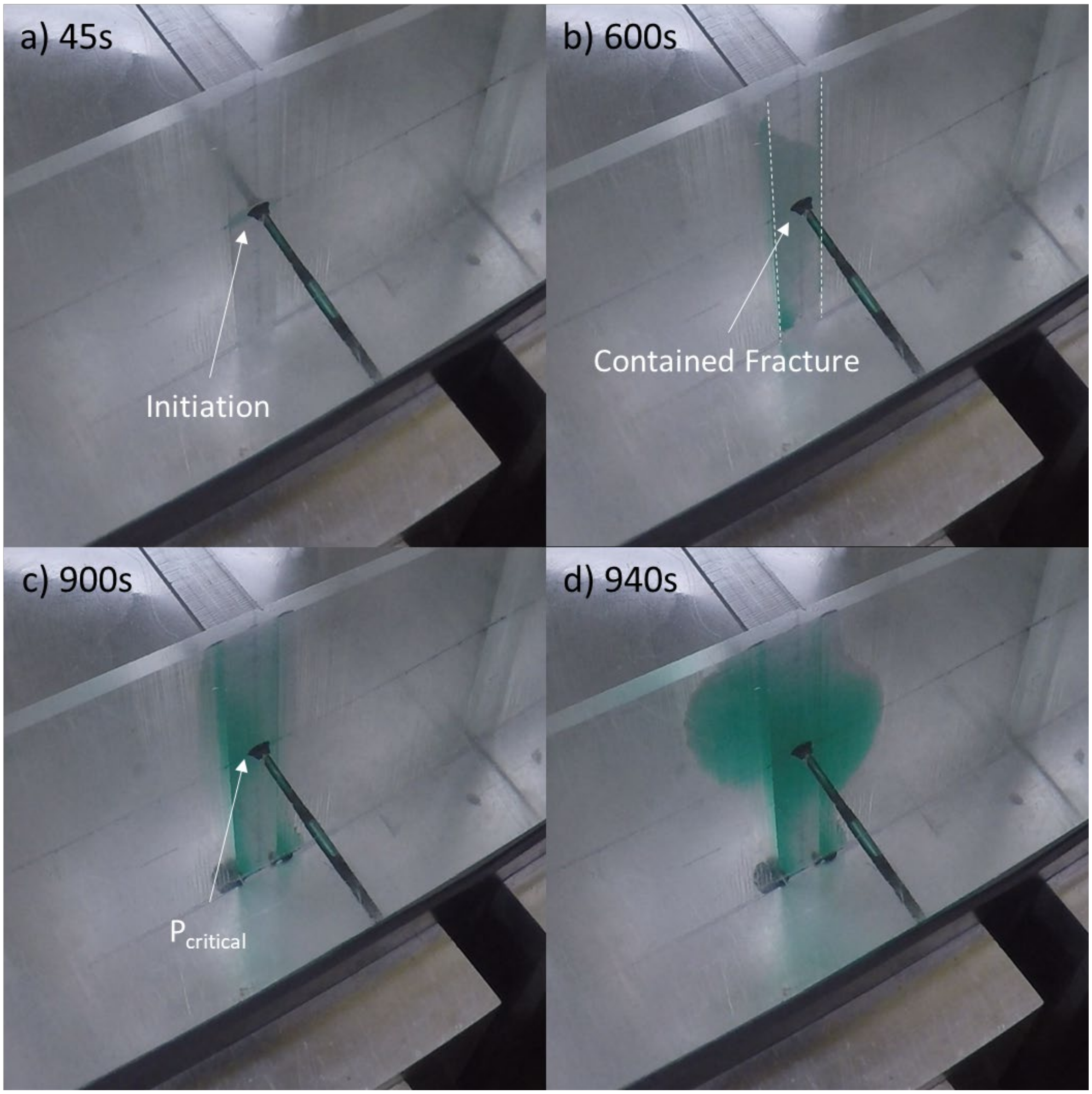

Figure 3-4. The process of fracture propagation. a) Fluid injection starts. b) Fracture initiation. c) Fracture is contained by the weak interfaces indicated by dashed lines and high stress barrier layers. Hence, it only propagates within the reservoir layer. d) Wellbore pressure reaches a critical value, and the unstable fracture height growing starts.

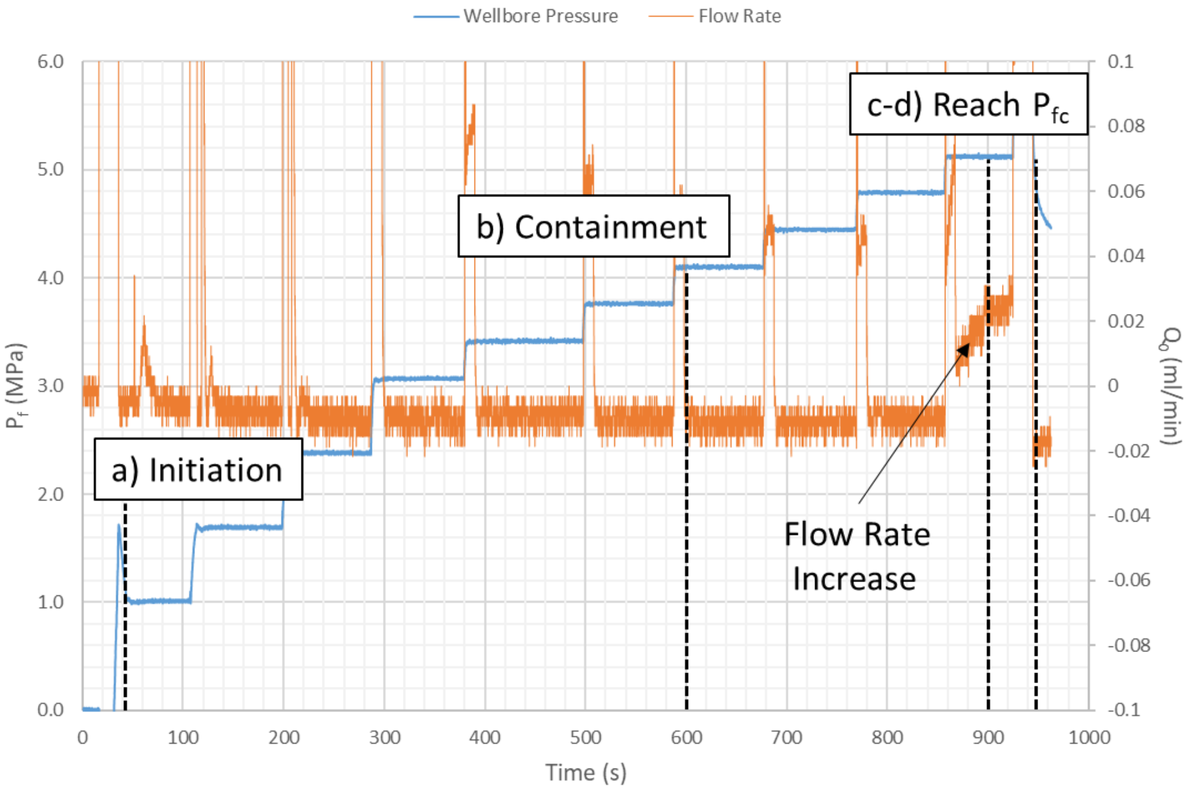

Figure 3-5. The injection plot of the impermeable material group test includes the wellbore pressure P_f (MPa) and injection flow rate Q_0 (ml/min) versus the time (s). It shows an unstable fracture height growth occurs at approximately P_{fc}=5.17MPa, combined with an increase of injection flow rate.

Additionally, it is observed that the fracture unstable height growth takes place at $P_{fc} \approx$ 5.17MPa. At the same point in the experiment, the injection flow rate has a distinct increase to approximately 0.02 ml/min. This observation provides a connection between observed height growth in the images and records that are available in the field, namely injection rates and pressure.

3.2.4 Experimental Groups

The basic principle for the impermeable experimental arrangement is to maintain the same barrier material (PMMA) while varying the reservoir layer material's Young's modulus. Thus, three impermeable material experiment groups are conducted, as shown in Table 3-2. These correspond to reservoir layer material candidates are PMMA, PC, and PP, which lead to the elasticity modulus ratio e equals 1, 0.84, and 0.61, respectively.

Table 3-2. Experimental groups for impermeable material combinations.

Group Name	**Reservoir Material**	**Barrier Material**	$e = \frac{E_r}{E_b}$
PMMA-PMMA	PMMA	PMMA	1
PC-PMMA	PC	PMMA	0.84
PP-PMMA	PP	PMMA	0.61

The primary purpose of the permeable material experimental program is to investigate the influence of permeability on hydraulic fracture height growth. Therefore, the experimentation considers three groups with various combinations of reservoir and barrier materials (Table 3-3).

Table 3-3. Experimental groups for permeable material combinations.

Group Name	Reservoir Material	Barrier Material
PC-Scioto	PC	Scioto Rock
Scioto -PMMA	Scioto Rock	PMMA
Berea-Scioto	Berea	Scioto

3.3 Onset of Height Growth for Impermeable Material Groups

While a more detailed comparison to a numerical model will be left to later in the thesis, it is useful to investigate how the pressure associated with the onset of height growth behaves across the various experimental groups. To provide some context to these results, one can propose that height growth in a uniform, elastic material with zero fracture toughness would follow the solution of Simonson et al. [1978], as presented previously in Eq. 2-1. By this model, uncontrolled height growth is predicted, e.g. [Nolte & Economides, 2000]

$$\frac{P_f - \sigma_r}{\sigma_b - \sigma_r} > 0.3\sim0.4 \qquad \text{Eq. 3-2}$$

Here the numerator gives the difference between fluid pressure and reservoir stress. The denominator gives the stress jump between the reservoir and the barrier layer. On the other hand, one could propose that height growth would become uncontrolled once the fluid pressure equals the stress in the barrier layer. Clearly, results will differ from these simple cases, notably because of the presence of the weak interface and Young's modulus contrast.

3.3.1 PMMA-PMMA Group

The uniform, impermeable material group (PMMA-PMMA) test provides a starting point that is the basis for comparison for other experiments. Inspired by the form of Eq. 3-2, the numerator and denominator term are plotted for the moment where height growth is observed to become unstable in Figure 3-6. For all the tests, the reservoir stress σ_r is 2.76 MPa. We can see two clusters of data points. The first cluster points have barrier stress σ_b in the range of 3.86~4.07MPa, with corresponding pressure at the onset of unstable height growth P_{fc} in the range of 4.68~5.31MPa. The second cluster has two points with barrier stress σ_b around 5.38MPa, corresponding to pressure causing unstable height growth P_{fc} of around 6.21MPa. For reference, the label beside each point is the corresponding vertical stress σ_v, in MPa, noting that the complete data can be found in Appendix Table B-1. For reference, the dashed line shows the prediction of unstable fracture height growth based on Eq. 3-2, and the solid line represents $P_f = \sigma_b$. Thus, it is clear that Eq. 3-2 vastly underpredicts the wellbore pressure required to induce rapid fracture height growth. Moreover, the wellbore pressure can even go above the barrier stress σ_b.

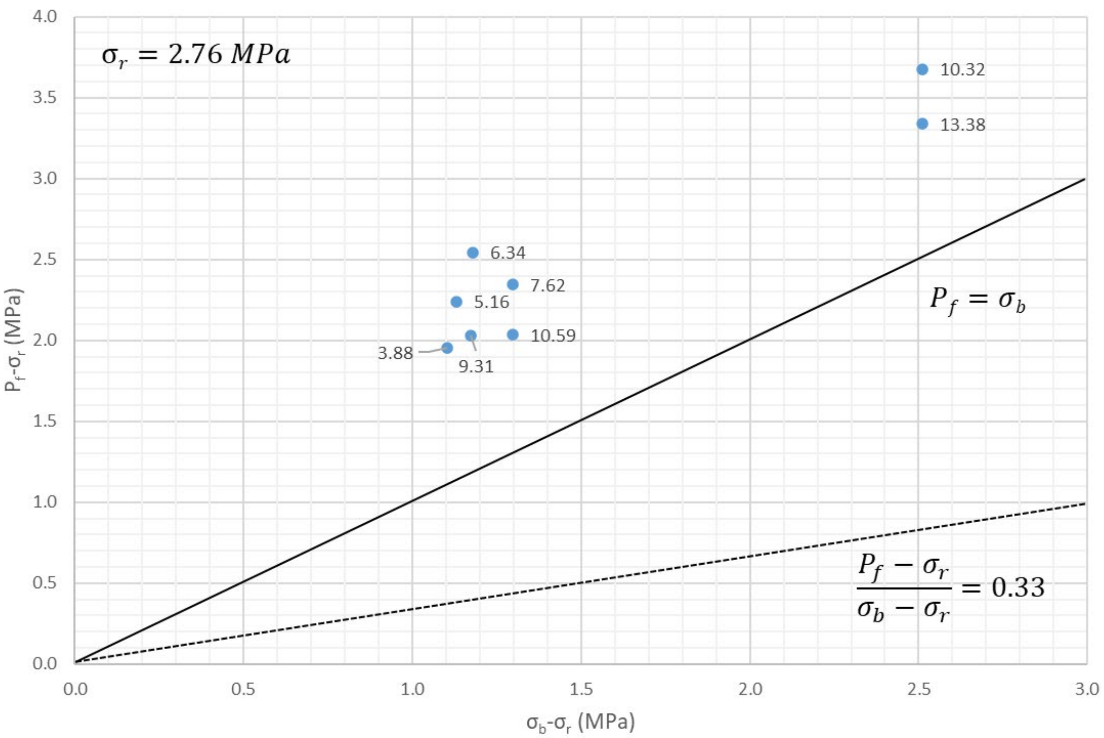

Figure 3-6. The PMMA-PMMA experimental group result shows the relationship between critical pressure P_{fc} and barrier stress σ_b, normalized by reservoir stress σ_r. The dashed line shows the criteria of unstable height growth derived by Simonson. In contrast, the solid line provides a reference that shows $P_f = \sigma_b$.

In greater detail, it is observed that within each data cluster in Figure 3-6, there is at least some potential for correlation between decreasing vertical stress and increasing the pressure sustained before unstable height growth. To further investigate the role of the vertical stress, the same data are plotted in Figure 3-7 with σ_v versus P_{fc}. The data label beside each point is the corresponding σ_b values, again in MPa. The black arrows connect tests with the closest barrier stress, from the one with large vertical stress to the one with small vertical stress. From this, we can see that for all other factors being similar, an increase in vertical stress σ_v causes a reduction in critical pressure for height growth. However, we should also realize that even the high vertical stress may promote fracture height growth by reducing the critical wellbore pressure, the barrier stress is still dominated factor in compare with vertical stress, noting that the sensitivities of critical pressure to barrier stress and vertical stress are $\Delta P_{fc}/\Delta\sigma_b \approx 1$ and $\Delta P_{fc}/\Delta\sigma_v \approx 0.1$, respectively.

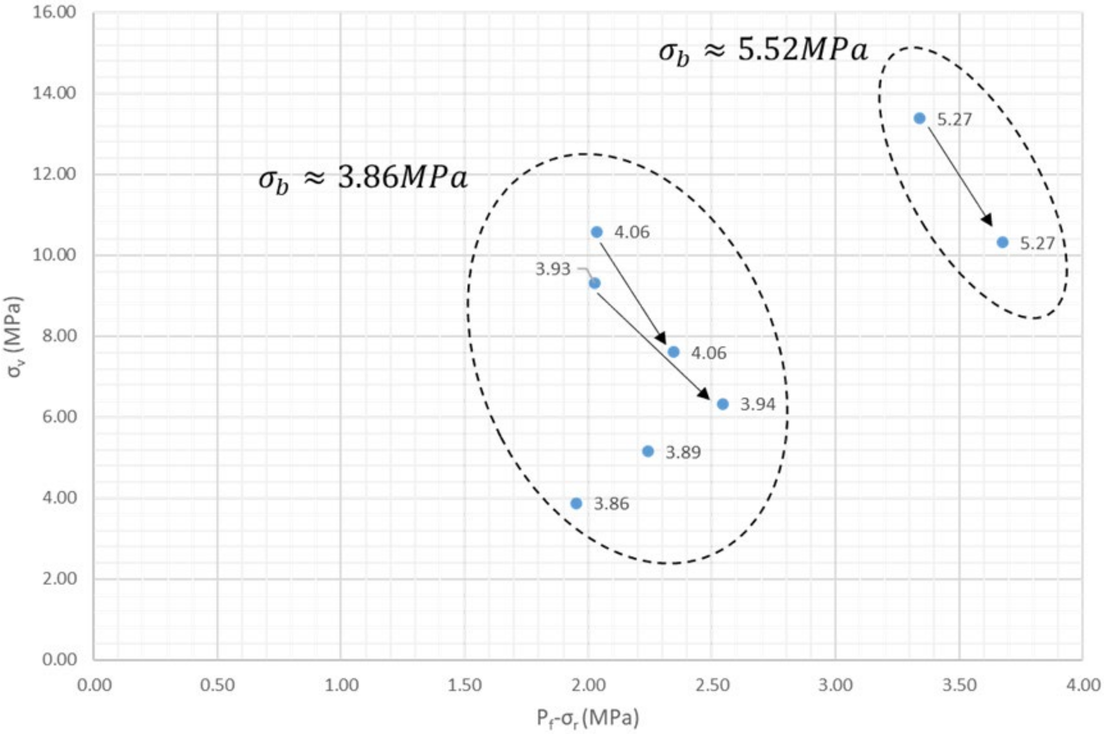

Figure 3-7. The PMMA-PMMA experimental group result shows the relationship between σ_v versus P_{fc}.

3.3.2 Elasticity Contrast Effect

The base case of PMMA-PMMA is extended upon to examine both small elastic moduli contrast (PC-PMMA, E_r/E_b=0.84) and moderate elastic moduli contrast (PP-PMMA, E_r/E_b=0.61). Figure 3-8 illustrates the relationship between the pressure required to cause unstable height growth and the barrier stress for all three groups (PMMA-PMMA, PC-PMMA, and PP-PMMA), with the number next to each data point indicating the vertical stress in MPa. Once again, all data points are distributed above the $P_f = \sigma_b$ line, and in fact, the PMMA-PMMA group and PC-PMMA group data points are very close to each other. In other words, for the small contrast in elastic modulus, there is no clear effect at the resolution of the experiments. However, there is a significant shift toward higher pressure required for unstable height growth when the Young's modulus contrast is higher, that is, when comparing the PP-PMMA group with the PMMA-PMMA group. For similar barrier stress, the PP-PMMA group has a critical wellbore pressure of approximately 2.1~2.8 MPa larger than the PMMA-PMMA group. This result provides evidence that a relatively stiff barrier compared to a softer reservoir layer can further limit fracture height growth by increasing the required critical wellbore pressure. Note that the raw data for the PC-PMMA and PP-PMMA can be found in Appendix Table B-2 and B-3, respectively.

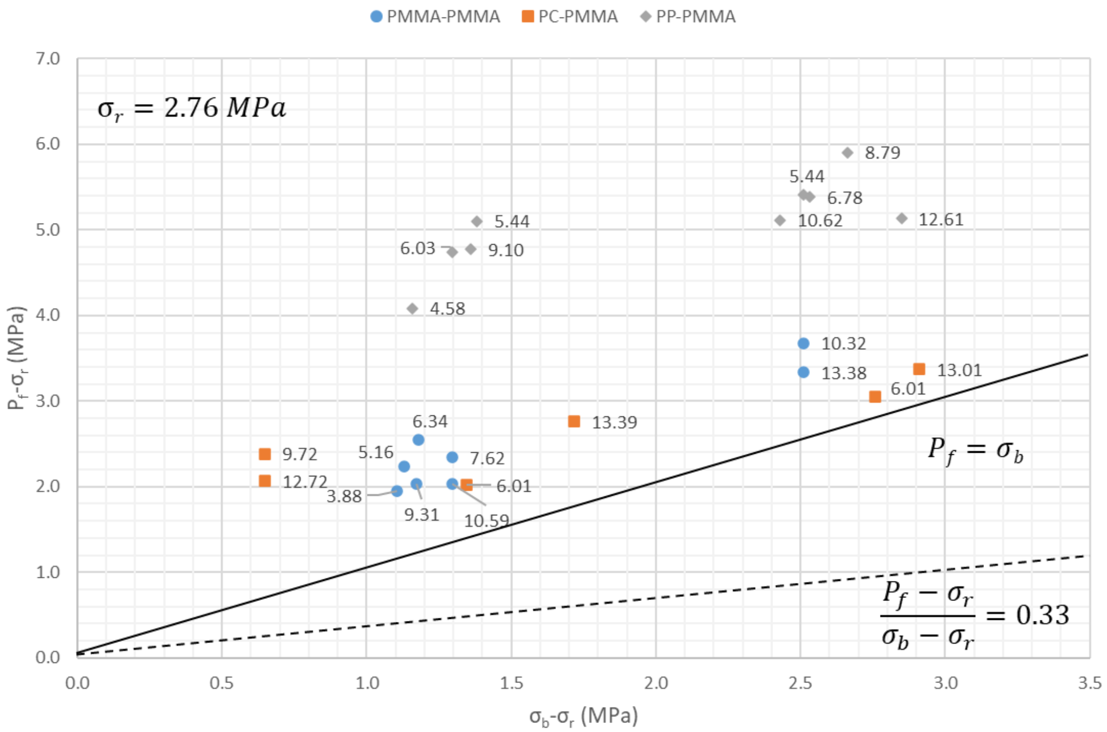

Figure 3-8. Experimental data show the relationship between critical pressure P_{fc} and barrier stress σ_b, indicating that a soft reservoir layer can limit vertical fracture growth by increasing the required critical wellbore pressure. The vertical stress value in MPa is denoted by the number next to each data point.

Finally, Figure 3-9 illustrates the combination of the new experimental results with previous experimental data from [Xing et al., 2018a]. It should be noted that the stress range applied in experiments of [Xing et al. 2018a] is (10-1~100 MPa), which is different from the range used here (100~101 MPa). Thus, the axis variables are normalized with the reservoir stress σr. For the [Xing et al., 2018a] data, the solid triangle marks indicate the test cases that have fracture height growth taking place, while the unfilled triangle marks represent the cases that have no fracture height growth happened (containment). Therefore, it is reasonable to take the overlapped part as the critical transition zone, as indicated by the dashed green line (noting that none of the lines is the best fit, they are included for illustration only). Plotting in this way shows that the data of Xing et al. [2018a] is basically consistent with the new observations. Specifically, it is observed that the previously-tested Er/Eb=0.5 experimental group would be expected to require even higher wellbore pressure to induce fracture height growth than our PP-PMMA group with an E_r/E_b=0.61 even if experiments were run with the same combinations of stresses.

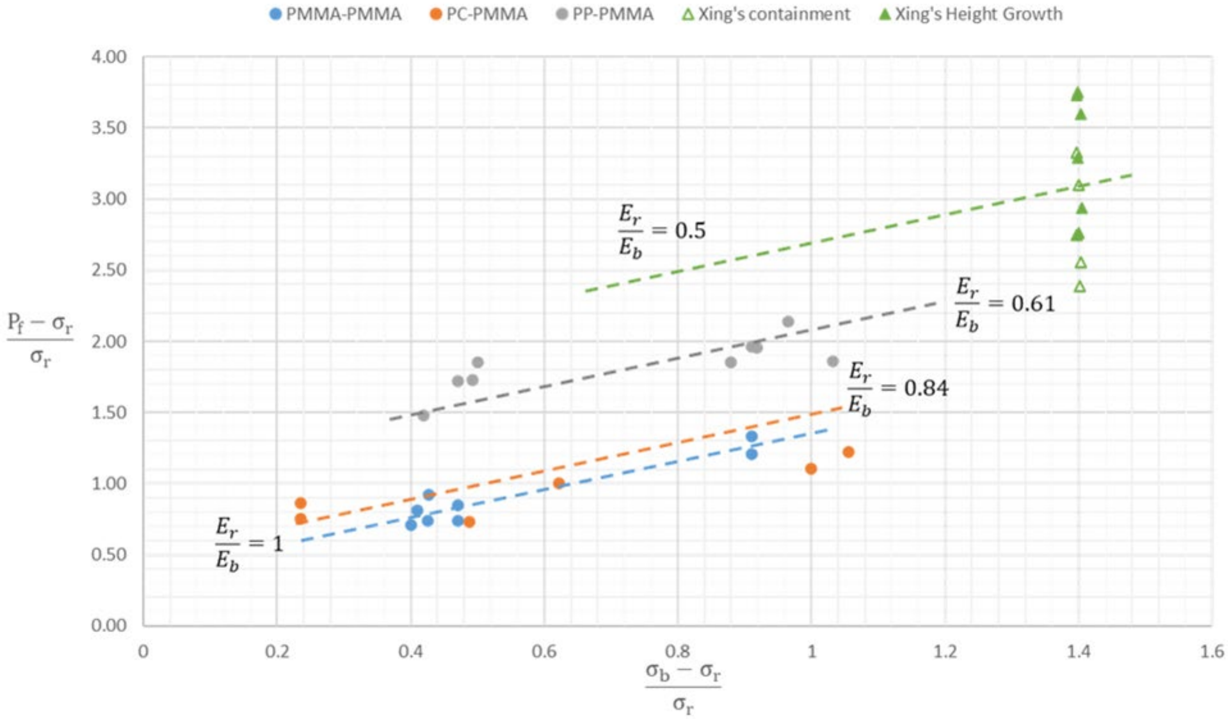

Figure 3-9. Combination of new data with prior data from [Xing et al. 2018a], showing that the critical wellbore pressure to induce fracture height-growth increases once the Young's modulus contrast is enlarged.

3.4 Permeable Material Group

3.4.1 Scioto-PMMA Group

The Scioto-PMMA group involves using a relatively stiff but permeable material for the reservoir that is bounded by a relatively soft and impermeable barrier layer (recall Table 7-4). Three tests are conducted with fixed vertical stress equal 10.49MPa, while varying reservoir stress 2.07~ 2.76MPa and barrier stress 3.80~5.81MPa. The Complete data is given in Appendix Table B-4.

A sample of images of experiment # 2019-06-13-1 illustrating the progression of hydraulic fracture growth is shown in Figures 3-10. Meanwhile, the wellbore pressure (blue line) and flow rate (orange line) are given in Figure 3-11. The corresponding boundary stresses can be found in Appendix Table B-4. There are several observations. Firstly, due to the high fluid diffusion in the reservoir layer, a much higher injection flow rate is required to maintain the same wellbore pressure than the impermeable material group. The fluid transport can be seen both to the matrix as well as distributed on top of the reservoir layer, see Figure 3-10c. We can observe that the flow rates are 10^0~10^1 ml/min, which is approximately 1000 times the rate of the impermeable material group when subjected to the same pressure range (which were less than 10^{-2} ml/min, recalling Figure 3-5).

Secondly, behavior that appears like fracture initiation takes place at low pressure, approximately 1.4MPa. However, the fracture initiation speed is much faster than the impermeable groups. In the meantime, the visualized color of fracture is darker. Considering the high injection rate does not apparently increase the fracture area. Thus, it is unlikely that the fluid invasion observed here is associated with the opening of the vertical interface as with the impermeable groups. Instead, it is likely a diffusive process, possibly coupled with the pressure via a pressure-dependent interface permeability. In other words, a permeable reservoir allows injection fluid to diffuse into the matrix with a pressure that is not sufficient to fully open a new fracture, but is perhaps sufficient to change the hydraulic width of a channel that is closed on the asperities of the two opposing faces. As a result, it is challenging to distinguish opening from flow into a closed fracture for the permeable reservoir layer cases.

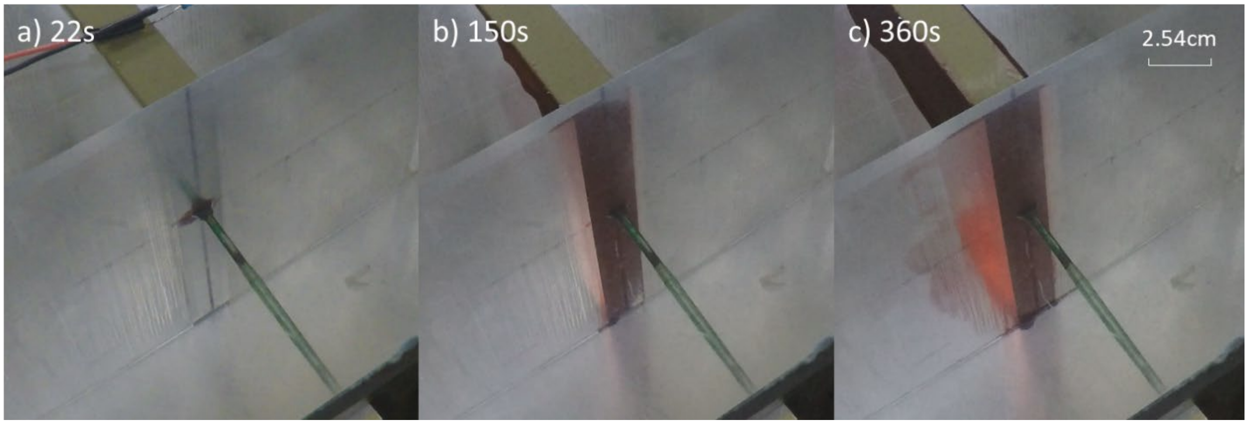

Figure 3-10. The progression of the Scioto-PMMA experiment(# 2019-06-13-1) at the moment when a) fracture initiates at 22s, b) fracture is mainly contained in the reservoir layer at 150s. c) unstable fracture height growth takes place with high leakoff on the top at 360s (oriented to the left in this photograph).

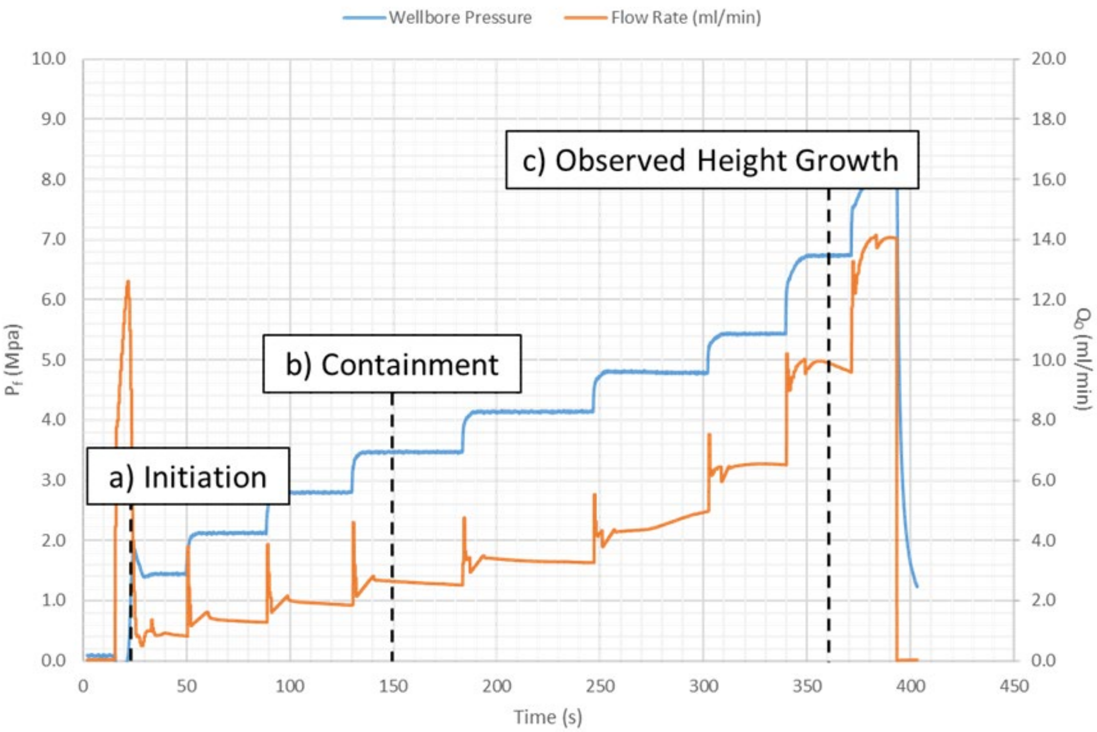

Figure 3-11. The injection plot of the Scioto-PMMA experiment(# 2019-06-13-1) includes the wellbore pressure P_f (MPa) and injection flow rate Q_0 (ml/min) versus the time (s). The video record shows an unstable fracture height growth occurs at approximately P_f=6.90 MPa.

Besides making initiation less clear and increasing the fluid injection rate necessary to maintain each pressure level, the permeable layer can make detecting unstable height growth difficult and somewhat ambiguous. For test # 2019-06-13-1 (i.e., Figure 3-11), the onset of unstable height growth occurs at $P_{fc} \approx 6.90$MPa. However, by making an injectivity plot (i.e., injection rate versus pressure), Figure 3-12 indicates that the Q_o versus P_f slope changes at $P_f \approx$ 4.83MPa. If one did not have access to images, it would be tempting to designate this inflection at 4.83MPa to be indicative of the onset of unstable height growth. This ambiguity is problematic if one considers that someone does not have direct fracture observation for field diagnostics but instead must rely on analysis of more common data like injection pressure and rate relationships.

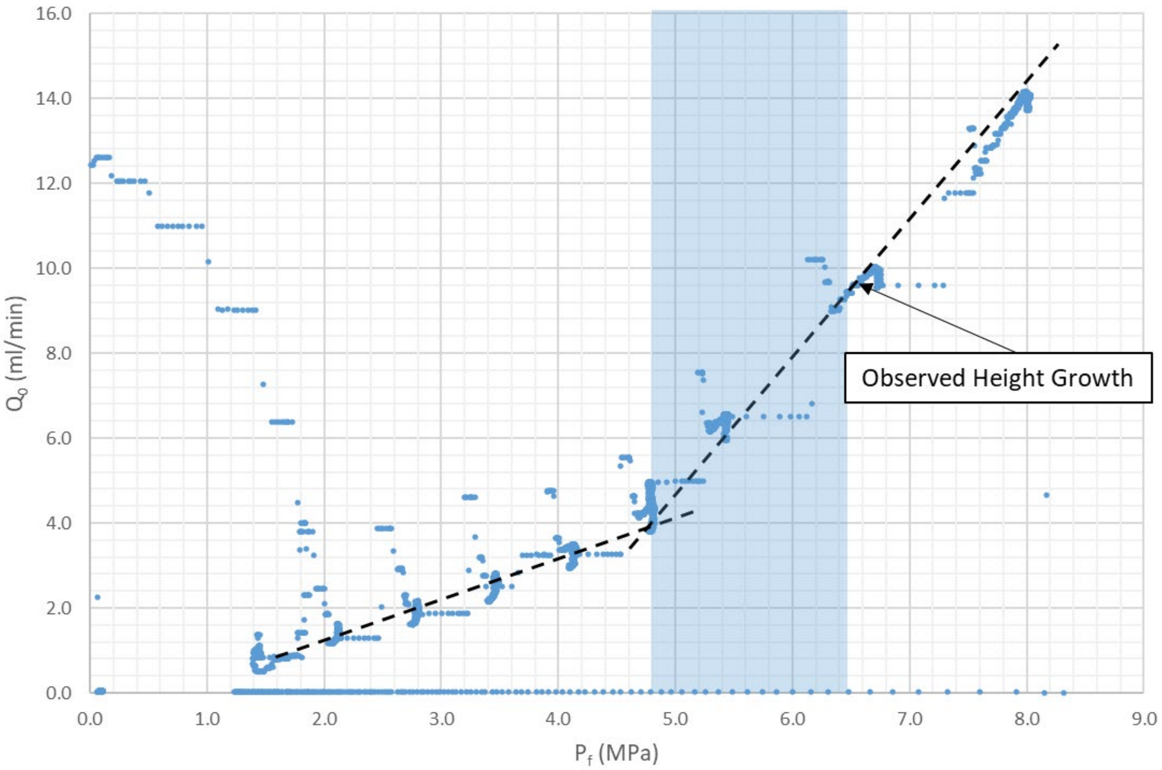

Figure 3-12. The plot shows the relationship between injection flow rate and wellbore pressure. It shows that the slope changes at wellbore pressure equal to 4.83 MPa, lower than the video observed critical pressure.

Next, it is useful to observe the impact of permeability contrast on height growth by comparing the Scioto-PMMA test group with the impermeable material groups. Figure 3-13 shows that the pressures required for inducing unstable height growth for the Scioto-PMMA cases are distributed between the PP-PMMA and PMMA-PMMA groups. The average difference between critical wellbore pressure and barrier stress is approximately 1.7 MPa. Considering the critical wellbore pressure may be over-estimated due to ambiguity in picking the point of instability, as discussed above, the actual Scioto-PMMA group data could even shift down and be closer to the PMMA-PMMA group. However, the critical pressure will still plot above the $P_f = \sigma_b$ line even with this uncertainty band.

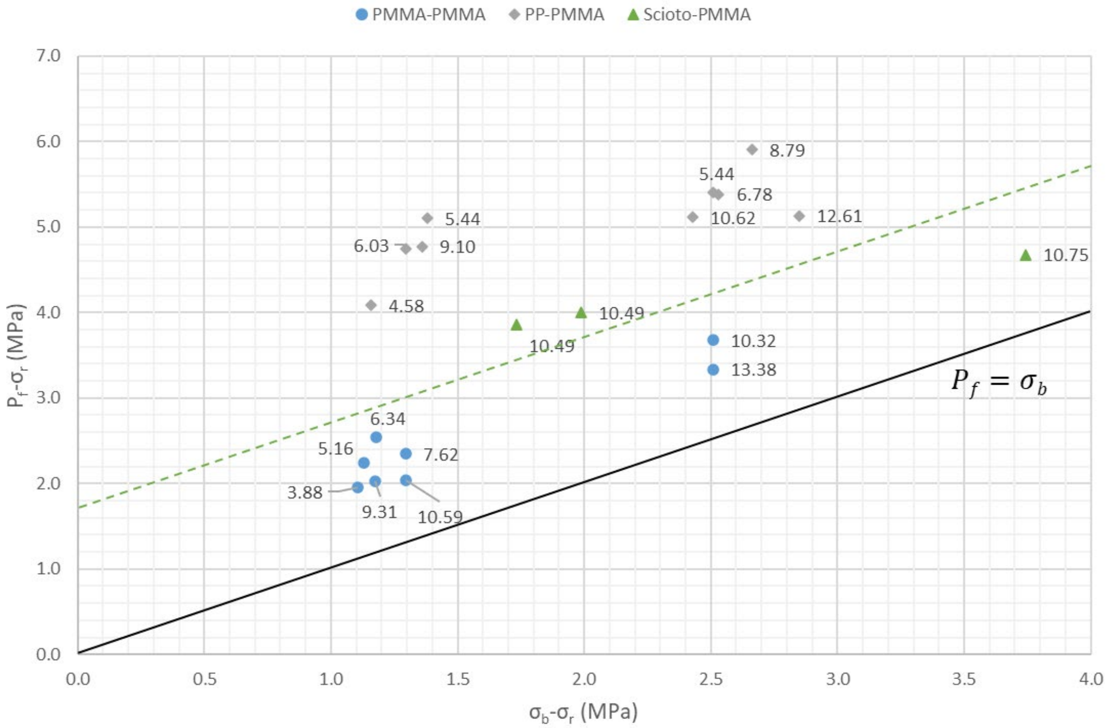

Figure 3-13. The critical pressure for the Scioto-PMMA experimental group along with impermeable group cases for reference, showing that the critical wellbore pressures are distributed between the PMMA-PMMA and the PP-PMMA groups' values. The vertical stress value, in MPa, is denoted by the number next to each data point

To summarize, the results show that a permeable reservoir layer may have a minor impact on the critical wellbore pressure. However, it is also observed that the permeable layer may have a secondary but important impact of reducing height growth by consuming fluid in the reservoir via leakoff so that it is not available to generate height growth.

3.4.2 PC-Scioto Group

The PC-Scioto Group reverses the permeability contrast, providing an impermeable reservoir combined with permeable barrier layers. All four tests are conducted with the vertical stress close to10 MPa. The detailed experimental conditions can be found in Appendix Table B-5.

Inspection of the results shows several similarities to cases with impermeable layers. For starters, Figure 3-14 shows that the experimental stages of PC-Scioto test #2019-06-07-1 have qualitatively similar geometry to impermeable cases, with these geometric conditions defining initiation, containment, and height growth phases and transitions from one phase to another with increasing wellbore pressure. The similarities continue upon inspection of the injection pressure and flow rate plot shown in Figure 3-15. The corresponding boundary conditions are given in Appendix Table B-5. Here the injection flow rates are basically below 0.05 ml/min, while the wellbore pressures are lower than 9.8 MPa. Then the flow rate rapidly increases from a few hundredths of an ml/min up to several tenths of an ml/min (i.e., a roughly one order of magnitude and relatively sudden increase). This onset of instability in height growth is sharp and unambiguous, similar to impermeable groups and unlike the gradual and somewhat ambiguous onset of height growth for the cases with a permeable reservoir layer. With that said, an interesting phenomenon that contrasts with all previously-described groups is that the flow rate is even slightly reduced when the wellbore pressure increases within a low level. One possible explanation of this phenomenon is that the flow rate for a fixed inlet pressure, PKN-shaped hydraulic fracture goes like $Ht^{\frac{1}{2}}$ [Bunger et al., 2013], where H is the fracture height. Thus, as long as H is maintained constant (containment case), the flow rate will decrease with time.

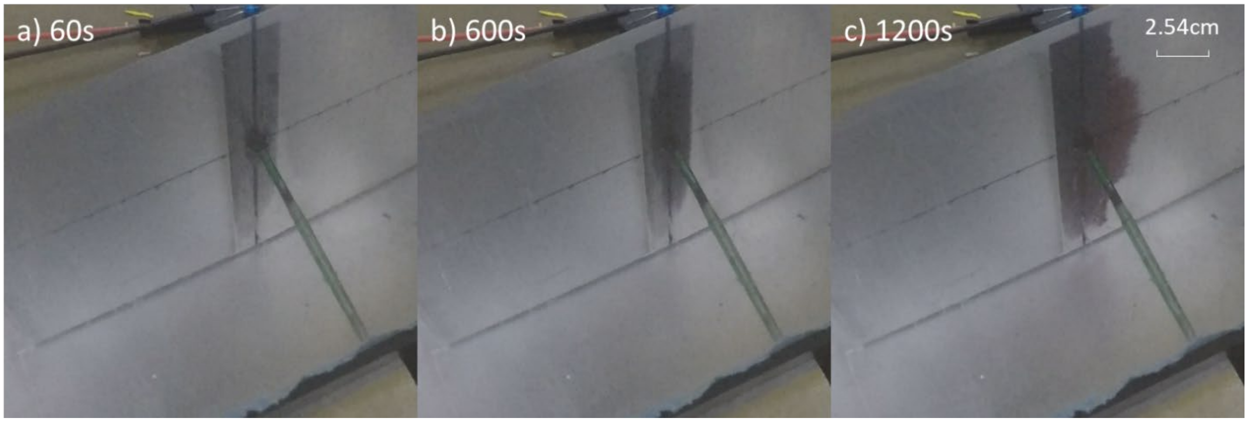

Figure 3-14. The progression of the PC-Scioto experiment(# 2019-06-07-1) at the moment a) fracture initiates at the 60s, b) fracture is contained within the reservoir layer at 600s, and c) fracture height growth takes place at 1200s.

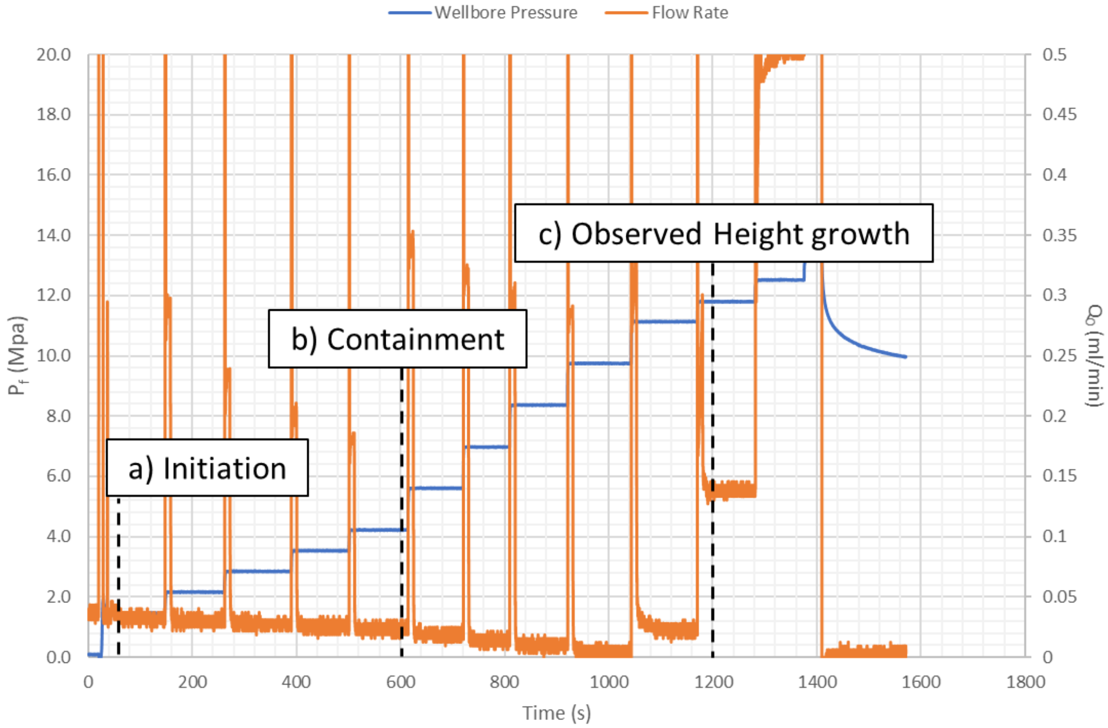

Figure 3-15. The injection plot of the PC-Scioto experiment (# 2019-06-07-1) includes the wellbore pressure P_f (MPa) and injection flow rate Q_0 (ml/min) versus the time (s). The video record shows an unstable fracture height growth occurs at approximately P_f =11.8 MPa.

The PC-Scioto group's critical wellbore pressure versus barrier stress plot is shown in Figure 3-16. Once again, the detail of the vertical stress value in MPa is denoted by the number next to each data point. It is evident that the critical wellbore pressures in the PC-Scioto group are significantly higher than the corresponding barrier stresses σ_b ($P_f - \sigma_b \approx 7.6$ MPa). Moreover, they are even higher than the PP-PMMA group's values. This result is probably primarily because Young's modulus ratio E_r/E_b of the PC-Scioto group is less than 0.5, which is even smaller than the value of the PP-PMMA group ($E_r/E_b = 0.61$). It is consistent with the previous observation that a softer reservoir material will increase the critical pressure that can induce unstable height growth.

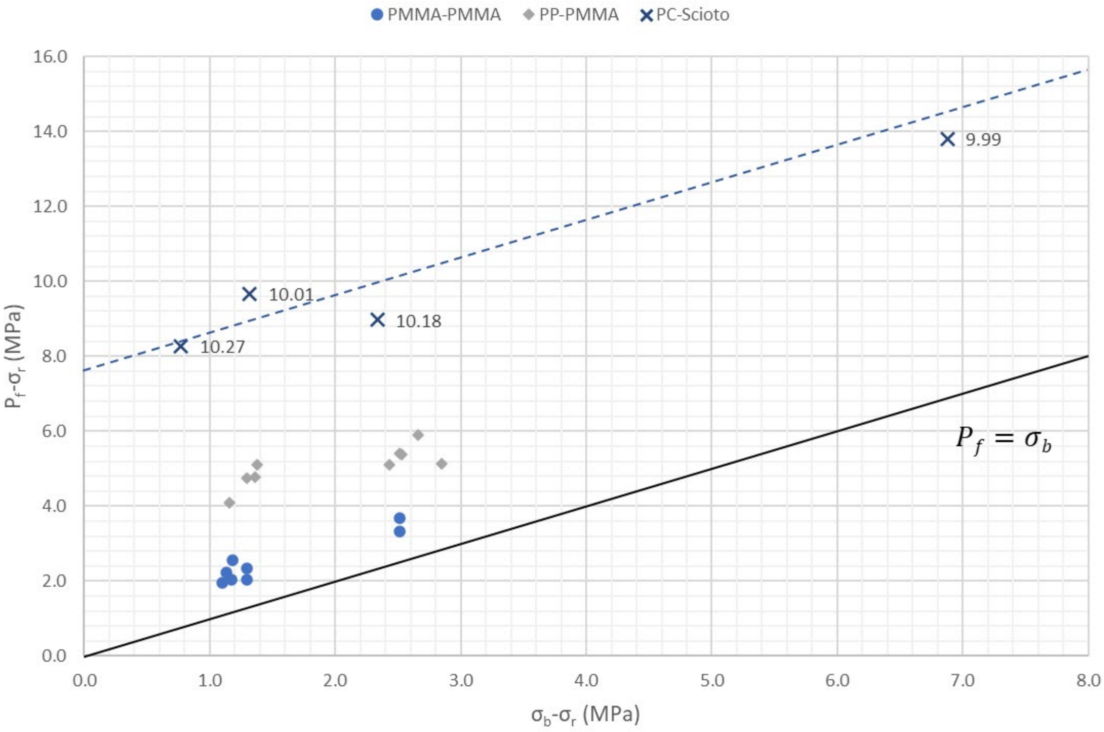

Figure 3-16. The PC-Scioto experimental group result shows that the critical wellbore pressures are distributed between the PMMA-PMMA and the PP-PMMA groups' values. The vertical stress value in MPa is denoted by the number next to each data point.

The critical pressures in Figure 3-16 basically continue the trend of Young's modulus impact. So, in this context, the relative contribution of the permeability appears to be small. And the presence of permeable barrier layers also does not appear to substantially increase the injectivity of the system, that is the flow rate obtained for a given wellbore pressure. So in some regards, the impact of the barrier permeability is not observed to be very strong. However, one potentially important behavior is that the permeable barrier material shortens the stable fracture height growth period. It can be seen by comparison to Figure 2-3b, where it is observed that previous groups show stable height growth over a certain range of wellbore pressure.

In contrast, once the fluid invasion of the barrier begins, the PC-Scioto cases exhibit a sudden transition to unstable growth with a very narrow range of stable height growth. It seems, then, that the permeable material suppresses the stable height growth period, perhaps by enabling loss of that fluid to leakoff. As a result, the first discernable transition from containment goes much more directly to unstable growth that outruns the ability of the permeable layer to diffuse the fluid away from the growing height.

3.4.3 Berea-Scioto Test

Previous experiment groups have established the basic ability to create hydraulic fractures in the configuration with permeable material in either reservoir or barrier layers. The final group considers a very high permeability reservoir and lower permeability barrier layers. In this Berea-Scioto group, the permeability contrast k_r/k_b is approximately 10^4. Two Berea-Scioto experiments were conducted with σ_r=2.76 MPa, σ_b=4.14 MPa, and σ_v=11.03 MPa. An example rock specimen and the experimental setup are shown in Figure 3-17.

Before going to the detailed results, it should be made clear that the large permeability of the Berea Sandstone led to extensive fluid invasion at low pressure and very low fracture efficiency at high pressure. Because the injection fluid dissipates into the rock matrix so fast, it is challenging to precisely analyze the data and quantitively compare it with other groups. However, we can still find several observations to be highlighted.

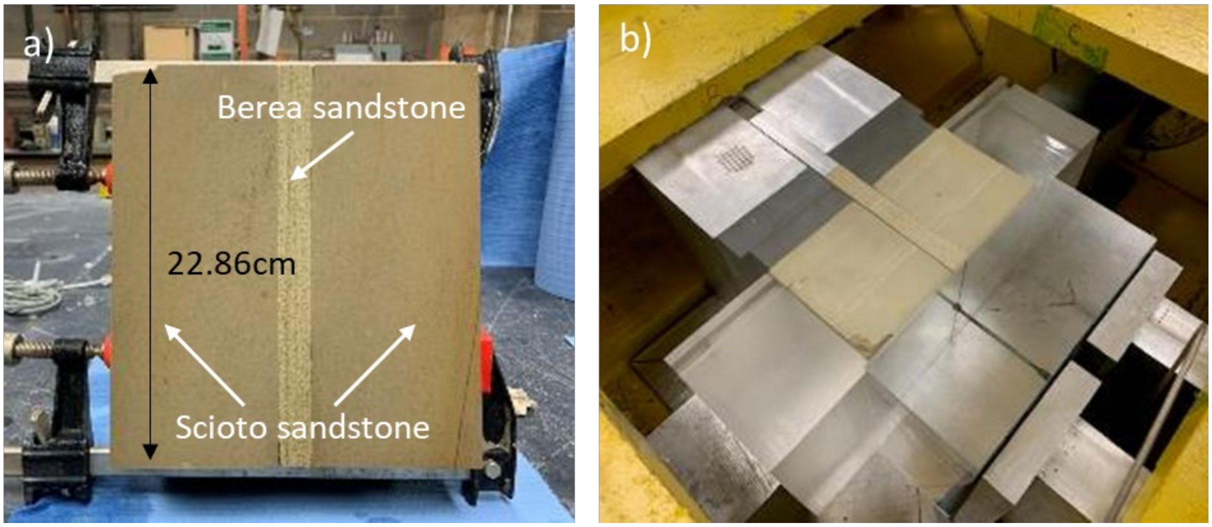

Figure 3-17 a) Three layers setup with Berea sandstone in the middle as reservoir layer and Scioto sandstone as barrier layers. b) The experimental setup for Berea-Scioto.

Figure 3-18 shows images of test #2019-04-25-1 conducted under 1.24 MPa constant injection pressure (schedule as 1.38 MPa). Correspondingly, Figure 3-19a illustrates the wellbore pressure and injection flow rate versus the time plot. These results show that the fluid reaches the wellbore head and initiates at 12 seconds (Figure 3-18a). Then, at 13 and 21 seconds, the fluid reaches the left (Figure 3-18b) and right (Figure 3-18c) interfaces, accompanied by two sudden flow rate increases, matching observations from other groups. Finally, the injection flow rate stabilizes at approximately 1.4 ml/min with a larger area growing in the lower permeability barrier layer, as shown in Figure 3-18d. Recalling that the case with a lower permeability reservoir comprised of the Scioto Sandstone (Figure 3-11), the injectivity for the case with Berea Sandstone is much higher, as is expected due to the high permeability of Berea sandstone. For comparison, Figure 3-19b shows the injection plot for test #2019-04-25-2, which applies a step injection rate that achieves a maximum of 7 ml/min. By both injection record and images of growth, the fracture progressions are similar to test #2019-04-25-1, except for the final fluid dissipated area.

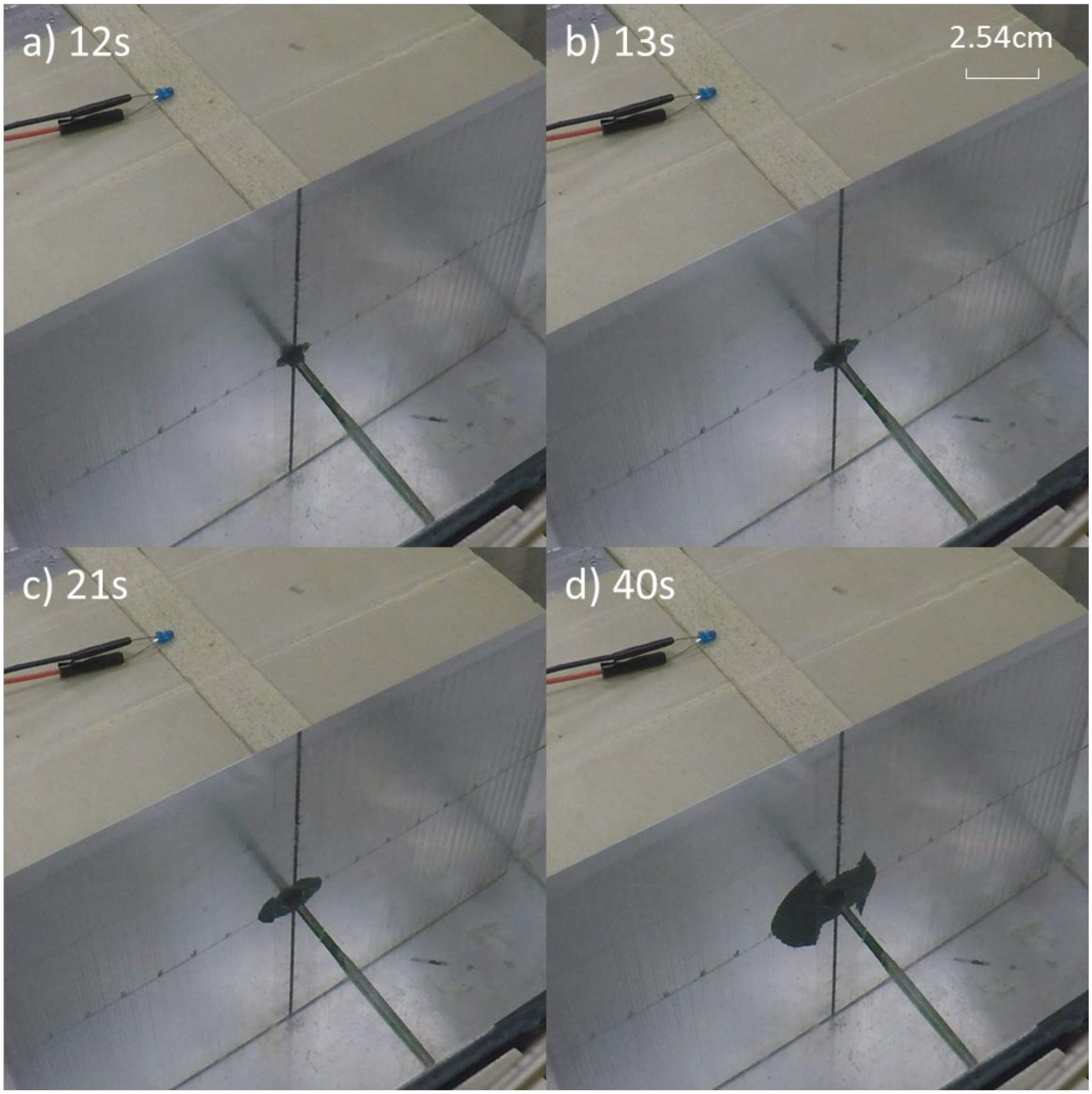

Figure 3-18: Images from a Berea-Scioto experiment #2019-04-25-1 conducted with 1.24 MPa constant injection pressure. a) fracture initiation. b) fluid reaches the left interface. c) fluid reaches the right interface. d) The injection fluid quickly dissipates from the reservoir into barrier layers in less than 1 minute.

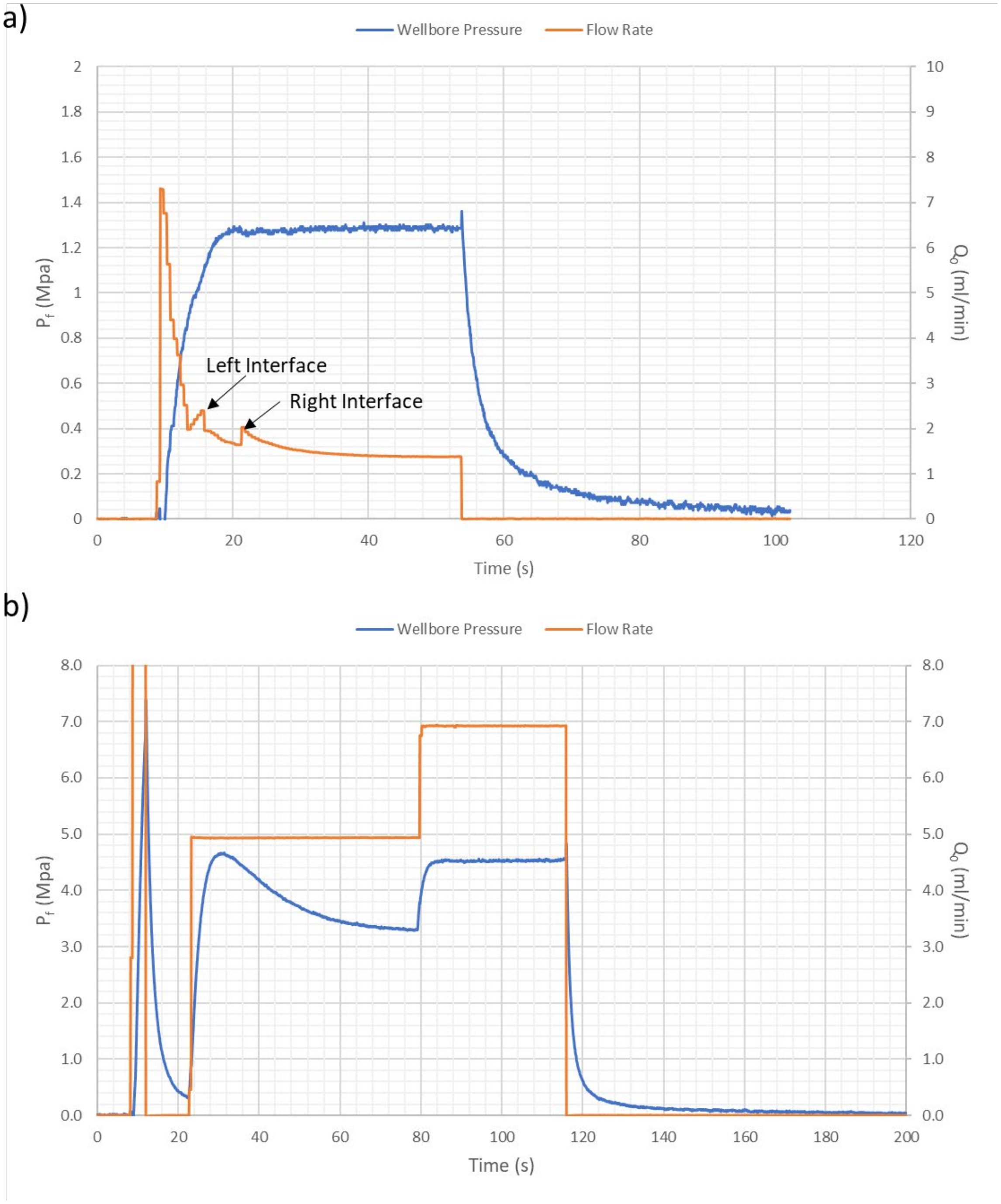

Figure 3-19. The injection plot of Berea-Scioto group a) test #2019-04-25-1 that is conducted with 1.24 MPa constant injection pressure. The injection flow rate stabilizes at 1.4 ml/min. b) test #2019-04-25-2, which is conducted with step flow rate injection. The test stabilizes at wellbore pressure around 4.6 MPa, corresponding to 7ml/min injection rate.

To more closely inspect the final fluid dissipation area, Figure 3-20 shows images of both Berea-Scioto specimens after unloading the system. These provide direct observation of the area into which the fluid has dissipated. Figure 3-20a shows the depth to which the fluid dissipates into the reservoir layer during low-rate test #2019-04-25-1, recalling that in this case, the injection pressure was fixed at 1.24 MPa, and the resulting injection rate steadied around 1.4 ml/min injection rate. Another view is given by Figure 3-20b, which shows the final fluid pattern formed in and on all three layers. In this case, the fluid's dissipation depth (x-direction, 3-20a) is close to the fracture length (y-direction) and vertical height (z-direction). In contrast, the results of fluid dissipation for higher rate test #2019-04-25-2 are shown in Figures 3-20 c and d. We can clearly see that the fluid invades a more extensive area. Furthermore, more fluid dissipates along the x-direction than the y and z directions. Finally, observation suggests that the fluid more easily diffuses into the Berea middle reservoir in-depth and through the pores rather than propagating in length or vertical directions.

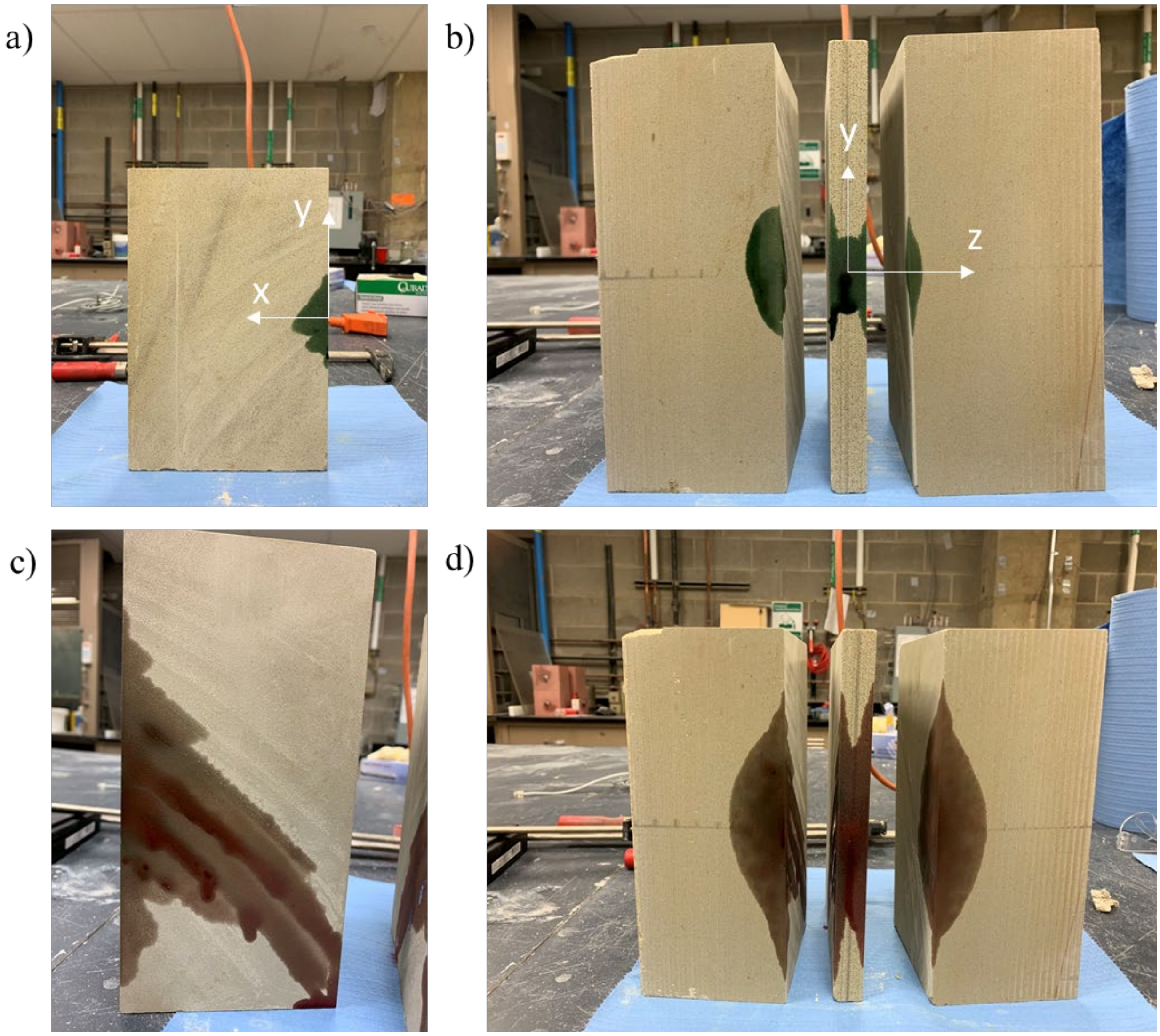

Figure 3-20. Injection fluid diffused into the permeable reservoir and barrier layers under a, b) 1.4 ml/min injection rate; c, d) 7 ml/min injection rate.

4.0 Numerical Simulation

One has a variety of possibilities for simulating hydraulic fracture growth in general and height growth in particular. The advantages and disadvantages of available approaches like Pseudo 3D and Planar 3D models are discussed already in Chapter 2. With that context and motivated by the experimental observations, it is considered essential that any model chosen for this work should be a fully-coupled hydraulic fracture model that allows fully three-dimensional growth, imposition of weak interface properties, and contrasting stresses and mechanical properties between the reservoir and barrier layers. Prior to a final selection of simulation platform, partial simulation of the problem based on fracture mechanics solutions provided initial insights regarding the impact of layering on the evolution of the stress intensity factor (Appendix A). However, considering the requirements of the simulator, the commercial lattice-based DEM simulator XSite [Damjanac et al., 2016] has been selected. Similar numerical modelings have also been tested by using the FEM simulator by applying cohesive zone theory. Compared with XSite modeling, the FEM simulator takes more computational resources to solve the problem under our specific configuration and boundary conditions. Thus, the XSite model might be an better option, and the implementation of the required model on this computational platform comprises the subject of this chapter.

4.1 XSite Simulation Mechanism

The commercially-available XSite simulator focuses on solving deformation and fracturing of the solid matrix in a distinct element method (DEM) approach [Damjanac et al., 2016]. It takes advantage of synthetic rock mass (SRM) [Pierce et al. 2007] and smooth joint model (SJM) concepts to further improve performance. Unlike the traditional DEM approach [Nagel N. et al., 2011; Nagel N. B. et al., 2013], it simulates the mechanical behavior of a fractured rock mass in a more efficient way, which overcomes the limitation of predefined fracture trajectories and interaction conditions [Damjanac & Cundall, 2016; Damjanac et al., 2016; Fu et al., 2019**Error! Bookmark not defined.**].

4.1.1 Lattice Model Methodology

The lattice model is essentially a set of nodes connected by 1D quasi-random arranged springs, as shown in Figure 4-1. Each pair of nodes is bonded by two springs. One represents the normal contact stiffness, and the other represents the shear contact stiffness. The model can be quickly discretized into numbers of small periodic bricks (p-brick), and each of those contains one or more matrix nodes. Meanwhile, those nodes are assigned to the positions corresponding to the centers of packed spheres, which used to be generated in PFC3D in periodic-space mode, with slightly varying radii relative to half of the lattice resolution. After that, the final model geometry can be achieved by trimming off the "excess" lattice extending outside the analyzed domain [Damjanac & Cundall, 2016]. Since the nodes are approximately uniformly-distributed within the p-brick, the mass of a node can be calculated by dividing the p-brick mass by the number of the nodes in it.

Once the model has been discretized, the simulation will be carried out by explicitly solving the motion equations (three translations and three rotations). For each node, the translational degrees of freedom can be expressed by combining the central difference equations of velocity and displacement:

$$\dot{u}_i^{t+\Delta t} = \dot{u}_i^{t-\Delta t} + \frac{\sum F_i^t \Delta t}{m} \qquad \text{Eq. 4-1}$$
$$u_i^{t+\Delta t} = u_i^t + \dot{u}_i^{t+\Delta t} \Delta t$$

Where $\dot{u}_i^t$ and u_i^t corresponds to the node velocity and displacement of component i (i = 1, 3) at time t. And the velocity change at each component can be expressed as the sum of all force components loading on the node with mass m, during the Δt time interval. In the meanwhile, the normal and shear spring force can be updated as

$$F^N \leftarrow F^N + \dot{u}^N k^N \Delta t \qquad \text{Eq. 4-2}$$
$$F_i^S \leftarrow F_i^S + \dot{u}_i^S k^S \Delta t$$

Here the "N" donates "normal" and "S" donates "shear". The spring force change equals the product of velocity, spring stiffness (normal stiffness k^N or shear stiffness k^S) and time interval Δt. Once the spring force exceeds the spring strength (normal or shear), both springs will be marked as broken, and a micro failure thus is generated. Correspondingly, both F^N and F^S will be set to zero, as long as the failure gap g is positive (the crack is open). When the crack is closed, and $g = 0$, Eq 4-2 can be re-applied for spring calculation which will lead to an aperture once the force becomes positive.

4.1.2 Smooth Joints Model

The pre-existing fractures or discontinuities (joints) in the XSite can be set up with flexible size and orientation. Each joint contains a planar array of bonds that obey the smooth joints model (SJM). As shown in Figure 4-1, the lattice springs cut through by the joint will be assigned as joint springs. Thus, the direction of those springs will no longer represent local orientation but the joint overall direction.

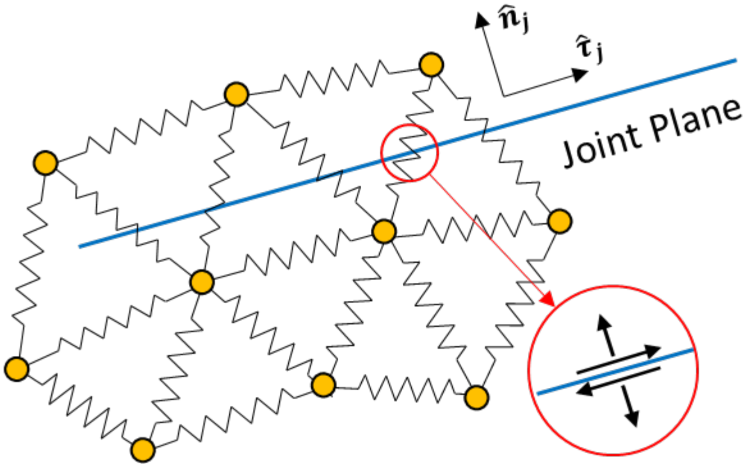

Figure 4-1. The schematic of the smooth joint model: The blue line represents the joint plane, which cuts through several joint springs connecting matrix nodes (green dots). The constitutive equations of each spring will be evaluated in ($\hat{n}_j, \hat{\tau}_j$) direction regardless its original connecting direction. Modified from Cundall [2011] as presented in Fu et al. [2019].

Based on [Cundall et al., 2011], the opening and slipping behaviors of an unbonded joint can be embodied as the limits of related joint spring forces following the relationship: If the hydraulic pressure p is large enough to overcome the normal compressive stress $\frac{F^n}{A}$

$$F^n - pA < 0 \Rightarrow F^n = 0, F_i^s = 0$$

else

$$F^n - pA \geq 0 \Rightarrow F_i^s = \frac{F_i^s}{|F_i^s|} \min\{(F^n - pA)tan\phi, |F_i^s|\}$$

Here, A is the apparent area of the joint segment, $tan\phi$ is the frictional coefficient between joint interfaces. For the first scenario, the joint will open with a fluid element inserted, and therefore shear force components F_i^s will go zero. Otherwise, the joint will remain closed, and the shear force components will be updated once the maximum shear strength $(F^n - pA)tan\phi$ less than the current shear component values.

4.1.3 Flow Model

Both fracture and matrix flow models are supported in XSite. Since current research focuses on the low permeability cases with negligible fluid leakoff, only the fracture flow model is discussed here. The fracture flow model can be applied in both pre-existing joints (bedding interfaces, natural fractures) and newly created joints (hydraulic fracture propagation). Figure 4-2 illustrates an equilibrium configuration as Figure 4-1 replaces the joint with the fluid nodes network (blue dots) connected by the one-dimensional flow pipe elements. The fluid pressures are stored in the fluid nodes that act as penny-shaped microcracks inserted into the middle of broken matrix springs and pre-existing joint springs (nodes 1~5). Once the hydraulic fracture propagates to the left side, and the spring mn is broken. A new fluid node (node 6) will be inserted into the middle of spring mn with certain fluid pressure and works as the new crack tip.

As the hydraulic fracture grows, the whole network will be updated iteratively when newly-formed microcracks are added. The classical lubrication equation Eq. 4-3 is utilized to evaluate the relationship between fracture flow rate and aperture. More specifically, the flow rate from node "A" to node "B" is calculated based on the equation:

$$q = \beta k_r \frac{a^3}{12\mu}[p^A - p^B + \rho_W g(z^A - z^B)] \qquad \text{Eq. 4-3}$$

Here a is hydraulic fracture aperture, μ and ρ_W correspond to fluid viscosity and density. p^A and p^B are fluid pressure of nodes "A" and "B", while z^A and z^B are the elevations of nodes "A" and "B" respectively. The relative permeability k_r is a function of saturation s, which can be expressed as:

$$k_r = s^2(3 - 2s) \qquad \text{Eq. 4-4}$$

where β is a dimensionless calibration parameter built into the XSite simulator and which is related to model resolution. The primary function of this parameter is to calibrate the conductivity of the fluid pipe network to the conductivity of the joint with an aperture equal to a.

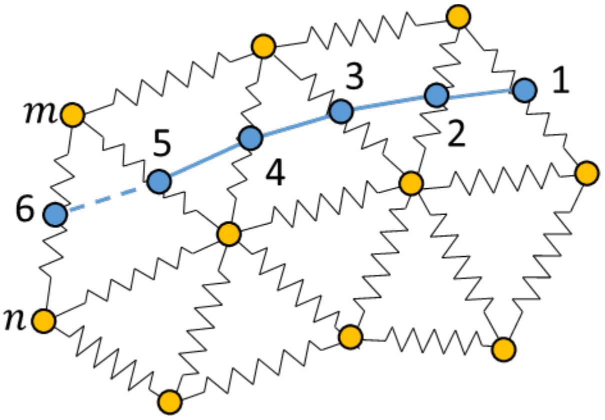

Figure 4-2. The equilibrium configuration of Figure 4-1. The fracture joint is replaced by discrete fluid nodes(blue dots) connected by flow pipes. An initial pressure input is assigned to pre-existing joints and new fluid nodes (No. 6), and pipes (dashed line) will be added to the network once springs break. Modified from Cundall [2011] as presented in Fu et al. [2019].

4.2 XSite Modeling of Infinite Homogeneous Case

4.2.1 Model Setup and Properties

The basic modeling configuration is set up based on the experimental lab scale with a dimension of 22.86×22.86×22.23 cm^3, as shown in Figure 4-3. The wellbore is arranged along the X-axis. Besides, a 0.003m radius injection cluster is assigned at the end of the wellbore, which is located at the modeling matrix's geometry centroid. For convenience, the injection cluster is taken as the coordinate origin for later demonstration. The pre-existing vertical joint is set along the Y-Z plane, penetrating the injection cluster perpendicular to the wellbore. The joint nodes are initialized with a 10^{-6} m aperture (the XSite minimum limit) and zero fluid pressure. To match the weak interfaces in the experiment, a "very weak" joint option is chosen (this is terminology from a drop-down menu in the XSite user interface), which has a negligible friction angle and zero tensile strength. Other physical properties setup of the joint is shown in Figure 4-4.

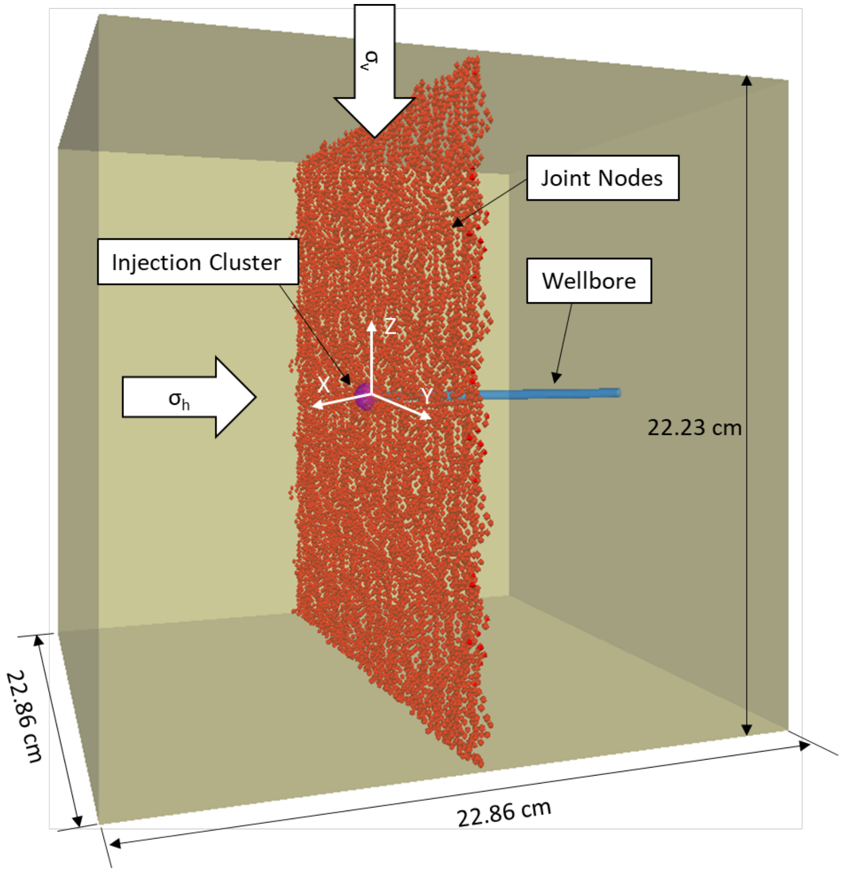

Figure 4-3. The demonstration of the basic modeling setup. The hydraulic fracture will propagate mainly within the vertical interface (Y-Z plane).

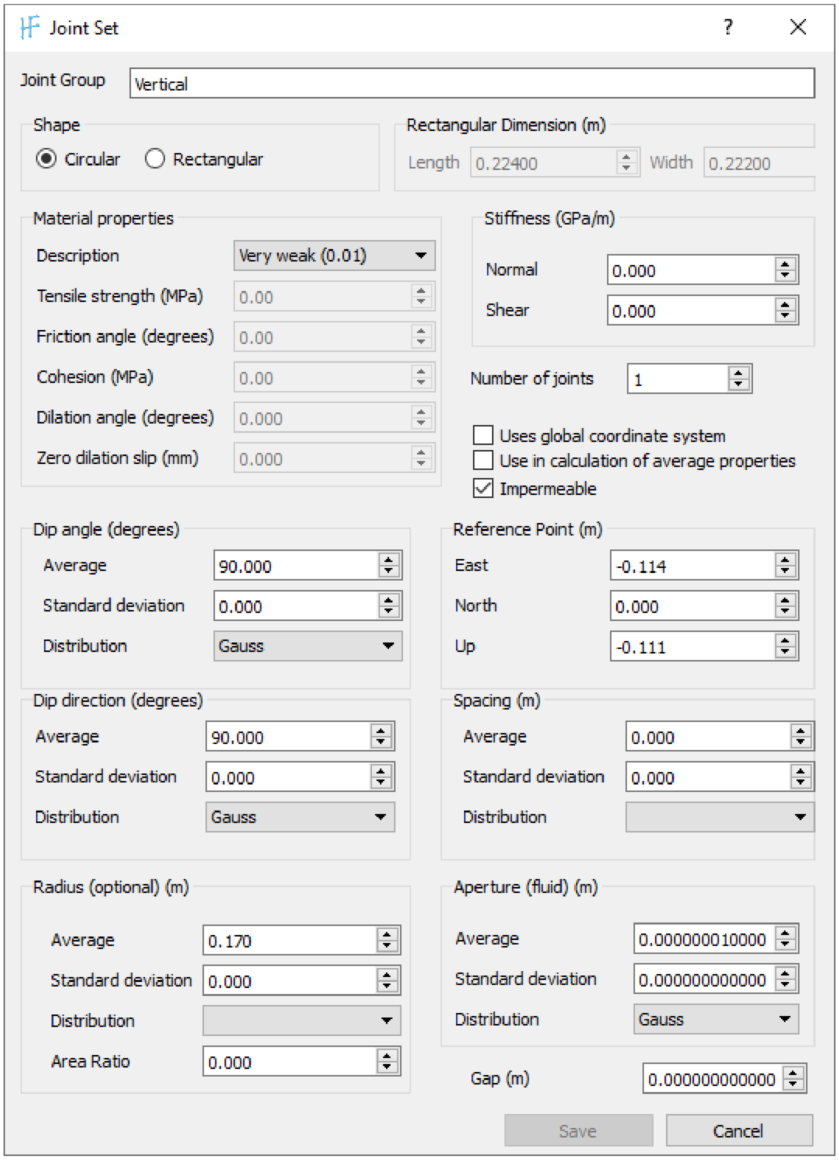

Joint Group: Vertical

Shape: ● Circular ○ Rectangular

Rectangular Dimension (m): Length 0.22400 Width 0.22200

Material properties

Description: Very weak (0.01)
Tensile strength (MPa): 0.00
Friction angle (degrees): 0.00
Cohesion (MPa): 0.00
Dilation angle (degrees): 0.000
Zero dilation slip (mm): 0.000

Stiffness (GPa/m)

Normal: 0.000
Shear: 0.000

Number of joints: 1

☐ Uses global coordinate system
☐ Use in calculation of average properties
☑ Impermeable

Dip angle (degrees)

Average: 90.000
Standard deviation: 0.000
Distribution: Gauss

Reference Point (m)

East: -0.114
North: 0.000
Up: -0.111

Dip direction (degrees)

Average: 90.000
Standard deviation: 0.000
Distribution: Gauss

Spacing (m)

Average: 0.000
Standard deviation: 0.000
Distribution:

Radius (optional) (m)

Average: 0.170
Standard deviation: 0.000
Distribution:
Area Ratio: 0.000

Aperture (fluid) (m)

Average: 0.000000010000
Standard deviation: 0.000000000000
Distribution: Gauss

Gap (m): 0.000000000000

Figure 4-4. The joint setup window shows the initialization properties.

The horizontal stress σ_h and vertical stress σ_v directions are also illustrated in Figure 4-3. The values of σ_h and σ_v stress are assigned explicitly before each simulation. Similar to the lab experiments in which the fracture will only propagate along with the pre-existing interfaces, the new fluid nodes are restricted to only be generated within a pre-defined joint. This is not a restriction of XSite, but rather a modeling choice made in order to have better similarity between the model and the experimental conditions. With this choice, the value of major horizontal stress σ_H perpendicular to the vertical X-Z plane is irrelevant to hydraulic fracture growth and so it can be given an arbitrary value that is kept constant across all simulations. Once the simulation is finished, the outputs are then imported into MATLAB for post-processing and visualization of quantities, including wellbore pressure P_f, fracture volume V_{total}, crack length l, and aperture W (which is also sometimes called the "width").

4.2.2 Validation for Circular Hydraulic Fracture

Many efforts have been made in previous research [Damjanac & Cundall, 2016, Fu et al., 2019, Xing et al., 2018b] to verify the accuracy of the XSite model. In our case, since we are applying different stress scales and specimen geometry, it is still necessary to validate the accuracy of this model before moving forward. The case that we validated is penny-shape hydraulic fracture propagation. Due to the hydraulic fracture growing along with pre-defined, zero toughness interfaces, the main mechanism of energy dissipation is associated with the viscous fluid flow. This scenario is also known as the viscosity-dominated regime [Detournay, 2004]. Thus, the basic idea is to benchmark the XSite simulation result of fracture opening width and pressure with the viscosity-dominated analytical solution driven by Savitski and Detournay [Savitski & Detournay, 2002]. To replicate experimental conditions, the material matrix is characterized by an elastic modulus equal to 3×10^9 Pa, and the Poisson's ratio equals 0.38. Additionally, the fluid is taken with 0.3 Pa·s viscosity and is injected at a constant 2×10^{-8} m^3/s flow rate.

Figure 4-5 illustrates an evenly distributed internal pressure around the wellbore after constant rate injection for 5 seconds. The wellbore pressure at this moment is approximately 4×10^6

Pa. Because the fracture is circular, for demonstration purposes, only the aperture and pressure data for nodes distributed at z = 0 (wellbore height) are picked to benchmark with the analytical solution. The result of this comparison is shown in Figure 4-6. Here the wellbore is located at r = 0, and nodes located to the left and right will have a negative and positive r, respectively. We can notice that the numerical results are symmetrical with respect to the wellbore and highly matched with the analytical solution except for the zone near the wellbore. The most likely reason is because of the geometry of the source owing to the fact that XSite has a finite wellbore size (injection from a finite source region), while the injection is taken to come from a point source in the analytical solution.

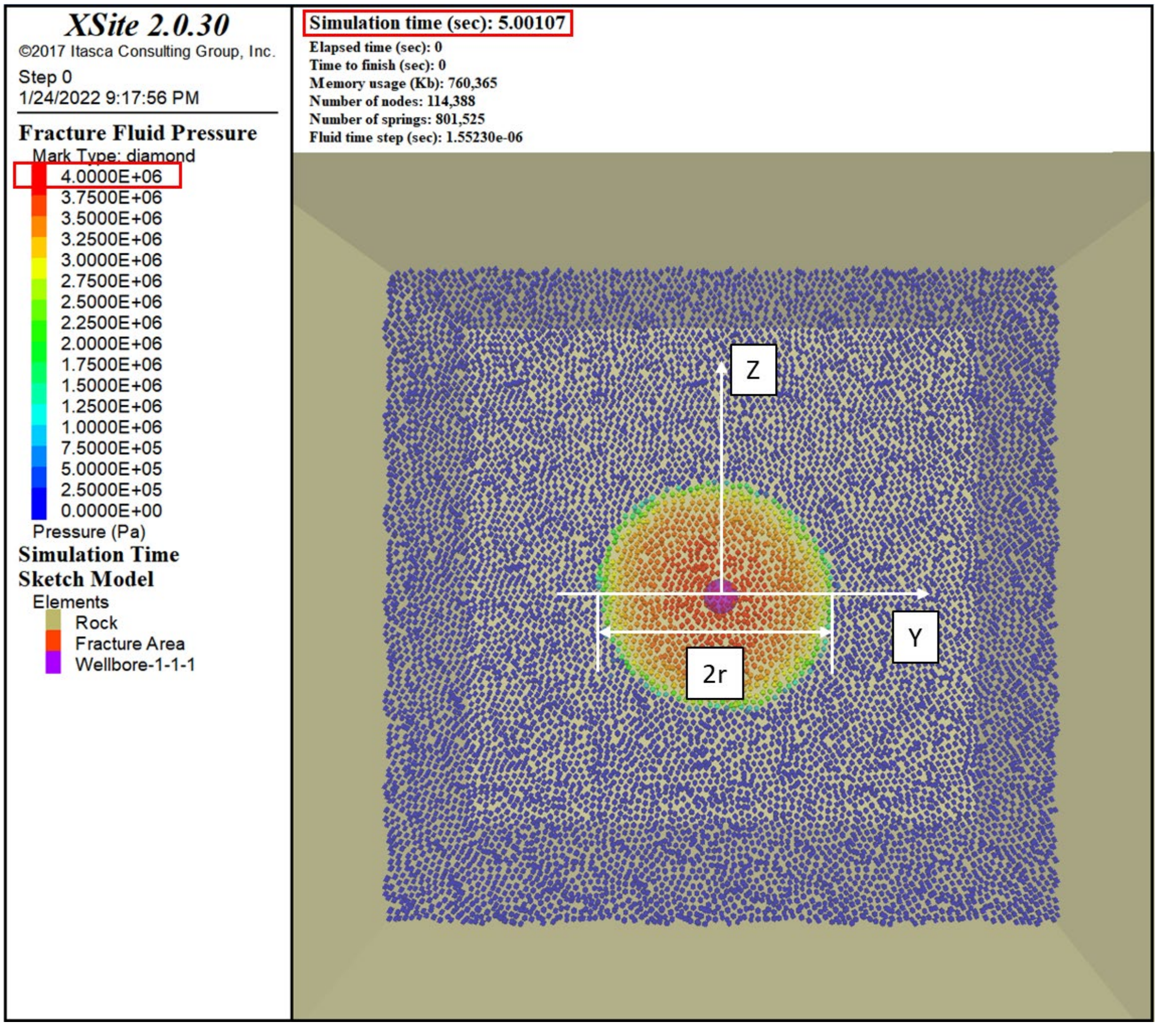

XSite 2.0.30
©2017 Itasca Consulting Group, Inc.
Step 0
1/24/2022 9:17:56 PM

Simulation time (sec): 5.00107
Elapsed time (sec): 0
Time to finish (sec): 0
Memory usage (Kb): 760,365
Number of nodes: 114,388
Number of springs: 801,525
Fluid time step (sec): 1.55230e-06

Figure 4-5. The XSite radial fracture simulation is carried out with constant flow injection for 5 seconds

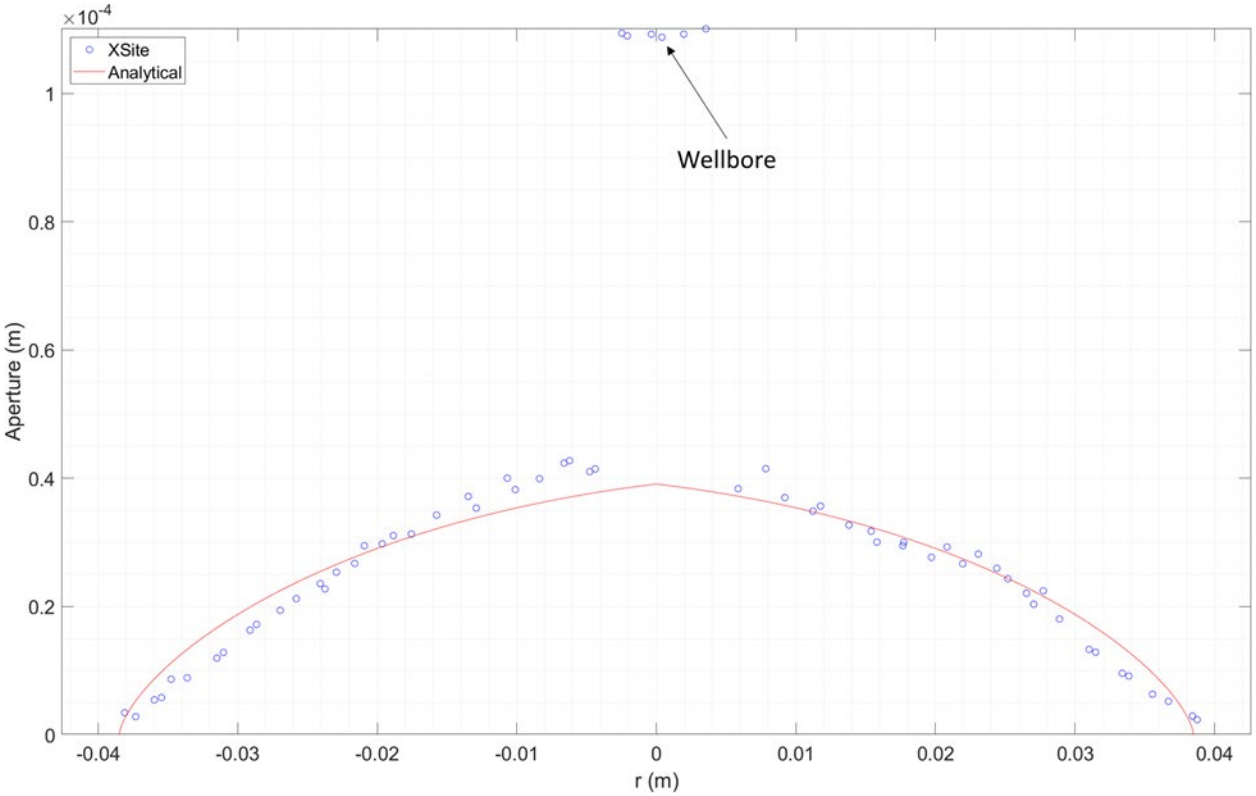

Figure 4-6. The benchmark result between XStite numerical solution and the analytical solution of Savitski & Detournay [2002] for fracture aperture.

4.3 Multi-layer Simulation

After validating the simulator's accuracy for the infinite domain, the next step is setting up multi-layer simulations. Based on the model setup demonstrated in Figure 4-3, two horizontal joints, which have identical properties to the vertical joint, are added along the X-Y plane, as shown in Figure 4-7. They work as free-sliding bedding interfaces and divide the matrix into three layers. Then, matrix materials and boundary conditions (stresses, injection flow rate) are assigned to each layer respectively before running the simulator.

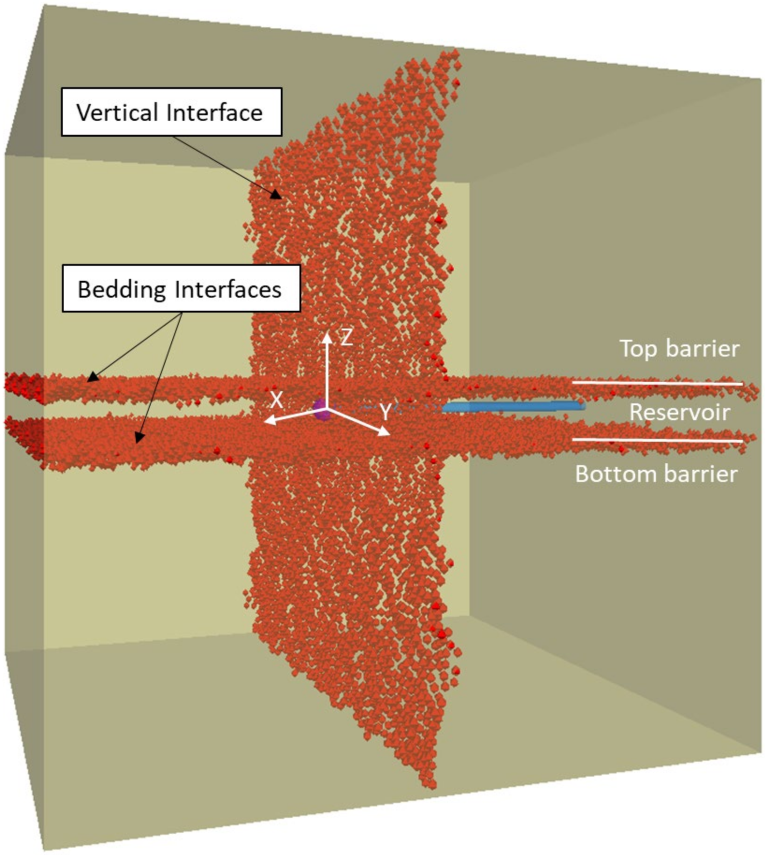

Figure 4-7. The demonstration of multi-layers modeling setup. Two bedding interfaces divide the basic configuration into three layers.

4.3.1 Enhanced Pseudo 3D Model Comparison

Benchmark solutions are not available for the three-layer case with weak interfaces and varying layer properties. However, to gain confidence in the model, it is useful to compare XSite modeling and enhanced Psuedo 3D (EP3D) modeling results using the approach of [Dontsov & Peirce 2015], and the detailed process can be found in the Supplementary Materials (Preface link). The EP3D model considers height growth under conditions where three layers have the same elastic properties. The reservoir layer has lower stress than the barrier layers. There is no weak interface between the layers. The EP3D approach is chosen for this comparison because of the ease of implementation and because it has been extensively benchmarked with high fidelity models [Dontsov & Peirce, 2015]. By making the interface strong in a three-layer system and setting all three layers to have the same elastic properties, XSite is set up for comparison to EP3D. For this comparison, parameters are chosen as $E = 3.2$ GPa, $2H = 0.019$ m, $v = 0.38$, $\mu = 0.3$ Pa.s, $Q_0 = 10^{-8}$ m^3/s. Besides, a horizontal stress contrast is applied with $\Delta\sigma = 1.38$ MPa (σ_r=2.76 MPa, σ_b=4.14 MPa).

Figure 4-8 shows the XSite fracture pressure distribution around the wellbore after constant rate injection for 4.8 seconds. Compared to Figure 4-5, which has uniform horizontal boundary stress ($\sigma_r=\sigma_b$), the fracture is distinctly suppressed in the z-direction, leading to an ellipse shape. The fracture aperture (width) is measured along a vertical line directed through the location of the injection point (z-axis) and compared with the EP3D results.

Figure 4-9 shows the XStite numerical solution (blue open circles) and the EP3D approximate solution (red line) of fracture aperture along the vertical direction. The XSite simulation is observed to be generally consistent with the EP3D result, noting that EP3D has been benchmarked to high fidelity Planar 3D simulations by [Dontsov & Peirce 2015]. It is also apparent that the apertures of the XSite simulation are not smooth, and there is a slight favoring of growth to the right side. Both of these are likely due to perturbations of the solution arising from the quasi-random arrangement of the springs. Nonetheless, the overall behavior illustrated by the contour of the XSite simulation is consistent with the EP3D solution.

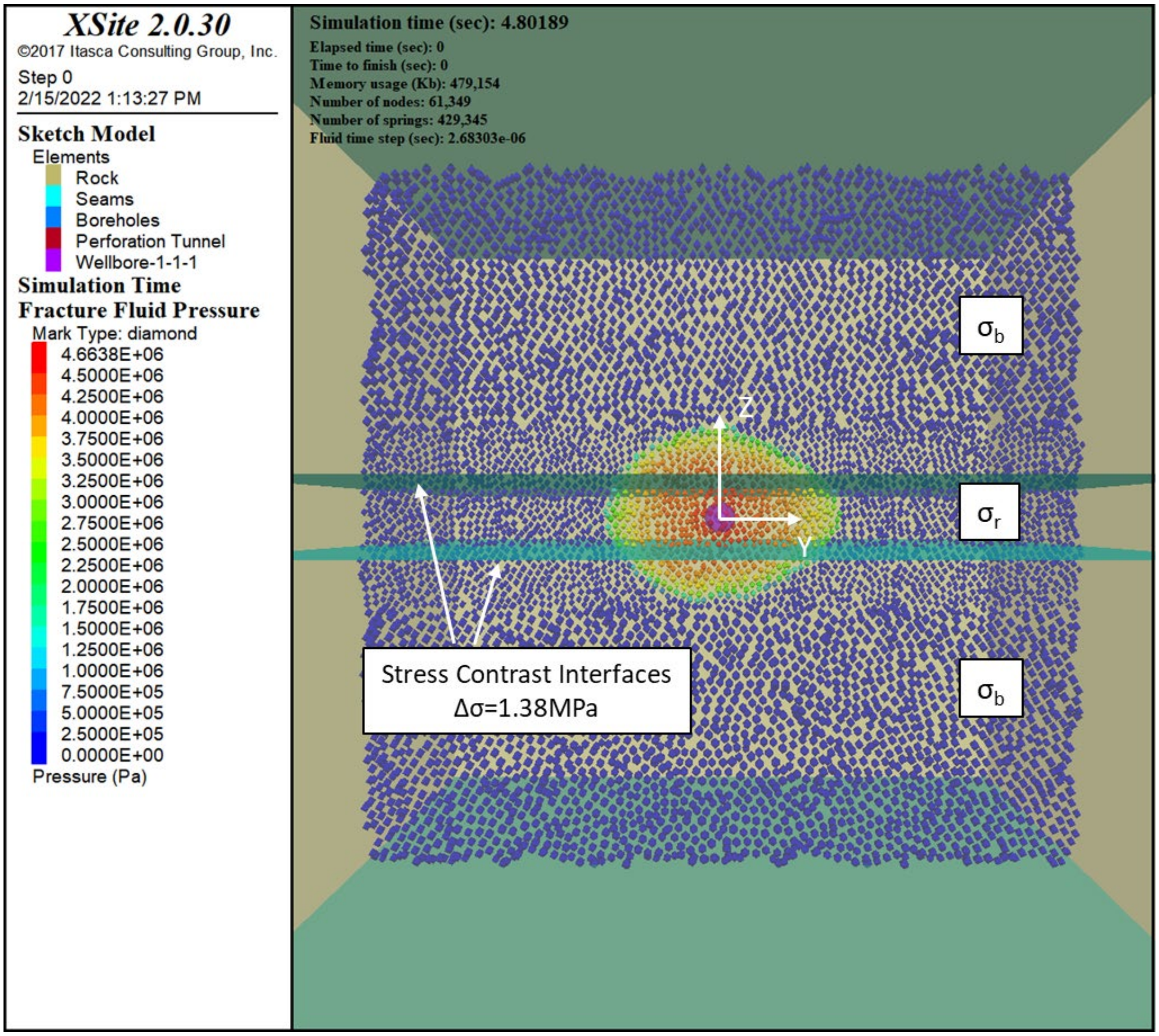

Figure 4-8. XSite modeling of hydraulic fracture propagation under stress contrast case with no weak interface between layers. The simulation is carried out with constant flow injection for 4.8 seconds.

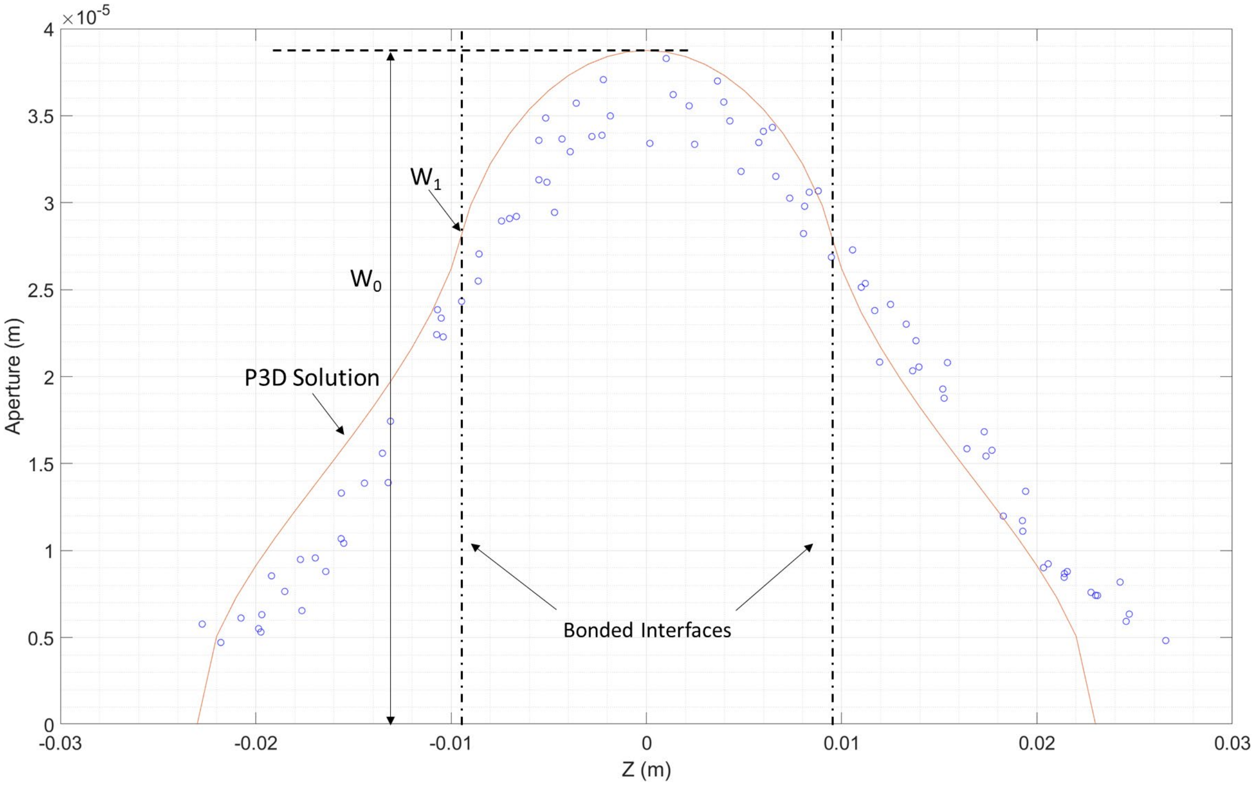

Figure 4-9. Comparison of the fracture aperture along vertical direction between XStite numerical solution and the EP3D solution [Dontsov & Peirce 2015].

4.3.2 Impact of Weak Interfaces

By switching the interfaces between the reservoir and barriers to be very weak, the impact of the interfaces becomes clear. For reference, an EP3D solution will again be included, noting that it represents the case with strong interfaces (i.e., no opening or sliding on the interfaces between the layers). Again using the fracture aperture along the vertical direction (z-direction), a comparison between the EP3D model (bonded interfaces) and XSite simulation with free-sliding interfaces is shown in Figure 4-10. Same parameters are unchanged from the previous EP3D comparison ($E = 3.2$ GPa, $2H = 0.019$ m, $\nu = 0.38$, $\mu = 0.3$ Pa.s, $Q_0 = 10^{-8}$ m^3/s, $\Delta\sigma = 1.38$ MPa) so that the only change is the addition of very weak interfaces in the XSite model. The comparison shows that if the barrier layer and reservoir are firmly bonded without any relative sliding, the fracture aperture (width) profile is smoothly continuous with the maximum value for this laboratory-scale simulation given by W_0=3.9×10^{-5} m. The maximum width of the barrier layers W_1 can reach a maximum of 2.9×10^{-5} m. However, once bedding interfaces are added, the fracture width within the reservoir layer increases dramatically, reaching an average value of 7.8×10^{-5} m. At the same time, the opening in the barrier layers drops below 10^{-5} m.

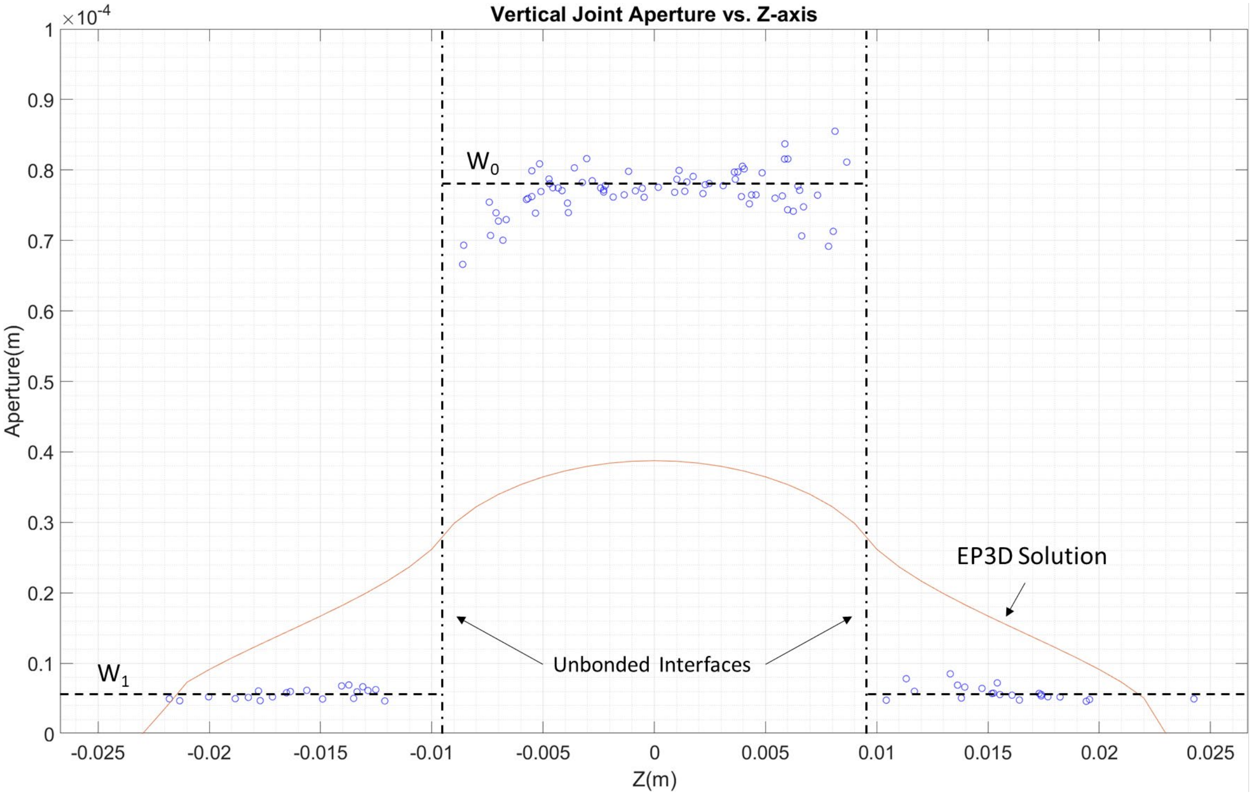

Figure 4-10. Comparison of EP3D and XSite solutions for a case with the same fracture height growth but different behavior due to the weak interfaces in the XSite solution. The EP3D represents the scenario in which no bedding interfaces exist (solid line), while the XSite result represents the case in which the bedding interfaces are weak and accommodate sliding deformation.

The high fracture aperture contrast between the reservoir and barrier layer indicates that most injection fluid is contained within the reservoir layer. This tendency of the weak interfaces to reduce the volume of the fluid penetrating to the barriers is broadly consistent with (and perhaps a cause of) the experimental observation that bedding interfaces enlarge the critical wellbore pressure required for unstable fracture height growth. Here, the numerical result shows that even if the fracture reaches the same height, the fracture opening in the barrier layers will be suppressed due to the bedding interfaces, and so by this mechanism of interface sliding, the bedding interfaces will limit the fracture height growth.

An illustrative sketch of this mechanism of interface sliding is shown in Figure 4-11. The left configuration represents the case with frictionless interfaces, which have the largest relative shifting and smallest barrier fracture aperture. In contrast, the right configuration represents the case with infinite high friction interfaces. It has a continuous fracture aperture across the interface with negligible sliding. In reality, our lab experiments can likely be represented by the middle configuration, which has a finite friction angle.

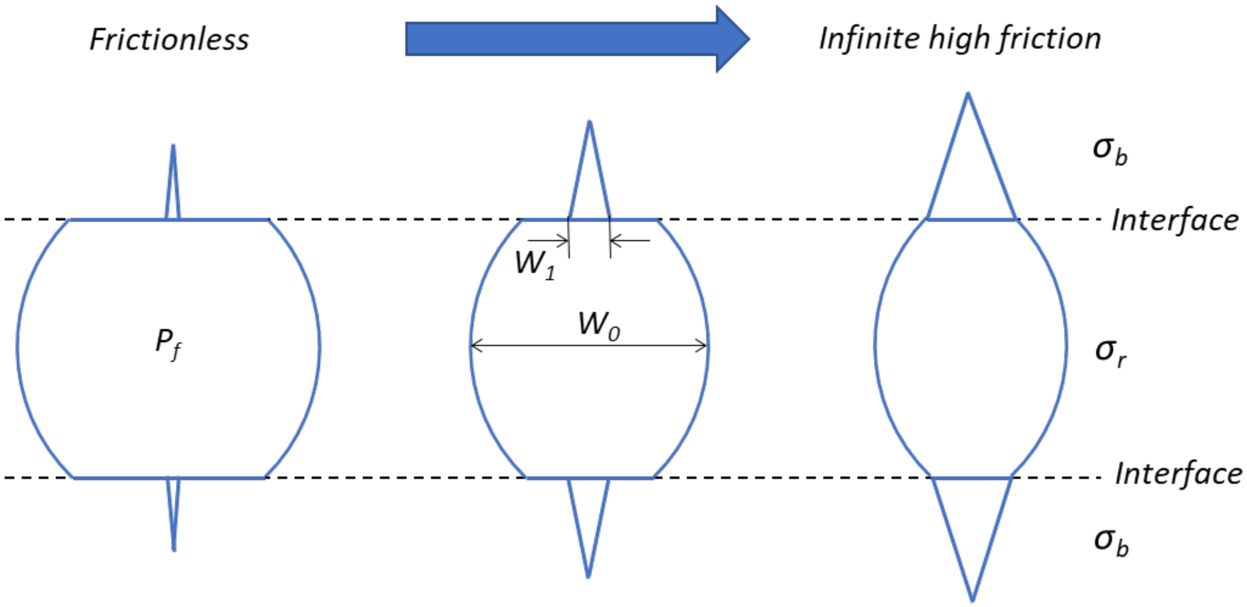

Figure 4-11. Impact of interface sliding on fracture width between the reservoir and barrier layers, showing (from left to right) frictionless interfaces, finite friction interfaces, and infinite friction interfaces.

5.0 Numerical Simulation of Experiments

5.1 Enabling Model-Experiment Comparisons

Before going into the details of simulations of laboratory-scale cases, it is important first to discuss and address some challenges to obtaining consistency between conditions encountered in the laboratory and what can be relized by XSite modeling owing to the fact that XSite has several limitations making it impossible to perfectly replicate the experimental injection and boundary conditions. Two main differences are:

1. The lab experiments involve applying a step-pressure injection schedule. However, the XSite simulator does not allow wellbore pressure-related boundary conditions but instead only allows constant influx conditions.
2. During each lab experiment, the injection process lasted until the unstable height growth was ascertained from observations. However, in most cases, the fluid had already reached the horizontal edges by this point in the experiment. Ideally, one would replicate this in the simulations with a permeable boundary at the edge of the specimen where the pressure can be fixed to match atmospheric pressure. However, the XSite simulator only applies a sealed boundary condition that does not allow fluid flow out of the boundaries of the model. Consequently, when the fluid reaches the boundary, the fluid will accumulate in the reservoir. Eventually, it is forced to drive height growth into barrier layers for lack of any other place to go.

The second mismatch issue between boundary conditions is addressed by ceasing fluid injection in the model when the fluid reaches the boundary, as sketched in Figure 5-1. Comparison between model and experiment is then enabled by extracting hydraulic fracture geometry from the data at exactly this moment when the fracture first reaches the boundary of the specimen.

To enable the comparison between experiments and data, it is necessary to define parameters that quantify observed fracture geometry. By reference to an idealized sketch of this fracture geometry given by Figure 5-1, the approximation of fracture half-height h can be extracted by referring to the scale on the observation block. The wellbore pressure at this moment is recorded as P_f. Then, the fracture height growth within the barrier layer ΔH can be calculated by subtracting half reservoir thickness H from total height growth, that is

$$\Delta H = h - H \qquad \text{Eq. 5-1}$$

To provide a convenient way to explore trends in the data, it is useful to define a dimensionless parameter relative height λ representing the normalization of ΔH with H, that is

$$\lambda = \frac{\Delta H}{H} \qquad \text{Eq. 5-2}$$

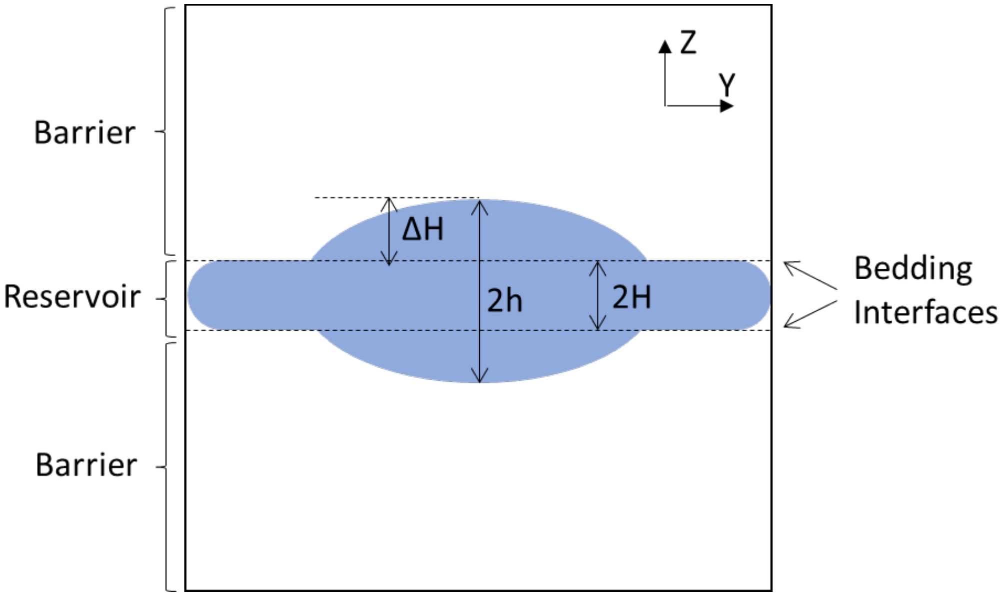

Figure 5-1. 2D planar cross-section illustrates the fracture geometry at the moment the fracture reaches the boundary.

Returning now to the two main issues regarding the applicability of the model to the experiments. To aid the resolution of the first issue, that XSite can not apply constant wellbore pressure, it is found to be effective to run multiple numerical simulations with identical boundary stresses as each laboratory experiment. Each numerical simulation is performed with a different constant injection rate and allowed to run until the horizontal fracture tip reaches the matrix bound. This enables the exploration of trends via postprocessing. Even though we will not have a direct comparison with each lab experiment, it is at least possible to ascertain how well the numerical simulations resemble key features of the observed data.

5.2 Comparison of Height Growth: PMMA-PMMA Case

An illustrative example of a PMMA-PMMA laboratory experiment (# 2020-01-15-3) is shown in Figure 5-2. From photo-based measurements, it is observed for this specific test that once the injection fluid reaches the horizontal boundary, the fracture has propagated approximately 2.1 cm in the vertical direction on one side. Then the λ value can be calculated as:

$$\lambda = \frac{\Delta H}{H} = \frac{2.10 - 0.95}{0.95} = 1.2$$

Moreover, the wellbore pressure at this moment is 4.83 MPa. Per the approach outlined in the previous section, corresponding to this laboratory experiment, four XSite simulations are performed with injection rates Q_0 equal to 1×10^{-8} m^3/s, 2×10^{-8} m^3/s, $5\times10^{-8} m^3/s$, $1\times10^{-7} m^3/s$, and $1.5\times10^{-7} m^3/s$. For demonstration purposes, the spatial distribution of fluid pressure when the fracture reaches the specimen boundary is shown for $Q_0 = 1\times10^{-8}$ m^3/s and $1\times10^{-7} m^3/s$ cases in Figures 5-3 and 5-4. From these, the pressure distribution and fracture height are apparent.

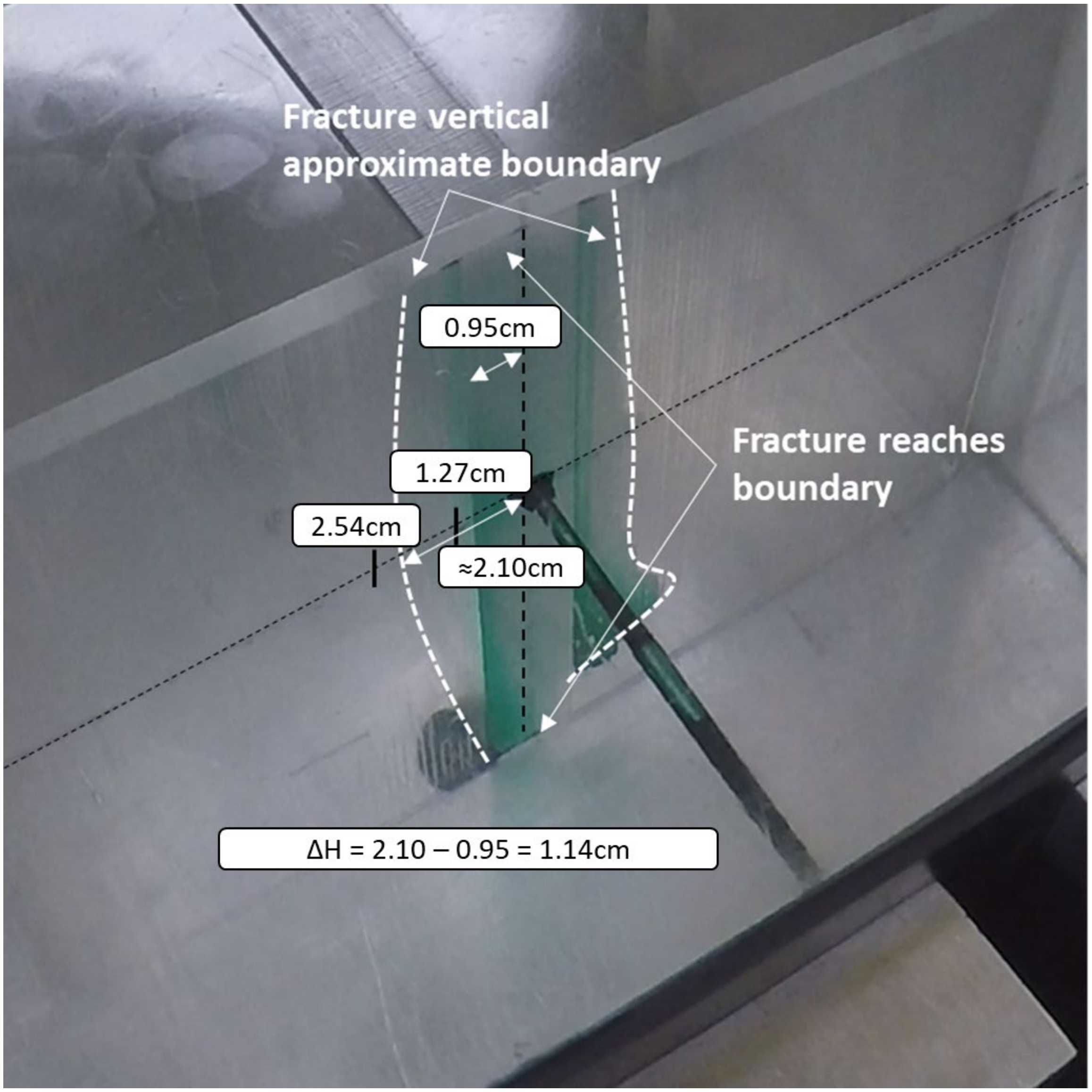

Figure 5-2. A laboratory experiment example shows when the fluid first reaches the horizontal boundary. Note that since the fracture tip aperture (width) is tiny, the color dye in the injection fluid is not significantly distinguishable from the figure. Thus, a dashed line roughly depicts the hydraulic fracture front.

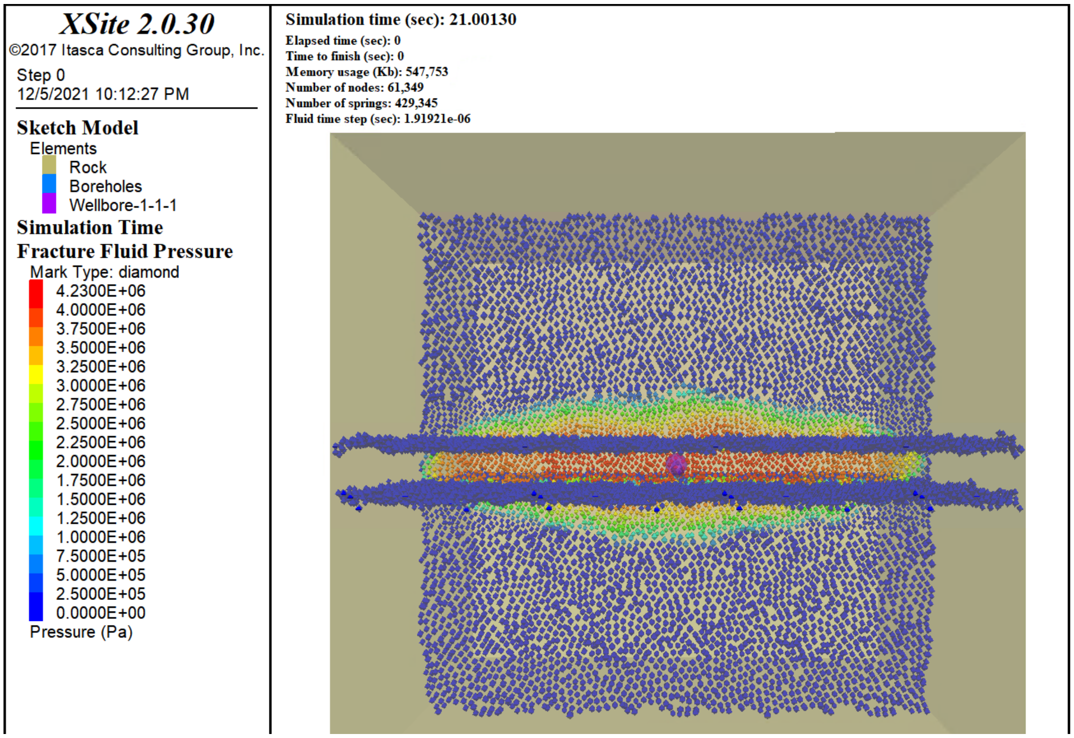

Simulation time (sec): 21.00130
Elapsed time (sec): 0
Time to finish (sec): 0
Memory usage (Kb): 547,753
Number of nodes: 61,349
Number of springs: 429,345
Fluid time step (sec): 1.91921e-06

Figure 5-3. XSite simulation example has a 1×10^{-8} m^3/s constant injection rate and lasts for 21 seconds.

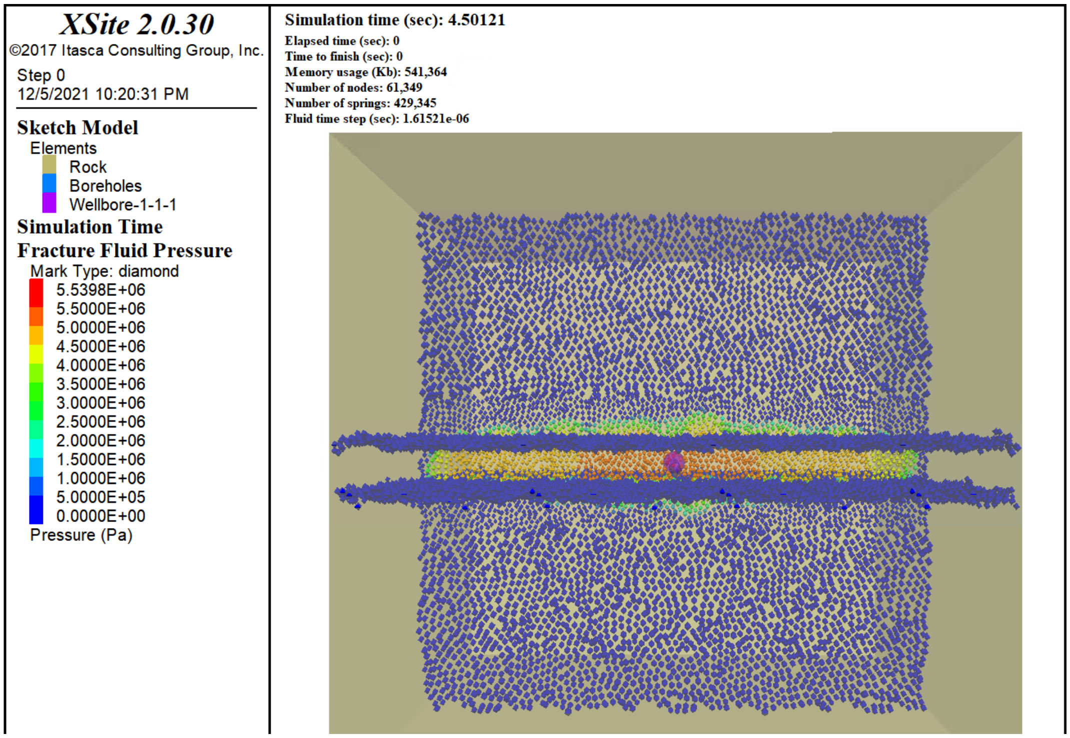

Simulation time (sec): 4.50121
Elapsed time (sec): 0
Time to finish (sec): 0
Memory usage (Kb): 541,364
Number of nodes: 61,349
Number of springs: 429,345
Fluid time step (sec): 1.61521e-06

Figure 5-4. XSite simulation example has a 1×10^{-7} m^3/s constant injection rate and lasts for 4.5 seconds.

The fracture aperture W distribution along the Y and Z axis with 10^{-8} ml/min and 10^{-7} ml/min injection rates are shown in Figure 5-5 and Figure 5-6, respectively. The blue dots represent the nodes' aperture variation. These are shown along the Y-axis (fracture horizontal propagation direction) at z = 0 in Figures 5-5a and 5-6a and along the Z-axis at y = 0 (vertical direction through the wellbore) in Figure 5-5b and 5-6b. Again, the simulation result dots are not distributed evenly along the axis due to the quasi-random arranged springs mechanism.

From Figure 5-5a and Figure 5-6a, it is observed that the hydraulic fracture reaches the horizontal boundary ($l \approx 0.22m$) for both tests. However, it takes 21 seconds for the low injection rate fracture to reach the horizontal boundary. In contrast, intersecting the same boundary takes 4.5 seconds for the high injection case. In the meantime, there is a significant difference between the vertical fracture growth, as shown in Figures 5-5b and 5-6b. The low injection case has a total fracture height of 0.044m, which decreases to 0.038m in the high injection case.

Then, following the steps demonstrated above, we can calculate the λ for all four simulation tests. For convenience, we can define net wellbore pressure P_{net} and the critical net pressure $P_{net,c}$

$$P_{net} = P_f - \sigma_r \qquad \text{Eq. 5-3}$$

$$P_{net,c} = P_{fc} - \sigma_r \qquad \text{Eq. 5-4}$$

With these definitions, the normalized height $\lambda = h / H$ versus P_{net} plot is shown in Figure 5-7. The solid point represents the lab measurement, while the open points represent the XSite numerical results. The comparison shows that the measurement for fracture height and injection pressure, taken when the fracture arrives at the specimen boundary, provides a point that lies roughly within the trend of the model predictions.

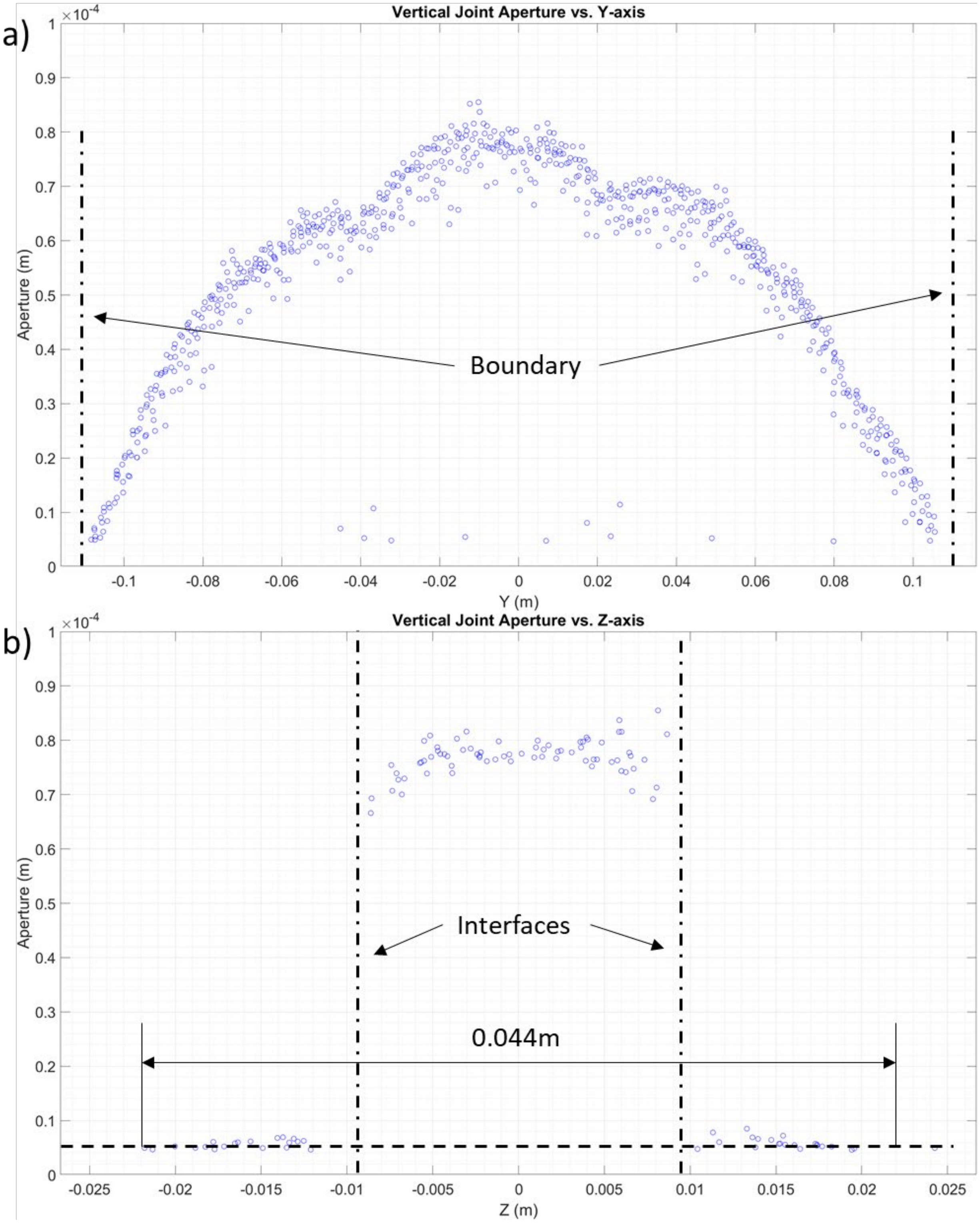

Figure 5-5. The simulation result of PMMA-PMMA test #2020-01-15-3 (Appendix Table B-1) with a low injection rate (1×10^{-8} m^3/s) shows fracture aperture along with a) Y-axis and b) Z-axis.

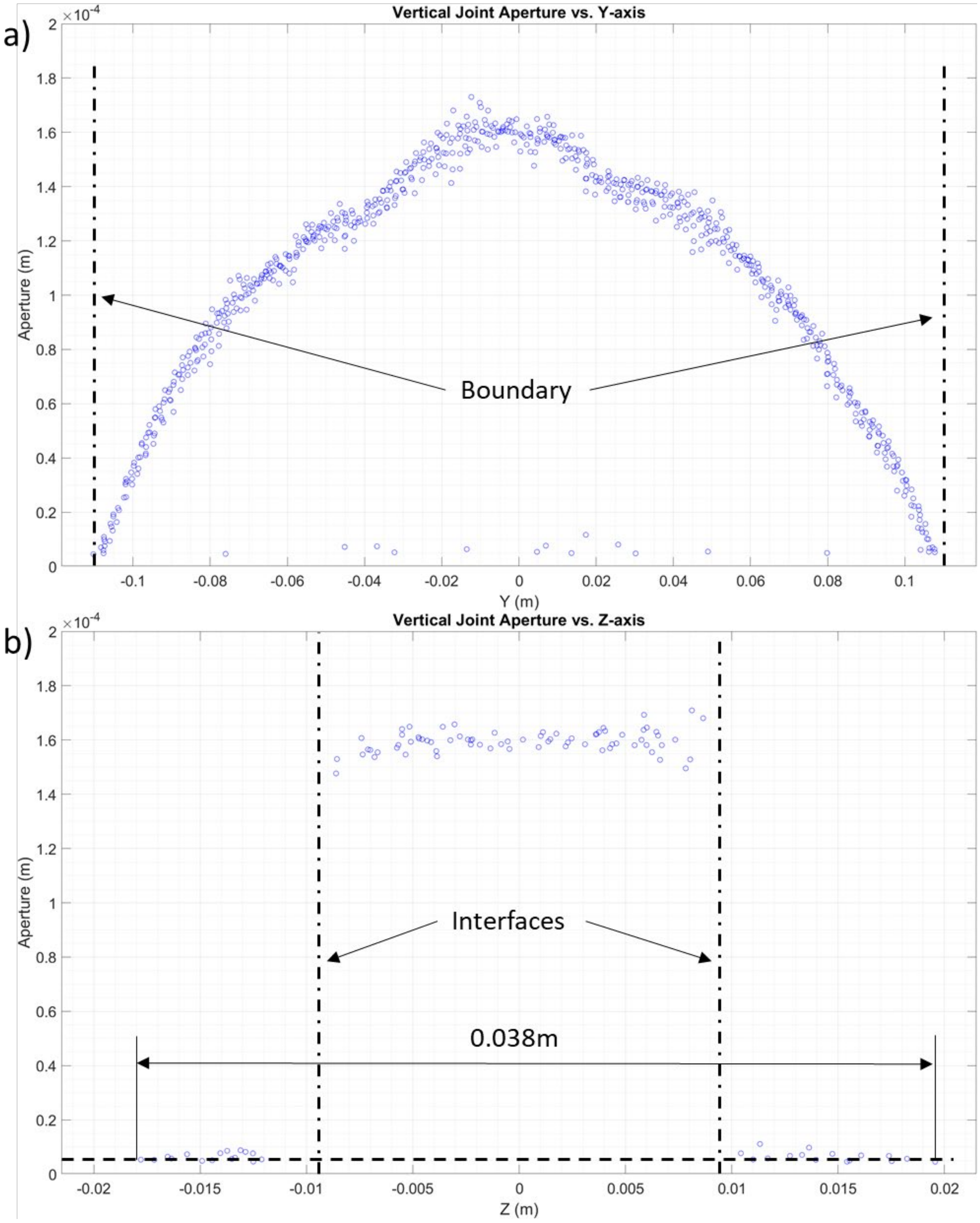

Figure 5-6 The simulation result of PMMA-PMMA test 2020-01-15-3 (Appendix Table B-1) with a <u>high injection rate</u> (1×10^{-7} m^3/s) shows fracture aperture along with a) Y-axis and b) Z-axis.

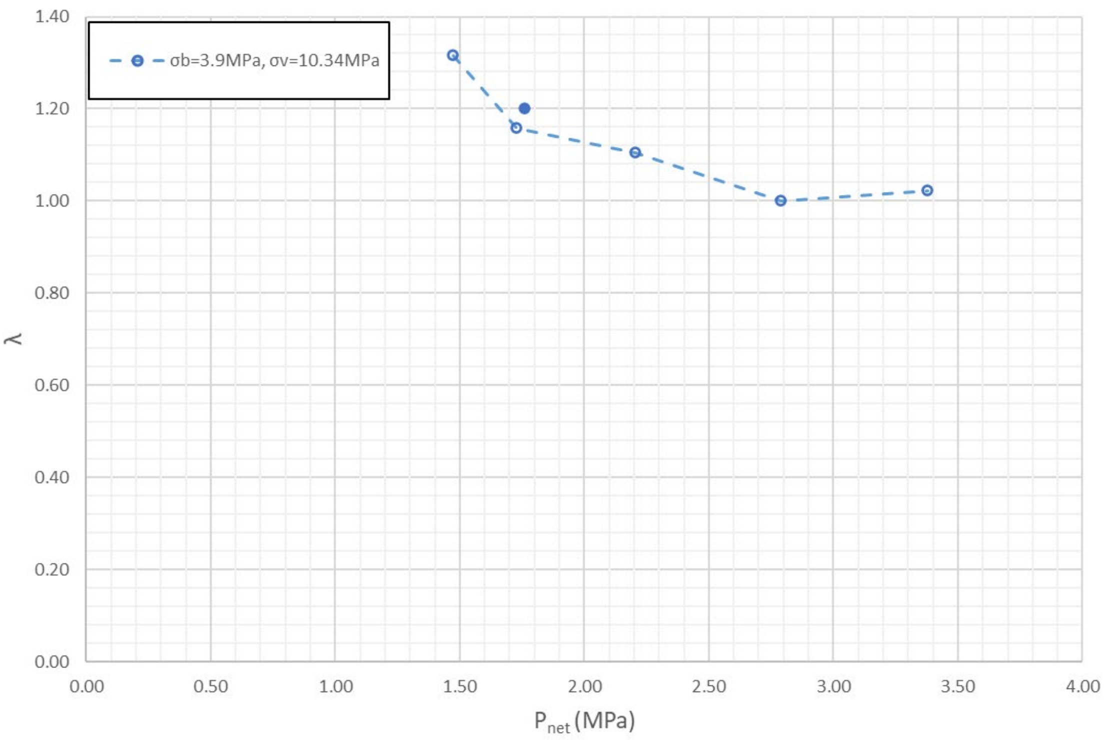

Figure 5-7. The λ versus H_b plot for the PMMA-PMMA test # 2020-01-15-3. The solid point represents the experimental measurement, while the open points represent the XSite numerical results.

5.3 Behavior of the Fracture Width

Fracture width is another part of the fracture behavior that can bring insight when it is carefully considered. More specifically, it is helpful to evaluate the trend of the maximum fracture width in reservoir layer W_0 (average crack opening within the reservoir) and the maximum fracture width in barrier layers W_1, including the ratio of these quantities.

The available simulations provide the ability to explore details of how stresses impact the fracture width. As previously discussed, cases are run to coincide with laboratory cases, although with the constant injection rates. This enables examination that is not possible with the laboratory observations alone. The complete width dataset for all cases is shown in Appendix Table C-1. Based on this data, Figures 5-8 and 5-9 illustrate the relationship between maximum reservoir width at the wellbore W_0 and maximum barrier width W_1 to the wellbore net pressure, respectively. Figure 5-8 shows that the reservoir widths (W_0) follow an approximately linear relationship with the wellbore pressure. In the meantime, the vertical stress has a minor impact on the W_0, which will be slightly reduced as vertical stress increases. Furthermore, it is striking that there is almost no sensitivity of the results to a change in barrier stress from 3.9 MPa to 5.24MPa. In other words, the barrier stress has barely any effect on the maximum reservoir width, showing that the elastic coupling between the barrier and the reservoir is diminished. In contrast, the classical P3D model applies governing equation

$$W = \frac{4}{\pi E'}[P_{net}\int_0^H G(s,z)ds + (P_{net} - \Delta\sigma)\int_H^h G(s,z)ds] \qquad \text{Eq. 5-5}$$

where $E'=E/(1-v^2)$ is the plane strain Young's modulus, $G(s,z)$ is the elasticity kernel [Adachi et al., 2010]. Eq 5-5 shows that W depends on the stress difference between the reservoir and barrier layers, $\Delta\sigma$. However, in the numerical simulations with weak interfaces, the dependence on the stress difference vanishes, thereby showing that accommodation of deformation on the weak interfaces makes the system deviate in its basic parametric sensitivities from a system where the barriers are bonded to the reservoir. Moreover, this observation adds to the weight of evidence that the free-sliding interfaces can significantly impact height growth behavior, in this case by reducing or even eliminating the dependence of maximum opening width on the barrier stress.

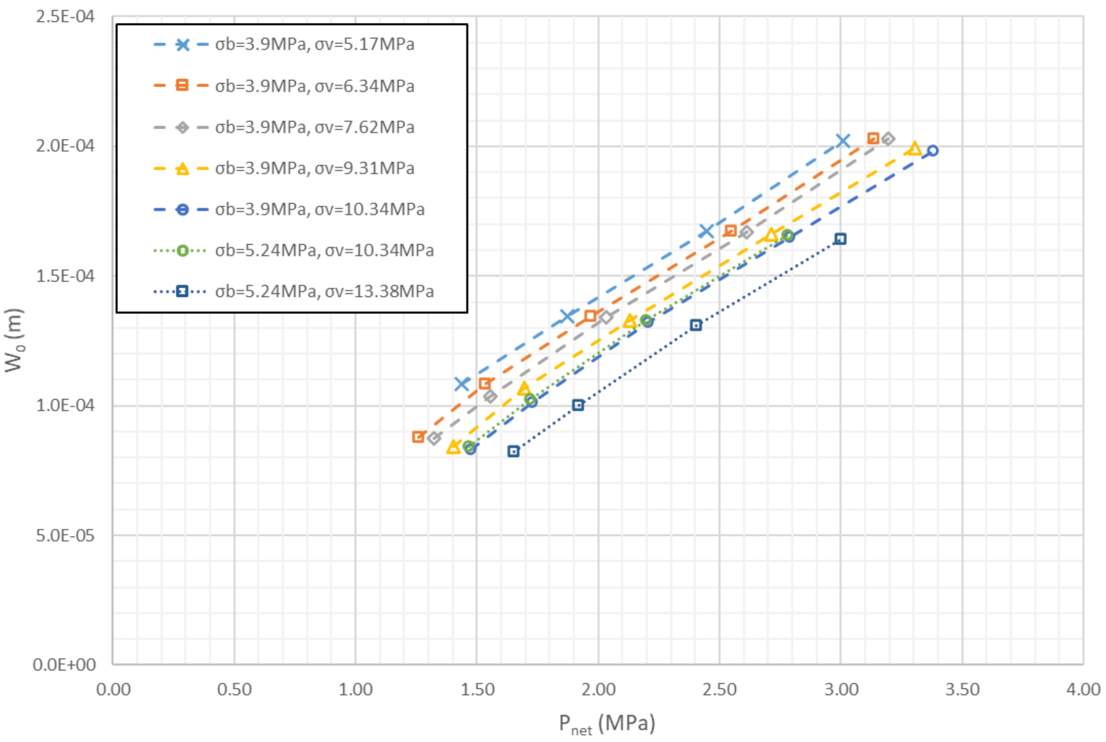

Figure 5-8. The maximum hydraulic fracture width in the reservoir ("reservoir width") W_0 versus net wellbore pressure P_{net} plot for numerical simulations representing PMMA-PMMA laboratory-scale experiments.

In contrast to the hydraulic fracture width in the reservoir ("reservoir width"), the barrier width (W_1) (i.e., the fracture width in the barrier layer at the contact with the reservoir) is highly sensitive to the barrier stress, as shown in Figure 5-9. Additionally, while reservoir width increases with P_{net} with a constant slope, the barrier width changes slope, becoming steeper in these cases when P_{net} equals 2~2.5 MPa. This phenomenon is most likely caused by the initiation of unstable fracture height growth at a similar net pressure value. One can also observe that higher vertical stress ($\sigma_v > 2\sigma_b$) can significantly increase W_1. In contrast, the sensitivity of the barrier width to vertical stress for low vertical stresses ($\sigma_v < 2\sigma_b$) is negligible.

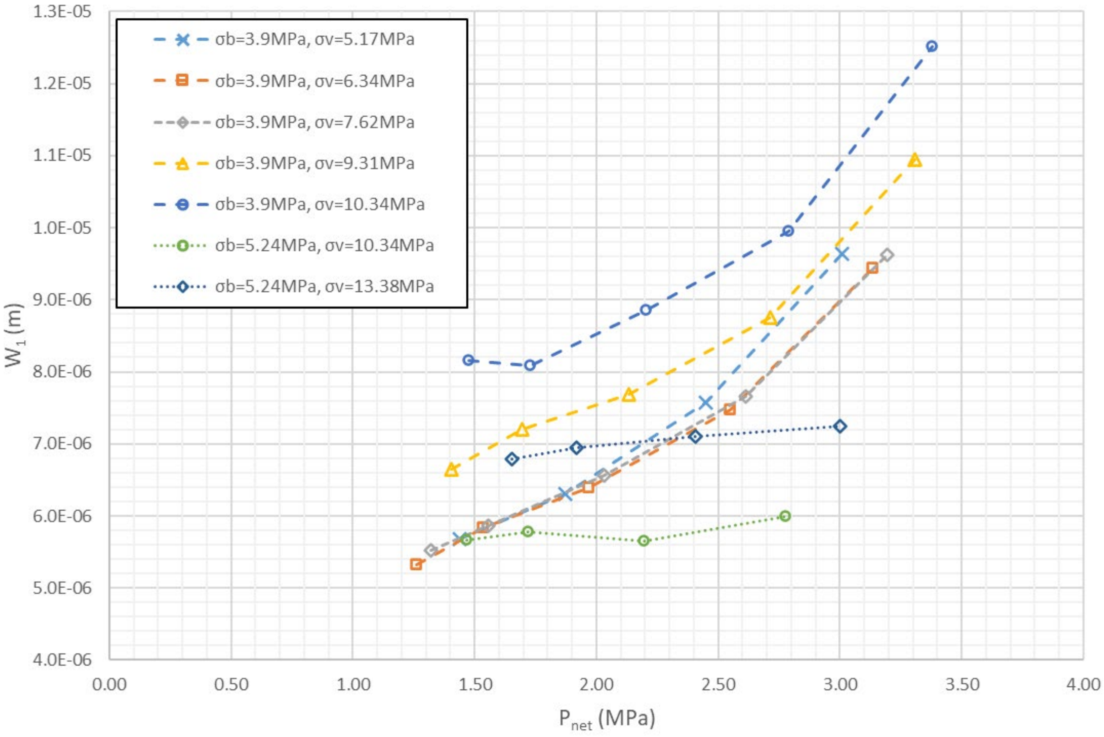

Figure 5-9. The maximum barrier width W_1 versus net wellbore pressure P_{net} plot for simulations based on PMMA-PMMA experiments.

In order to visualize the relative changes of reservoir and barrier width, it is helpful to introduce the fracture width ratio

$$\omega = \frac{W_0}{W_1} \qquad \text{Eq. 5-6}$$

Hence, a large value of ω means the fluid prefers to stay in the reservoir layer. At the same time, a low ratio indicates the fluid prefers to penetrate the barrier layers, thus may potentially promote the fracture height growth.

Figure 5-10 shows the cases with constant σ_b =3.9MPa and σ_r =2.76MPa. First of all, for each set, the ratio ω increases with P_{net} until reaching the peak value at approximately 2.5~2.8 MPa. Meanwhile the slope $d\omega/dP_{net}$ keeps decreasing from positive to negative values. The corresponding critical net pressures $P_{net,c}$ data from lab experiments are indicated by the blue band (i.e., experiments observed transition to unstable height growth when increasing pressure passed through this range). Therefore, the critical net pressures from the lab experiments are found to coincide with the values where there is a change in the slope of ω, as predicted by simulations. Secondly, we can observe from the simulation results that vertical stress negatively correlates with ω. Similar to what we have seen in Figure 5-9, high vertical stress ($\sigma_v > 2\sigma_b$) can reduce the ω more effectively than the low vertical stress ($\sigma_v < 2\sigma_b$).

The remaining simulation sets of the PMMA-PMMA group are shown in Figure 5-11, which illustrates an apparent increase of ω by increasing σ_b from 3.9MPa to 5.24MPa. Then ω is suppressed again by enlarging σ_v from 10.34MPa to 13.38MPa.

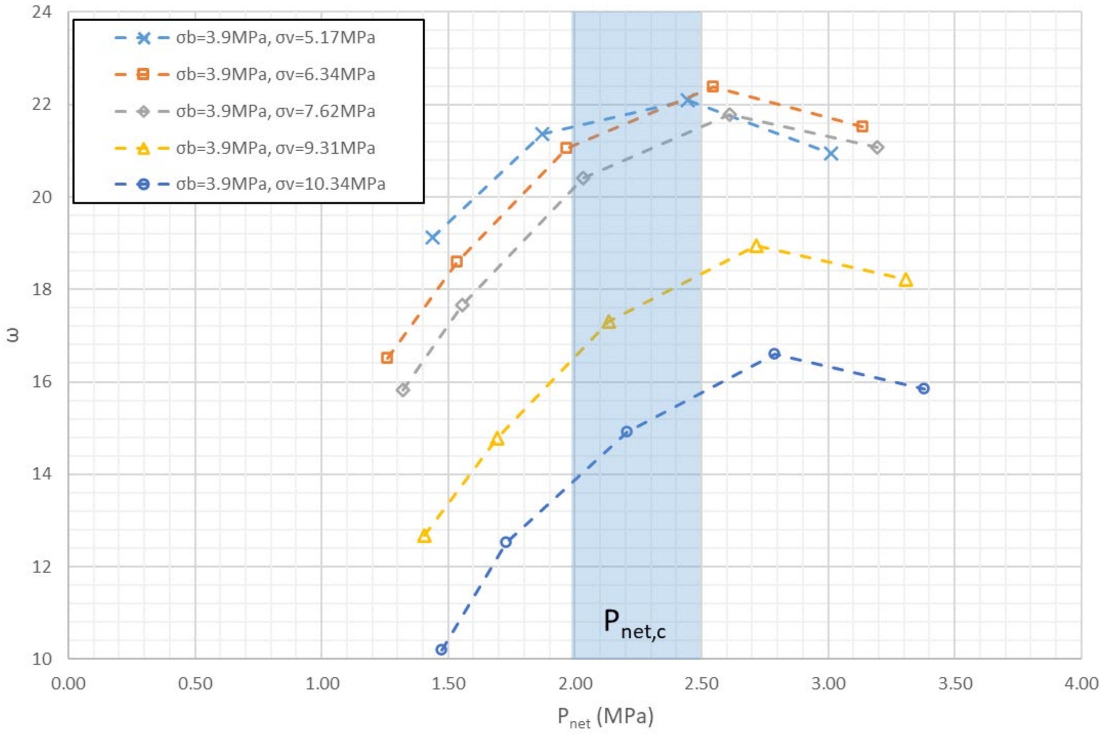

Figure 5-10. The plot of width ratio ω versus P_{net} of PMMA-PMMA group simulations that have σ_b=3.9MPa.

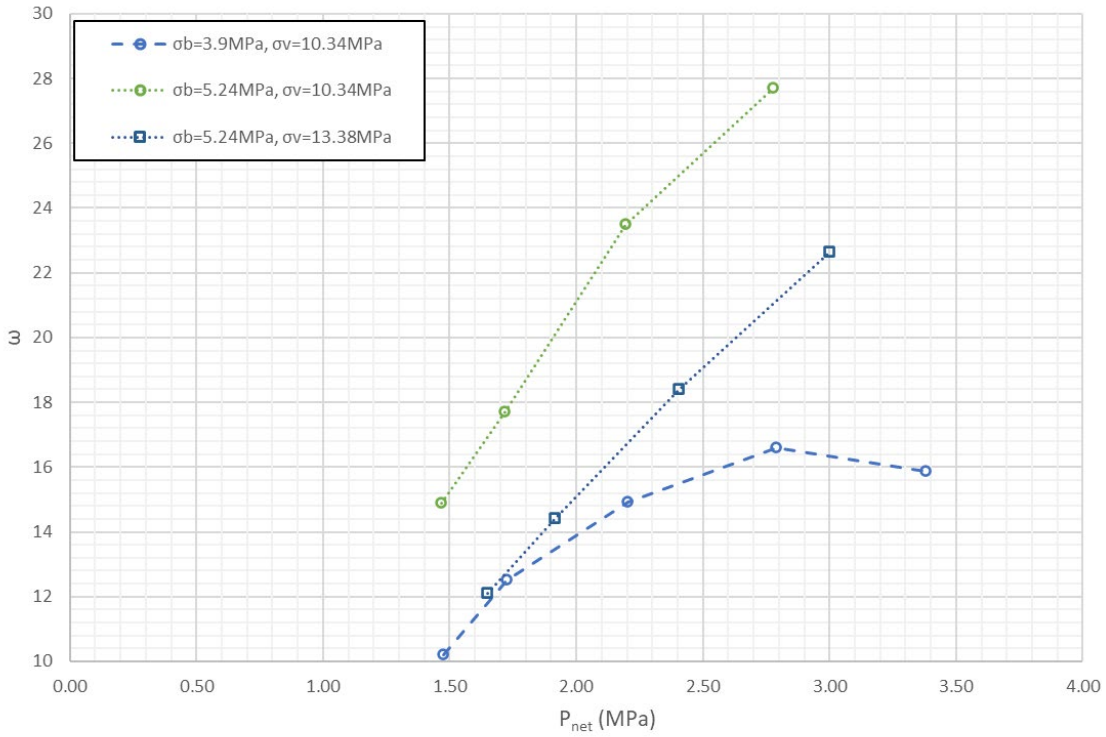

Figure 5-11. The plot of width ratio *ω* versus P_{net} of PMMA-PMMA group simulations shows the impact of boundary stress on *ω*.

5.4 Behavior of the Fracture Height

The complete PMMA-PMMA group λ data is shown in Appendix Table C-2. Figure 5-12 shows the λ versus P_{net} for sets that have σ_b =3.9MPa and σ_r =2.76MPa. The numerical data of each set are open-marked and connected with the dashed line. At the same time, the corresponding experimental data point is indicated with a solid symbol. This comparison shows that the experimental data points are in the ballpark with the XSite predictions (except for the case with σ_v =6.34MPa), which increases the confidence of the numerical simulation by this experimental validation.

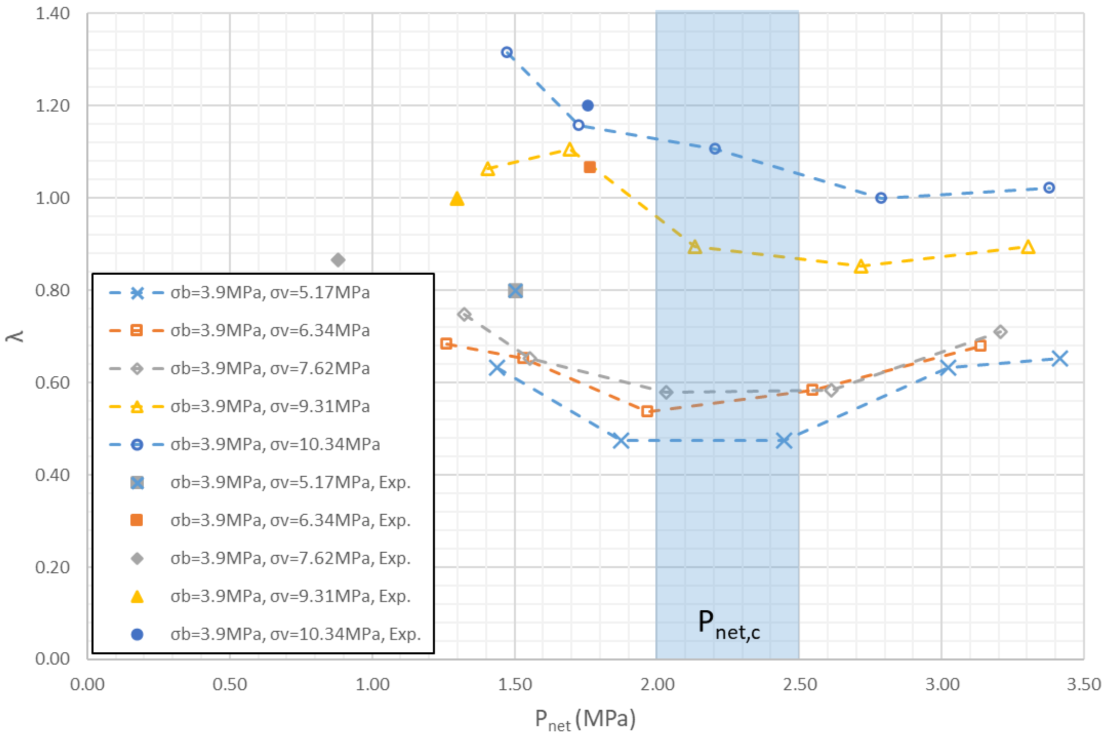

Figure 5-12. The λ versus P_{net} summary plot for the PMMA-PMMA group with fixed horizontal stresses σ_r = 2.76MPa and σ_b=3.9MPa. The solid points represent the experimental measurement, while the open points represent the XSite numerical results.

The transition from stable height growth to rapid (i.e., unstable) height growth that was observed in the experiments is also reflected in the simulations. Figure 5-12 shows that for each set, the height ratio λ will be reduced by increasing the net wellbore pressure until reaching the minimum value at approximately 2.0~2.8 MPa. After that, the λ will increase with P_{net}. In other words, the $d\lambda/dP_{net}$ changes from negative to positive as P_{net} increases. Therefore, similar to the observed slope inflection at the critical pressure for the simulation result for the width ratio (Figure 5-10), the λ versus P_{net} slopes change at the critical pressure range found in the experiments.

The impact of vertical stress on fracture height growth can also be observed in the simulations. Figure 5-12 also shows that similar to the effect on W_1, the vertical stress σ_v can distinctly promote the height growth at high values, while the influence becomes negligible when vertical stress is relatively small. The same conclusion can be found via a different representation of the simulation data, shown in Figure 5-13. Here it is shown that the λ shift from 0.6 ~ 0.9 to 1 ~ 1.3 when the σ_v increases from 10.34. MPa to 13.38 MPa while σ_b =5.24MPa. In the meantime, once the vertical stress is constant, we notice that the λ value drops down once σ_b increases from 4MPa to 5.24 MPa, which indicates that the high barrier confining stress will have a negative effect on the fracture height.

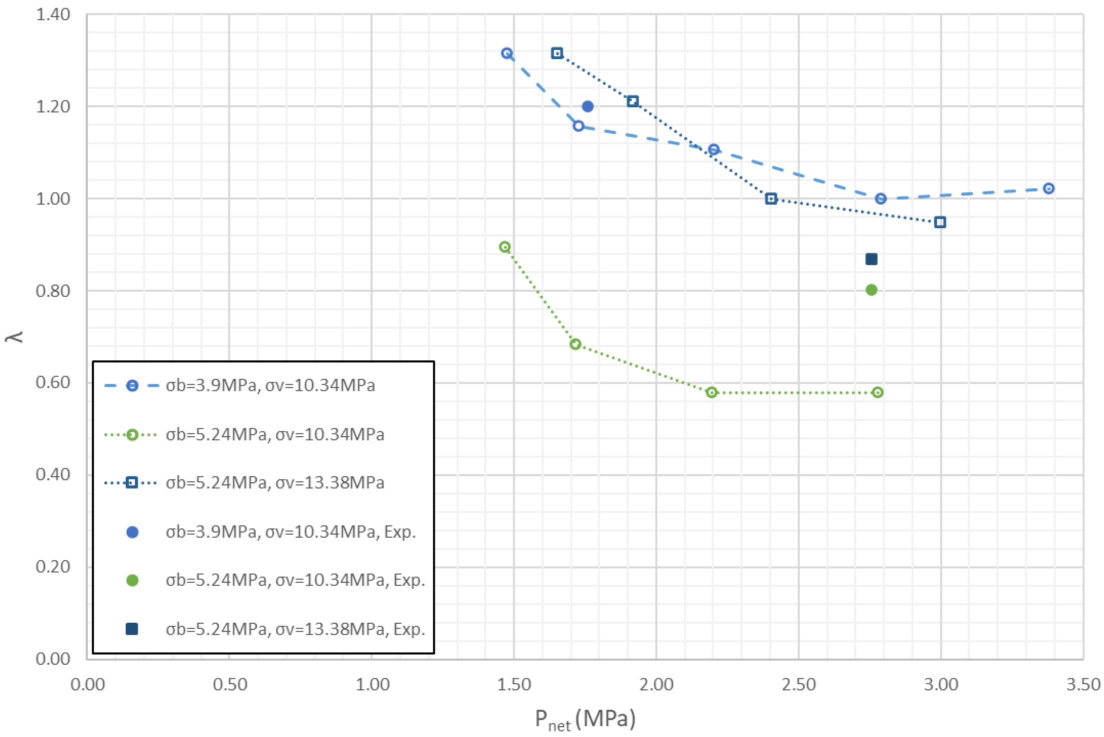

Figure 5-13. The comparison of numerical simulations with fixed horizontal stresses σ_r =2.76MPa and σ_b=5.24MPa indicates that the λ will increase with σ_v. In the meantime, the comparison of numerical tests with fixed horizontal stresses σ_r =2.76MPa and σ_v =10.34MPa indicates the λ will decrease with σ_b increasing. The solid points represent the experimental measurement, while the open points represent the XSite numerical results.

In summary, the simulations corroborate the experimental observation that boundary stresses strongly impact height growth. The simulations allow a detailed view of the mechanisms, particularly from both width and length perspectives. Generally speaking, vertical fracture propagation can be promoted by either decreasing barrier stress or increasing vertical stress. More specifically, high vertical and low barrier stress can lead to a small width ratio ω and a large height ratio λ. Additionally, the simulation results show that both ω and λ can be used as promising indicators for predicting the critical wellbore pressure since it has been proved that the unstable fracture height growth will take place once the ω and λ are approaching their peak and minimum values, respectively.

5.5 Non-Uniform Material Layers

5.5.1 Fracture Width Analysis

The same simulation procedures are applied to the PC-PMMA groups, obtaining this case by simply changing the elastic properties of the layers. The complete width and height data for the PC-PMMA group can be found in Appendix Table C-3 and C-4. First of all, to improve data interpretation, the whole group is divided into three sub-groups based on the boundary confining stresses to study the effect of vertical stress. Figure 5-14 shows the width ratio plots of three sub-groups, whose barrier stresses equal 3.45MPa, 4.14MPa, and 5.52MPa, respectively. Moreover, the integrated plot can be found in Appendix Figure C-1.

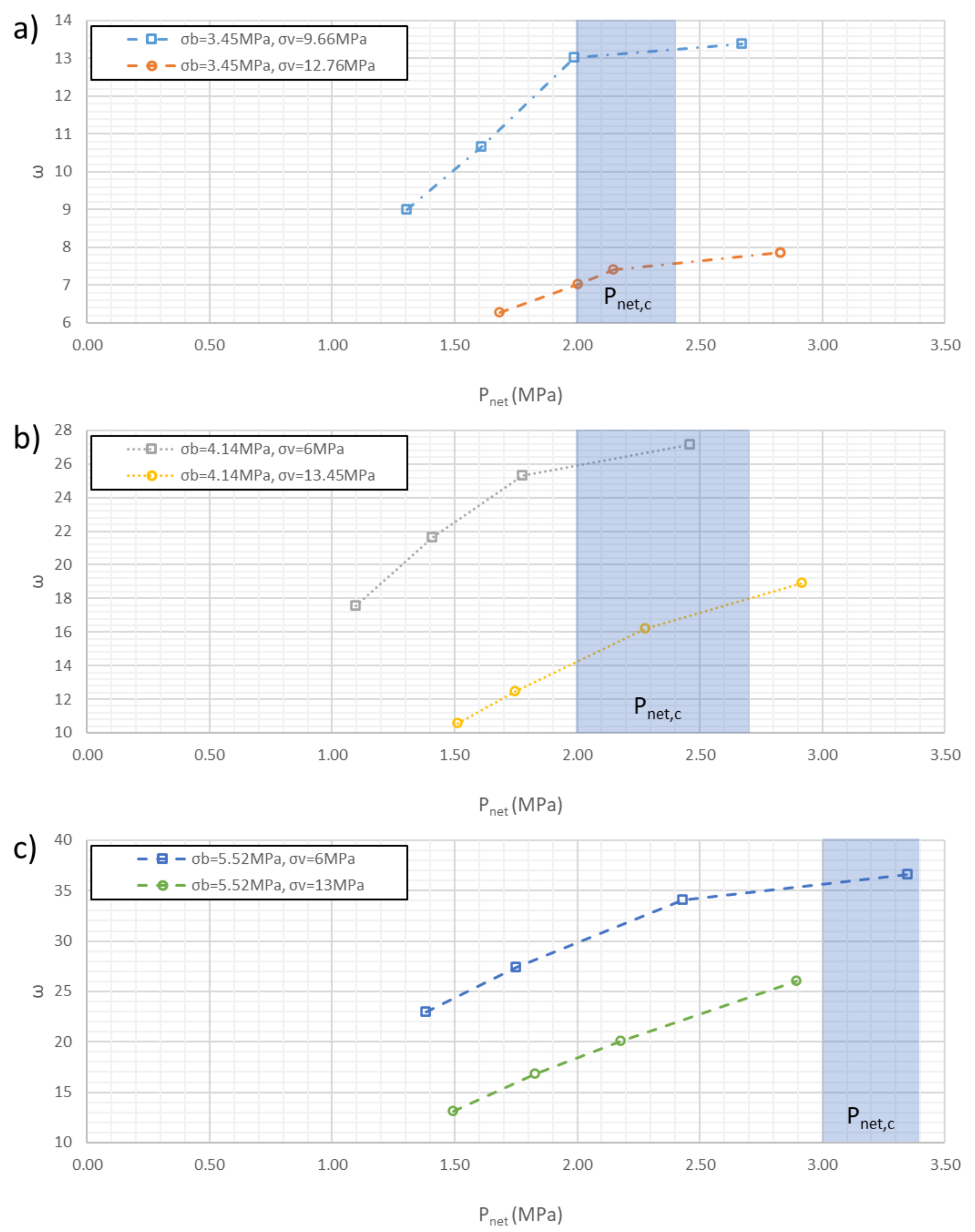

Figure 5-14. The PC-PMMA simulation results of width ratio ω, which are divided into three sub-groups based on barrier stress σ_b equal a) 3.45 MPa, b) 4.13 MPa, and c) 5.52 MPa.

By comparing the sets in each sub-group, one is led to a similar conclusion as with the PMMA-PMMA group. Specifically, it is again found that the high vertical stress can reduce the ω value, thus promoting the fracture propagation vertically. In the meantime, it is once again observed that the pressure zones at which the curve slopes change are also in the ballpark with the critical wellbore pressure measured in the lab experiments. Additionally, all the simulation sets shown in Figure 5-15 have vertical stress of approximately 13MPa. The result indicates a significant increase of ω by enlarging the barrier stress, indicating a similar sensitivity of the width ratio to the barrier stress as observed in the PMMA-PMMA group.

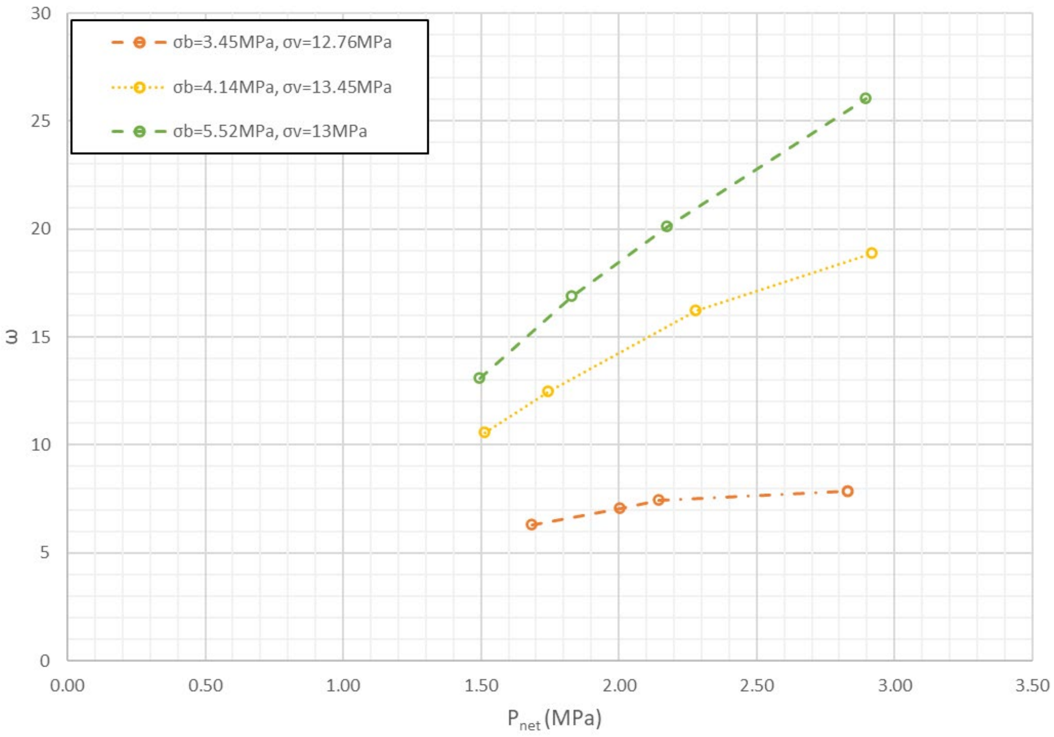

Figure 5-15. The plot shows the ω versus P_{net} relationship for the PC-PMMA tests with vertical stress close to 13MPa.

5.5.2 Fracture Relative Height Analysis

Figure 5-16 illustrates the relationship of λ and P_{net} for three sub-groups, where the groupings are based on the value of the barrier stress. A plot of all results is included in Appendix Figure C-2. Consistent with PMMA-PMMA group data (Figure 5-12), the fracture height is promoted as the vertical stress increases. Additionally, Figure 5-17 shows that the high barrier stress can suppress the fracture height growth, which is consistent with the conclusion as drawn from Figure 5-13. With these consistencies between PC-PMMA cases and PMMA-PMMA cases also comes a contrast. Specifically, it is observed that the increase of wellbore pressure (or injection flow rate) does not affect the fracture height as much as the PMMA-PMMA group.

While the comparison and contrast with other experiments are important, most importantly and strikingly, the simulation results show a high level of consistency with experimental lab data. When combined with previous evidence of consistency between simulations and data, these results confirm the simulator's accuracy for capturing the behavior of hydraulic fracture height growth under these circumstances. By leading to increased confidence in the model, this comparison suggests it could provide an efficient and sufficiently accurate platform for predicting hydraulic fracture height growth at other scales and in a wider range of parameter combinations. In other words, the simulator provides the key link between the laboratory results and applicability of the work to field-scale operations.

With that said, we can also notice that for the two low vertical stress groups shown in Figures 5-16b and c, the height ratio λ changes its slope at a net pressure smaller than the values we observed from the lab. In other words, some divergence between simulations and data occurs when the height growth is very small. This is probably because the vertical stress is too low compared with horizontal stress, which involves a potential T-shape fracture geometry. Thus we may put forward a hypothesis that an additional criterion to detect unstable high growth is that λ satisfies a minimum threshold value (e.g., approximately λ = 0.3 in the PC-PMMA case).

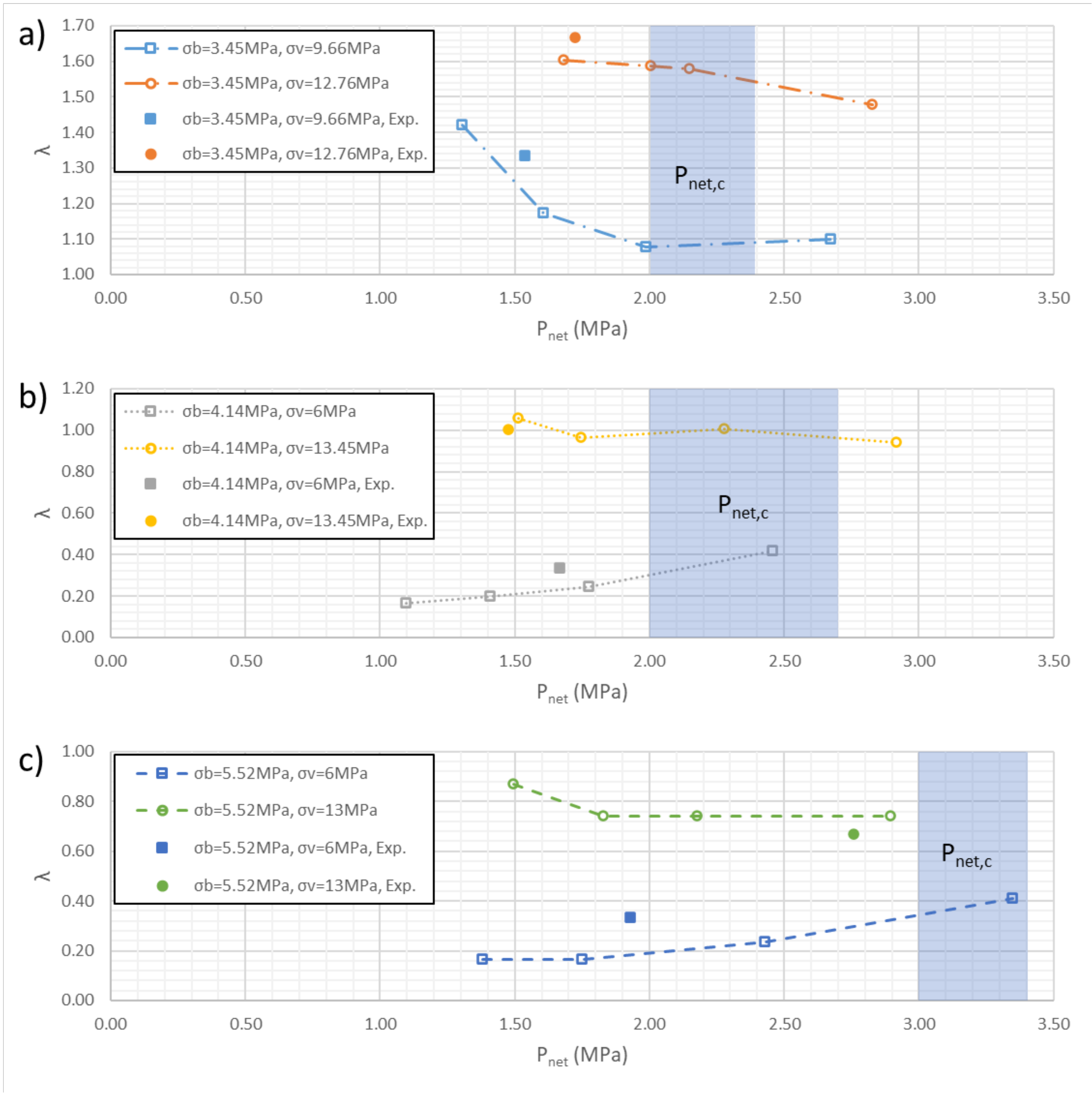

Figure 5-16. PC-PMMA simulation tests are subdivided into three groups based on barrier stress σ_b equals a) 3.45 MPa, b) 4.13 MPa, and c) 5.52 MPa.

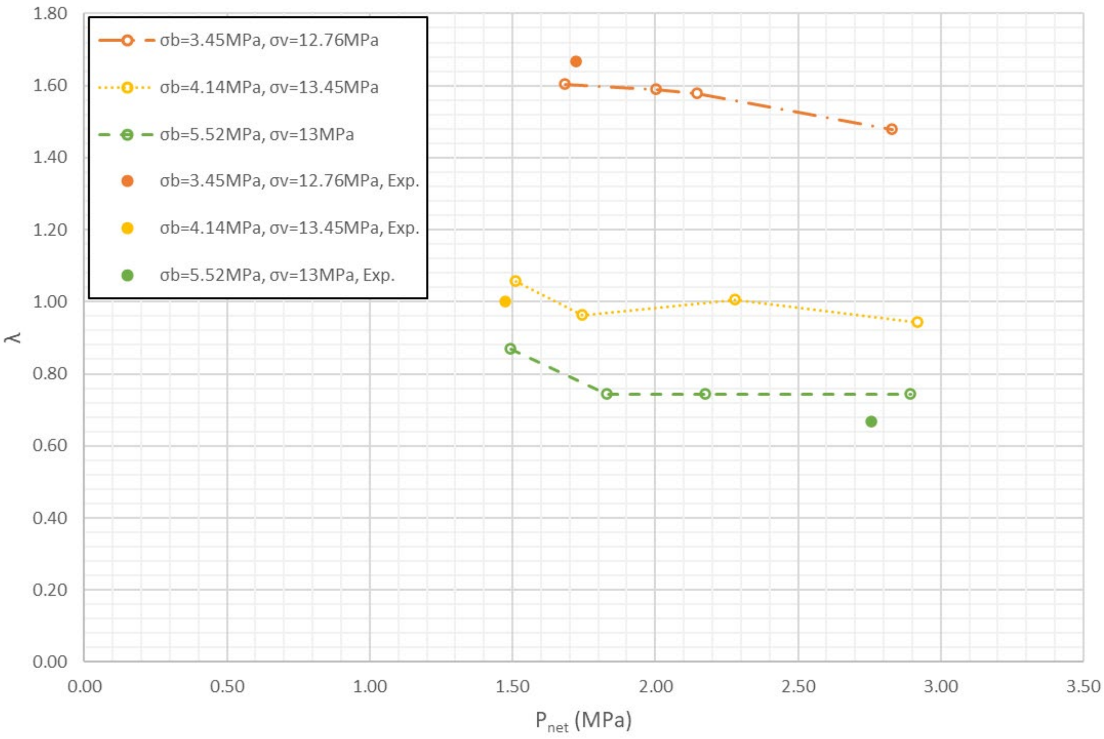

Figure 5-17. The plot shows the λ versus P_{net} relationship for the PC-PMMA tests with vertical stress close to 13MPa.

5.5.3 Comparison of Groups with Various Contrasting Young's Moduli

Having looked in detail at the behavior of the PC-PMMA cases, it is valuable to conclude this section by bringing in the larger Young's modulus contrast group (PP-PMMA) and then elucidating the role of Young's modulus through direct comparisons. To this point, the width ratio plot of three groups with impermeable material combinations is presented in Figure 5-18. Additionally, the vertical height growth comparison plot is shown in Figure 5-19. The corresponding data can be found in Appendix Table C-5 and C-6. Note that the PC-PMMA and PP-PMMA group simulations apply identical confining stresses as the PMMA-PMMA group (#2020-01-15-3). Hence these simulations have no direct experimental counterparts. Validation with experiments has been presented in previous sections, and so this section focuses purely on a numerical parametric study.

Figure 5-18 shows that a high Young's modulus contrast can limit the vertical fracture propagation by effectively increasing the width ratio. This observation from the simulations provides some insight into why a qualitatively similar behavior is observed in the experiments wherein height growth is suppressed by the larger Young's modulus of the barrier layer. Additionally, the PC-PMMA group is closer to the PMMA-PMMA group than the PP-PMMA group, which is again a possible explanatory mechanism for why we do not see a substantial difference between the PC-PMMA and the PMMA-PMMA behavior in the lab experiments. Combining with the observation from Figure 5-19, which confirms that the lower Young's Modulus ratio suppresses the relative height, it is clear that a stiff barrier and soft reservoir can substantially limit the vertical fracture propagation. Hence these simulations corroborate the conclusion drawn from the lab experiments.

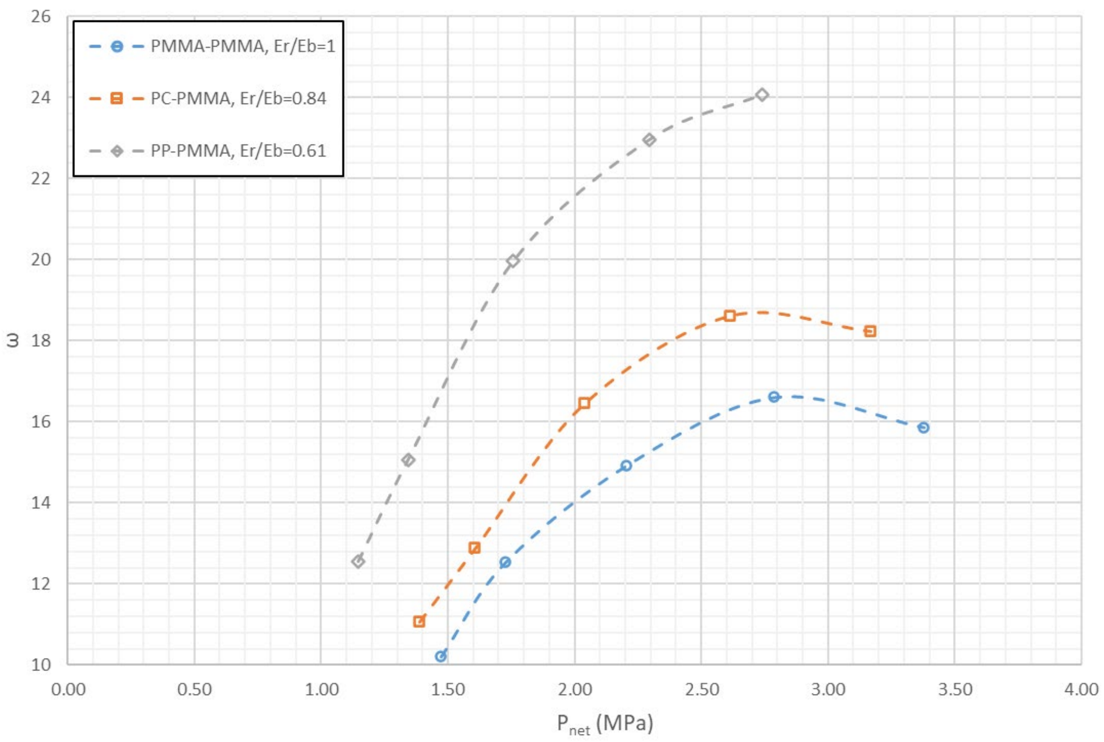

Figure 5-18. The plot shows the *ω* comparison between PMMA-PMMA, PC-PMMA, and PP-PMMA groups with σ_r =2.76MPa, σ_b =3.9MPa, σ_v =10.34MPa.

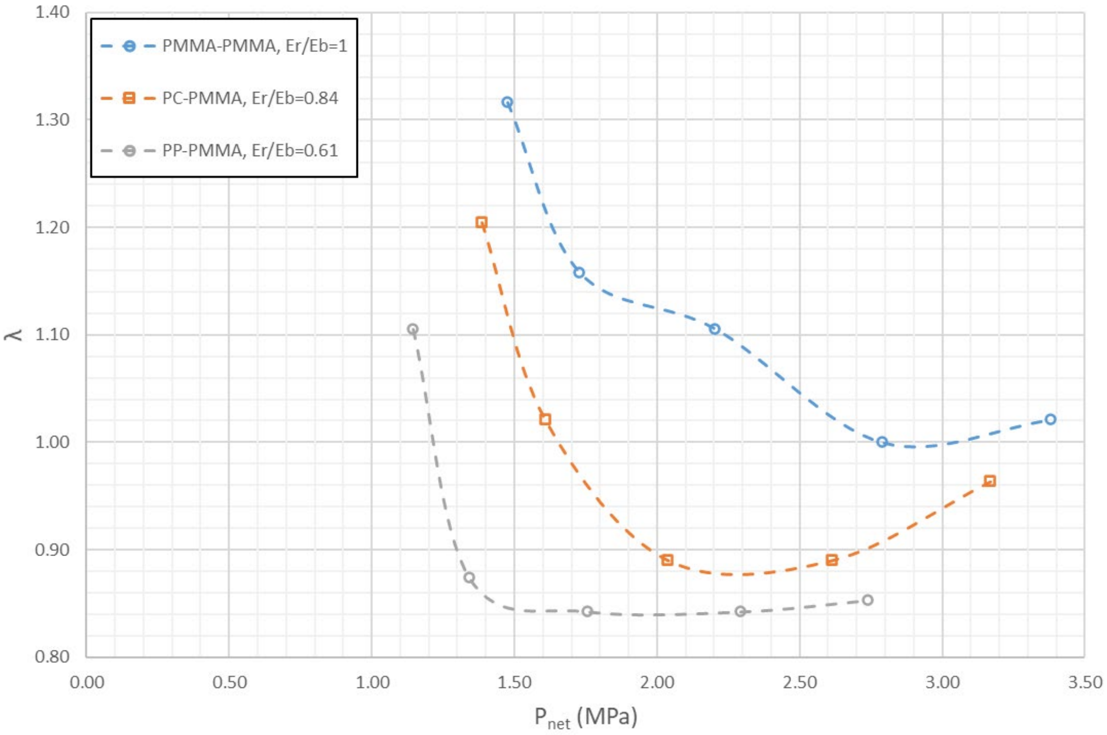

Figure 5-19. The plot shows the λ comparison between PMMA-PMMA, PC-PMMA, and PP-PMMA groups with σ_r =2.76MPa, σ_b =3.9MPa, σ_v =10.34MPa.

6.0 Conclusions

Laboratory experiments and numerical simulations show the substantial impact on hydraulic fracture height growth in layered systems imposed by a combination of weak horizontal interfaces and contrasting elastic properties among layers. Experiments also demonstrate the important role of layer permeability. Because of the close coupling between experimental and numerical studies that extensive consideration of past research to independently consider the roles of stresses and layer properties, this research comprises a uniquely important step forward in elucidating essential mechanisms that govern hydraulic fracture containment and height growth in layered reservoirs.

In the evaluation of experimental and simulation data, three quantities are introduced. These are the critical wellbore pressure P_{fc} (or critical net wellbore pressure $P_{net,c}$), relative height λ (ratio of height in the barrier to the reservoir height), and fracture width ratio ω (ratio of maximum width in the reservoir to the maximum width in the barrier). By comparing how these quantities vary in light of applied stresses and properties of the layers and interfaces between layers, the relative impact of the various conditions on height growth can be quantified. Additionally, it is found that both relative height λ and fracture width ω can be used as indicators to obtain critical wellbore pressure from data. Based on the simulations and experiments, the critical wellbore pressure can be taken as the pressure zone at which these two parameters approach the maximum/minimum values. Furthermore, simulation data shows that sliding of the interfaces greatly reduces the barrier fracture width while increasing the reservoir fracture width compared to the case with solid interfaces (high toughness) and therefore substantially impacts the fracture width ratio.

Broadly speaking, an increased critical wellbore pressure, increased fracture width ratio, and/or decreased relative height is indicated of a reduction or limitation in the hydraulic fracture height growth. Based on the evaluation of how these quantities vary due to changes in the parameters quantifying the conditions imposed in both experiments and simulations, the following conclusions are drawn.

The first main conclusion is that the free-sliding (zero toughness) bedding interfaces can significantly limit fracture height growth. Specifically, it can increase the critical wellbore pressure at which the unstable fracture height growth will occur. This result is broadly consistent with Xing et al. [2018]. However, the demonstration of the stress combinations leading to uncontrolled height growth is new in this research.

Following closely from this point, a second conclusion is that the barrier stress exerts the primary control on height growth. High barrier stress can comprehensively limit the fracture height growth by reducing the fracture height and barrier fracture width while increasing the critical wellbore pressure. This part is not surprising. But what is striking is that it is clearly shown that the critical pressure is above the barrier stress, and because of this, pressure limits set to prevent height growth that based on the classical equilibrium height growth model can be far too conservative for cases where weak interfaces separate the reservoir from the barrier layers.

Thirdly, it is concluded that the impact of vertical stress might be minor compared to the barrier stress. However, it is non-negligible and somewhat complex. This impact of vertical stress is unique to height growth with horizontal interfaces; in a fully bonded domain, the vertical stress is not expected to have an influence. In its details, numerical results show that enlarging vertical stress can slightly increase critical wellbore pressure to limit the fracture height growth. However, in the meantime, it can also dramatically promote fracture height and decrease the width ratio ω. Combined with the experimental observations, increasing vertical stress increases the tendency for fracture height growth.

Fourthly, similar to the barrier stress, a relatively soft reservoir material will lead to a reduced fracture height and increasing width ratio ω, indicating a solid limitation for the fracture height growth. Hence, the mechanical properties of the layers are important, although secondary to the barrier stress in their influence.

Finally, the experiments give an indication of the impact that can be expected for layers with contrasting permeability. As expected, the fluid injection rate required in permeable reservoir cases is significantly higher than in impermeable cases. For high permeability layers, the injection fluid prefers to dissipate into the matrix, which can greatly reduce the fluid injection efficiency. In the meantime, the bedding interfaces can still work as barriers to limit fracture height growth as long as one side is impermeable material. Furthermore, the permeable barrier appears to only affect the fracture/fluid behavior when it penetrates through the interfaces. When this penetration finally happens, the height growth transition can be sudden and so, somewhat surprisingly, it is found that permeability of the barrier layer can extend the range of pressures for which there is containment but can make the transition abrupt so as to reduce the stable height growth period.

Inspired by this research, a couple of interesting topics can be conducted in the future. First, since current research only focuses on the zero-toughness and low friction interfaces, controllable finite toughness and friction characters can be further combined with existing variables. Secondly, current research only covers the geometry of a soft reservoir and stiff barriers. Thus, it is valuable to investigate the fracture propagation behavior once the reservoir material is stiffer than the barrier one. Finally, even though the permeable material laboratory experiments have been conducted macroscopically, it is still necessary to apply a numerical analysis to investigate the microcosmic mechanism of the permeability effect.

Nevertheless, this dissertation research shows a striking consistency between the simulation results and experimental lab data. By leading to increased confidence in the model, this comparison suggests that the lattice-type DEM model could provide an efficient and sufficiently accurate platform for predicting hydraulic fracture height growth at other scales and in a wider range of parameter combinations. In this manner, the simulator provides the key link between the laboratory results and the applicability of the work to field-scale operations.

Appendix A - Elasticity Modulus Effect Study with K_{Ic} Approach

Fett and Munz Theory

To better understand how elasticity modulus will impact the stress intensity K_I, a helpful starting point comes from [Fett & Munz, 1997] theory. A.1-1 shows us the geometry of internal crack propagation between two interfaces.

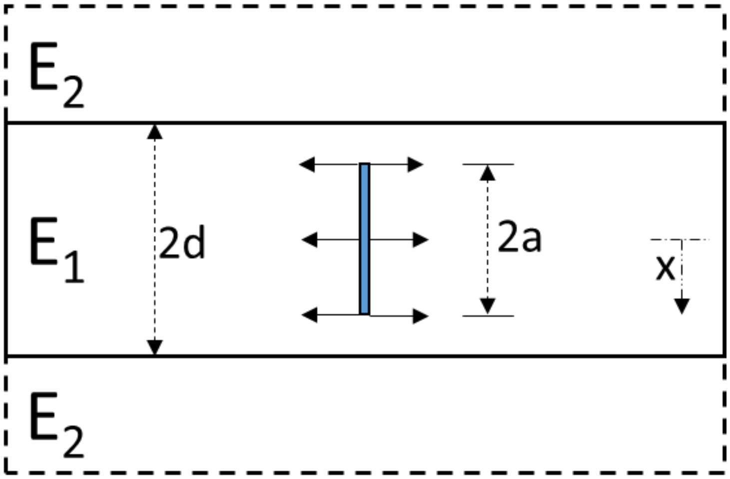

Appendix Figure A-1. Fett and Munz's theory illustrates the geometry with the internal crack propagating between two interfaces.

Based on the theory, the weight function for this geometry can be calculated as

$$h_1 = \frac{2}{\sqrt{\pi\alpha}}\left(\frac{1}{\sqrt{1-\rho^2}} + D_1\sqrt{1-\rho^2}\right), \qquad \rho = x/\alpha \qquad \text{Eq. A.1-1}$$

Where α is the crack half-length and D_1 is a function of α /d ratio and Young's modulus ratio E_1/E_2, as shown in Figure A.1-2a. The stress intensity factor K_I can then be calculated by

$$K_I = \int_0^{\alpha} h_1(x, \alpha)\sigma_y(x)dx \qquad \text{Eq. A.1-2}$$

For cases where E_1/E_2 is less than 1 (the barrier is stiffer than the reservoir), D_1 is negative. Therefore, the stress intensity factor is reduced as the fracture approaches the barrier. To illustrate further, substituting Eq. A.1-1 into A.1-2, for a uniform loading σ along the crack, the K_I can be solved as

$$K_I = \sigma\sqrt{\pi\alpha} \times (1 + \frac{D_1}{2}) \qquad \text{Eq. A.1-3}$$

The K_I for a case with E_1/E_2=0.5 is shown in Figure A.1-2b. Note that the stress is constant and uniformly distributed along the crack in this example. It is taken as a unit value (i.e., σ = 1 MPa) with a unit length for the fracture length (i.e., α = 1m). We can notice that the stress intensity factor keeps enlarging as the tip approaches the interfaces until the peak point with α/d approximately equals 0.9. After that, the SIF starts to decrease. This result indicates that a stiffer barrier can reduce K_I as the hydraulic fracture grows towards it, necessitating a higher pressure to facilitate continued height growth.

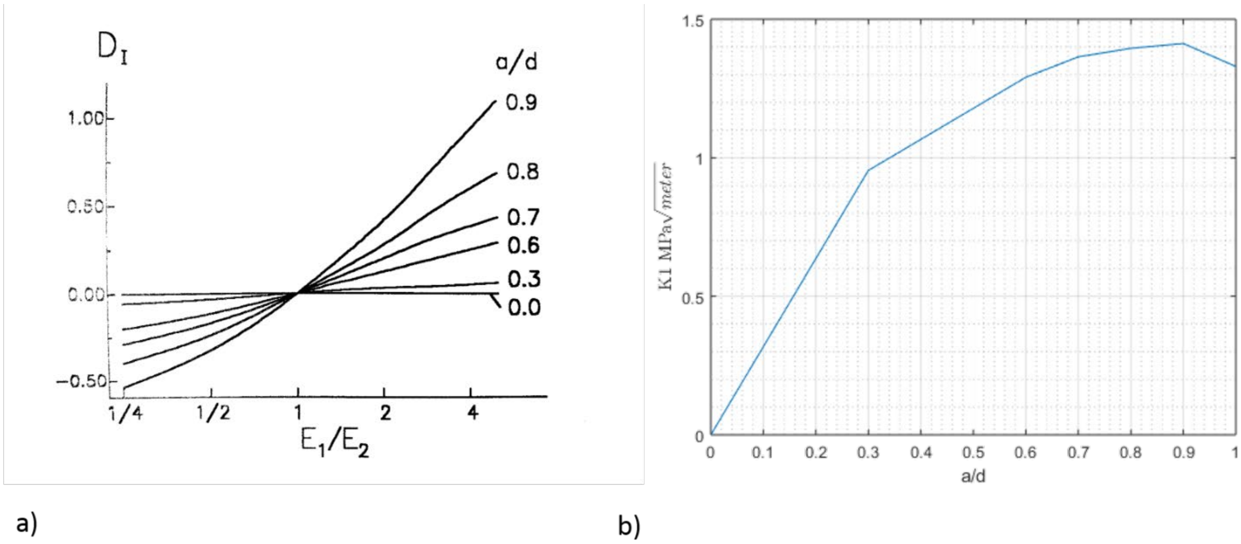

Appendix Figure A-2. a) Dependence of D_I on α /d and E_1/E_2, from [Fett & Munz, 1997]. b) Change of stress intensity factor for the case with a stiffer barrier (E_1/E_2=0.5). 1 MPa constant uniform loading is applied on unit length crack with varying values of the layer thickness *d*.

Franc2D Simulation

Alternatively, we can approach a similar result by applying the Franc2D simulator. Franc2D is a highly interactive program for simulating crack growth in layered structures developed and maintained by Cornell University [Iesulauro, E., 1995]. It uses standard eight or six nodded serendipity elements with quadratic shape functions. The built-in function can statically calculate the stress intensity factor K_I for the crack tip propagation from a low young's modulus (E_1) middle layer into a high young's modulus (E_2) barrier layer. The model geometry that we used was similar to Figure A.1-1. It should be aware that in this scenario, the barrier layer and reservoir layer are strongly bonded, and no free-sliding interfaces (natural fracture) exist, which allows cracking opening or relatively shifting. Since it is symmetric along the vertical direction, only half of it was applied in the model with appropriate boundary conditions. As shown in Figure A.1-3, we can notice that the elasticity contrast has little effect on the K_I value when the crack length is small (or relatively minor to the middle layer thickness). As the crack keeps growing, the plotting curves start to diverge while keeping increment trend. Those stiffer barrier cases (small E_1/E_2) show a smaller K_I value than the uniform material case. Similar to the Fett and Munz result, when the crack tip is close enough to the interface, the K_{Ic} will start to decrease.

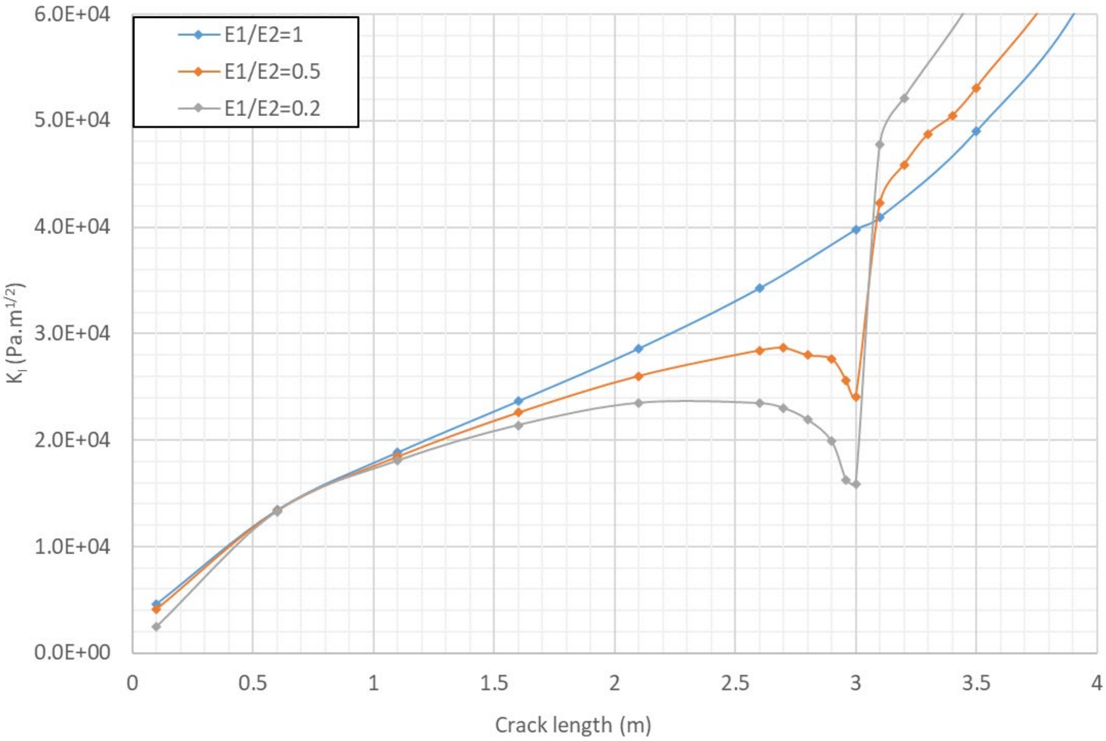

Appendix Figure A-3. Franc2D simulation shows the stress intensity factor K_I vs. cracks length variation under different elasticity modulus contrasts.

Both Fett & Munz and Fran2D solutions are consistent with the fact that the Young's modulus contrast between multiply layers affects the vertical crack propagation. Even with simple model geometry, it is quite promising that a soft reservoir layer and stiff barrier layer scenario will restrict crack propagation into the barrier layer. The crack-tip stress intensity factor will drop while approaching the interface without other conditions changing.

Appendix B - Lab Experimental Data

Appendix B includes all the raw data tables for both permeable and impermeable lab experimental tests. Each table includes the confining stresses (reservoir stress σ_r, barrier stress σ_b, and vertical stress σ_v) applied during experiments and their corresponding critical wellbore pressures P_{fc}. The detailed procedures can be referenced from Chapter 3.

Appendix Table B-1. PMMA-PMMA group experimental result.

PMMA-PMMA (MPa)				
e **=1**	σ_r	σ_b	σ_v	P_{fc}
2019-10-31-1	2.76	3.86	12.72	4.71
2019-11-08-1	2.76	3.89	13.39	5.00
2019-11-18-1	2.76	3.94	6.01	5.30
2020-01-15-1	2.76	3.93	13.01	4.79
2020-01-15-2	2.76	4.06	6.01	5.10
2020-01-15-3	2.76	4.06	9.72	4.79
2020-01-16-1	2.76	5.27	5.73	6.43
2020-01-16-2	2.76	5.27	6.01	6.10

Appendix Table B-2. PC-PMMA group experimental result.

PC-PMMA (MPa)				
e **=0.84**	σ_r	σ_b	σ_v	P_{fc}
2019-03-18-1	2.76	3.41	12.72	4.83
2019-03-19-1	2.76	4.48	13.39	5.52
2019-03-21-1	2.76	5.52	6.01	5.81
2019-03-25-1	2.76	5.67	13.01	6.13
2019-04-02-1	2.76	4.10	6.01	4.78
2019-04-22-1	2.76	3.41	9.72	5.14

Appendix Table B-3. PP-PMMA group experimental result.

PP-PMMA (MPa)				
e =0.61	σ_r	σ_b	σ_v	P_{fc}
2020-02-24-5	2.76	5.42	8.79	8.66
2020-02-24-6	2.76	4.12	9.10	7.53
2020-02-27-1	2.76	5.19	10.62	7.88
2020-02-27-2	2.76	5.29	6.78	8.14
2020-03-03-1	2.76	5.61	12.61	7.89
2020-03-03-2	2.76	5.27	5.44	8.17
2020-03-04-1	2.76	3.92	4.58	6.84
2020-03-04-2	2.76	4.14	5.44	7.86
2020-03-04-3	2.76	4.06	6.03	7.50

Appendix Table B-4. Scioto-PMMA group experimental result.

Scioto-PMMA (MPa)				
	σ_r	σ_b	σ_v	P_{fc}
2019-06-12-3	2.76	4.74	10.49	6.76
2019-06-13-1	2.07	5.81	10.75	6.74
2019-06-14-1	2.07	3.80	10.49	5.93

Appendix Table B-5. PC- Scioto group experimental result.

PC-Scioto (MPa)				
	σ_r	σ_b	σ_v	P_{fc}
2019-06-05-1	2.76	4.32	10.27	13.79
2019-06-06-1	2.76	3.53	10.18	11.03
2019-06-07-1	2.76	5.10	10.01	11.72
2019-06-10-1	2.76	4.08	9.99	12.41

Appendix C - Numerical Simulation Data

Appendix C includes all the raw simulation data tables and complementary figures that are related to Chapters 4 and 5. Specifically, it contains the width ratio ω and relative height λ data for PMMA-PMMA and PC-PMMA groups. Besides, it also includes the data tables used for investigating Young's modulus effect and the completed figures of ω *and* λ for the PC-PMMA group.

Appendix Table C-6. The width data of numerical simulation for the PMMA-PMMA group.

	σ_b=3.9MPa, σ_v=5.17MPa				σ_b=3.9MPa, σ_v=6.34MPa			
Test #	2019-11-08-1				2019-11-18-1			
	P_{net} (MPa)	W_0 (m)	W_1 (m)	W_0/W_1	P_{net} (MPa)	W_0 (m)	W_1 (m)	W_0/W_1
Xsite	1.44	1.09E-04	5.67E-06	19.13	1.26	8.80E-05	5.33E-06	16.51
	1.87	1.35E-04	6.30E-06	21.35	1.53	1.08E-04	5.83E-06	18.58
	2.45	1.67E-04	7.57E-06	22.10	1.97	1.34E-04	6.39E-06	21.04
	3.01	2.02E-04	9.64E-06	20.95	2.55	1.67E-04	7.47E-06	22.39
	3.42	2.22E-04	1.09E-05	20.39	3.14	2.03E-04	9.44E-06	21.51

	σ_b=3.9MPa, σ_v=7.62MPa				σ_b=3.9MPa, σ_v=9.31MPa			
Test #	2020-01-15-2				2020-01-15-1			
	P_{net} (MPa)	W_0 (m)	W_1 (m)	W_0/W_1	P_{net} (MPa)	W_0 (m)	W_1 (m)	W_0/W_1
Xsite	1.32	8.74E-05	5.52E-06	15.82	1.41	8.43E-05	6.65E-06	12.68
	1.55	1.04E-04	5.86E-06	17.65	1.69	1.07E-04	7.21E-06	14.79
	2.03	1.34E-04	6.57E-06	20.40	2.13	1.33E-04	7.68E-06	17.32
	2.61	1.67E-04	7.67E-06	21.78	2.72	1.66E-04	8.76E-06	18.95
	3.20	2.03E-04	9.62E-06	21.08	3.31	1.99E-04	1.09E-05	18.21

	σ_b=3.9MPa, σ_v=10.34MPa				σ_b=5.24MPa, σ_v=10.34MPa			
Test #	2020-01-15-3				2020-01-16-1			
	P_{net} (MPa)	W_0 (m)	W_1 (m)	W_0/W_1	P_{net} (MPa)	W_0 (m)	W_1 (m)	W_0/W_1
Xsite	1.48	8.32E-05	8.15E-06	10.20	1.47	8.43E-05	5.66E-06	14.88
	1.73	1.01E-04	8.09E-06	12.52	1.72	1.02E-04	5.78E-06	17.71
	2.21	1.32E-04	8.86E-06	14.91	2.20	1.33E-04	5.66E-06	23.50
	2.79	1.65E-04	9.95E-06	16.59	2.78	1.66E-04	5.99E-06	27.70
	3.38	1.98E-04	1.25E-05	15.85				

	σ_b=5.24MPa, σ_v=13.38MPa			
Test #	2020-01-16-2			
	P_{net} (MPa)	W_0 (m)	W_1 (m)	W_0/W_1
Xsite	1.65	8.21E-05	6.79E-06	12.10
	1.92	1.00E-04	6.95E-06	14.41
	2.41	1.31E-04	7.10E-06	18.41
	3.00	1.64E-04	7.25E-06	22.63

Appendix Table C-7. The height data of numerical simulation for the PMMA-PMMA group.

Test #	2019-11-08-1			2019-11-18-1			2020-01-15-2		
Stresses(MPa)	σ_r	σ_b	σ_v	σ_r	σ_b	σ_v	σ_r	σ_b	σ_v
	2.76	3.86	5.17	2.76	3.86	6.34	2.76	3.86	7.62
	P_f-σ_r		λ	P_f-σ_r		λ	P_f-σ_r		λ
Lab	1.50		0.80	1.77		1.07	0.88		0.87
Xsite	1.44		0.63	1.26		0.68	1.32		0.75
	1.87		0.47	1.53		0.65	1.55		0.65
	2.45		0.47	1.97		0.54	2.03		0.58
	3.02		0.63	2.55		0.58	2.61		0.58
	3.42		0.65	3.14		0.68	3.21		0.71

Test #	2020-01-15-1			2020-01-15-3			2020-01-16-1		
Stresses(MPa)	σ_r	σ_b	σ_v	σ_r	σ_b	σ_v	σ_r	σ_b	σ_v
	2.76	3.86	9.31	2.76	3.86	10.59	2.76	5.24	10.34
	P_f-σ_r		λ	P_f-σ_r		λ	P_f-σ_r		λ
Lab	1.30		1.00	1.76		1.20	2.76		0.80
Xsite	1.41		1.06	1.48		1.32	1.47		0.89
	1.69		1.11	1.73		1.16	1.72		0.68
	2.13		0.89	2.21		1.11	2.20		0.58
	2.72		0.85	2.79		1.00	2.78		0.58
	3.31		0.89	3.38		1.02			

Test #	2020-01-16-2		
Stresses(MPa)	σ_r	σ_b	σ_v
	2.76	5.28	13.38
	P_f-σ_r		λ
Lab	2.76		0.87
Xsite	1.65		1.32
	1.92		1.21
	2.41		1.00
	3.00		0.95

Appendix Table C-8. The width data of numerical simulation for the PC-PMMA group.

	σ_b=4.14MPa, σ_v=6MPa				σ_b=4.14MPa, σ_v=13.45MPa			
Test #	2019-04-02-1				2019-03-19-1			
	P_{net} (MPa)	W_0 (m)	W_1 (m)	W_0/W_1	P_{net} (MPa)	W_0 (m)	W_1 (m)	W_0/W_1
Xsite	1.10	8.60E-05	4.91E-06	17.54	1.51	8.12E-05	7.67E-06	10.58
	1.41	1.15E-04	5.31E-06	21.61	1.75	9.76E-05	7.83E-06	12.47
	1.78	1.37E-04	5.41E-06	25.31	2.28	1.36E-04	8.42E-06	16.20
	2.46	1.85E-04	6.82E-06	27.14	2.92	1.78E-04	9.43E-06	18.89

	σ_b=3.45MPa, σ_v=9.66MPa				σ_b=3.45MPa, σ_v=12.76MPa			
Test #	2019-04-22-1				2019-03-18-1			
	P_{net} (MPa)	W_0 (m)	W_1 (m)	W_0/W_1	P_{net} (MPa)	W_0 (m)	W_1 (m)	W_0/W_1
Xsite	1.31	8.30E-05	9.22E-06	9.00	1.68	9.48E-05	1.51E-05	6.28
	1.61	9.94E-05	9.32E-06	10.67	2.00	1.19E-04	1.69E-05	7.03
	1.99	1.34E-04	1.03E-05	13.02	2.15	1.28E-04	1.73E-05	7.41
	2.67	1.80E-04	1.34E-05	13.39	2.83	1.75E-04	2.23E-05	7.86

	σ_b=5.52MPa, σ_v=6MPa				σ_b=5.52MPa, σ_v=13MPa			
Test #	2019-03-21-1				2019-03-25-1			
	P_{net} (MPa)	W_0 (m)	W_1 (m)	W_0/W_1	P_{net} (MPa)	W_0 (m)	W_1 (m)	W_0/W_1
Xsite	1.38	1.15E-04	5.02E-06	22.93	1.50	8.19E-05	6.25E-06	13.09
	1.75	1.38E-04	5.04E-06	27.36	1.83	1.11E-04	6.57E-06	16.86
	2.43	1.85E-04	5.43E-06	34.10	2.18	1.31E-04	6.50E-06	20.11
	3.35	2.41E-04	6.58E-06	36.58	2.90	1.81E-04	6.97E-06	26.04

Appendix Table C-9. The height data of numerical simulation for the PC-PMMA group.

Test #	2019-04-22-1			2019-03-18-1			2019-04-02-1		
Stresses(MPa)	σ_r	σ_b	σ_v	σ_r	σ_b	σ_v	σ_r	σ_b	σ_v
	2.76	3.45	9.66	2.76	3.45	12.76	2.76	4.14	6.00
	P_f-σ_r		λ	P_f-σ_r		λ	P_f-σ_r		λ
Lab	1.54		1.33	1.72		1.67	1.67		0.33
Xsite	1.31		1.42	1.68		1.60	1.10		0.17
	1.61		1.17	2.00		1.59	1.41		0.20
	1.99		1.08	2.15		1.58	1.78		0.24
	2.67		1.10	2.83		1.48	2.46		0.42

Test #	2019-03-19-1			2020-01-15-3			2020-01-16-1		
Stresses(MPa)	σ_r	σ_b	σ_v	σ_r	σ_b	σ_v	σ_r	σ_b	σ_v
	2.76	4.14	13.45	2.76	5.52	6.00	2.76	5.52	13.01
	P_f-σ_r		λ	P_f-σ_r		λ	P_f-σ_r		λ
Lab	1.48		1.00	1.93		0.33	2.76		0.67
Xsite	1.51		1.06	1.38		0.17	1.50		0.87
	1.75		0.96	1.75		0.17	1.83		0.74
	2.28		1.01	2.43		0.23	2.18		0.74
	2.92		0.94	3.35		0.41	2.90		0.74

Appendix Table C-10. The ω data for PMMA-PMMA, PC-PMMA, and PP-PMMA groups with σ_r=2.76MPa, σ_b=3.9MPa, σ_v=10.34MPa.

σ_b=3.9MPa, σ_v=10.34MPa											
PMMA-PMMA, E_r/E_b=1				PC-PMMA, E_r/E_b=0.84				PP-PMMA, E_r/E_b=0.61			
P_{net} (MPa)	W_0 (m)	W_1 (m)	W_0/W_1	P_{net} (MPa)	W_0 (m)	W_1 (m)	W_0/W_1	P_{net} (MPa)	W_0 (m)	W_1 (m)	W_0/W_1
1.48	8.32E-05	8.15E-06	10.20	1.39	8.59E-05	7.77E-06	11.05	1.15	8.80E-05	7.01E-06	12.56
1.73	1.01E-04	8.09E-06	12.52	1.61	1.03E-04	7.96E-06	12.88	1.34	1.08E-04	7.16E-06	15.07
2.21	1.32E-04	8.86E-06	14.91	2.04	1.32E-04	8.04E-06	16.44	1.76	1.46E-04	7.29E-06	19.98
2.79	1.65E-04	9.95E-06	16.59	2.61	1.69E-04	9.06E-06	18.61	2.30	1.91E-04	8.34E-06	22.97
3.38	1.98E-04	1.25E-05	15.85	3.17	2.03E-04	1.11E-05	18.23	2.74	2.27E-04	9.43E-06	24.08

Appendix Table C-11. The λ data for PMMA-PMMA, PC-PMMA, and PP-PMMA groups with σ_r=2.76MPa, σ_b=3.9MPa, σ_v=10.34MPa.

σ_r=2.76MPa, σ_b=3.9MPa, σ_v=10.34MPa					
PMMA-PMMA, E_r/E_b=1		PC-PMMA, E_r/E_b=0.84		PP-PMMA, E_r/E_b=0.61	
P_{net}	λ	P_{net}	λ	P_{net}	λ
1.48	1.32	1.39	1.20	1.15	1.11
1.73	1.16	1.61	1.02	1.34	0.87
2.21	1.11	2.04	0.89	1.76	0.84
2.79	1.00	2.61	0.89	2.30	0.84
3.38	1.02	3.17	0.96	2.74	0.85

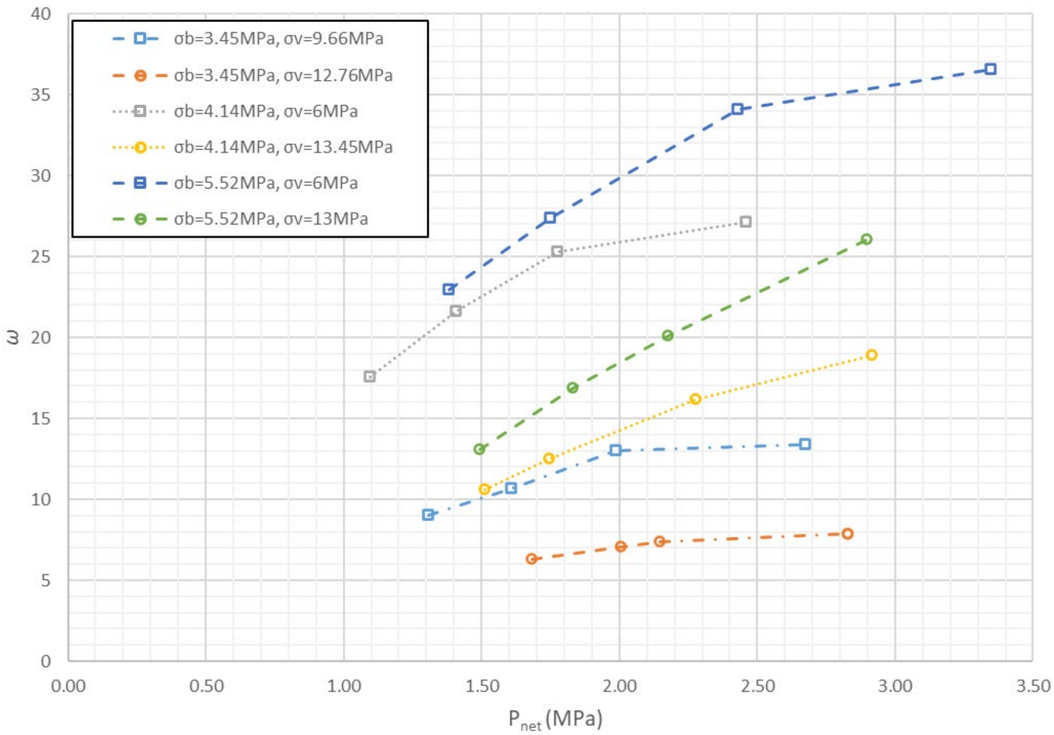

Appendix Figure C-4. The completed width plot of numerical simulation for the PC-PMMA group.

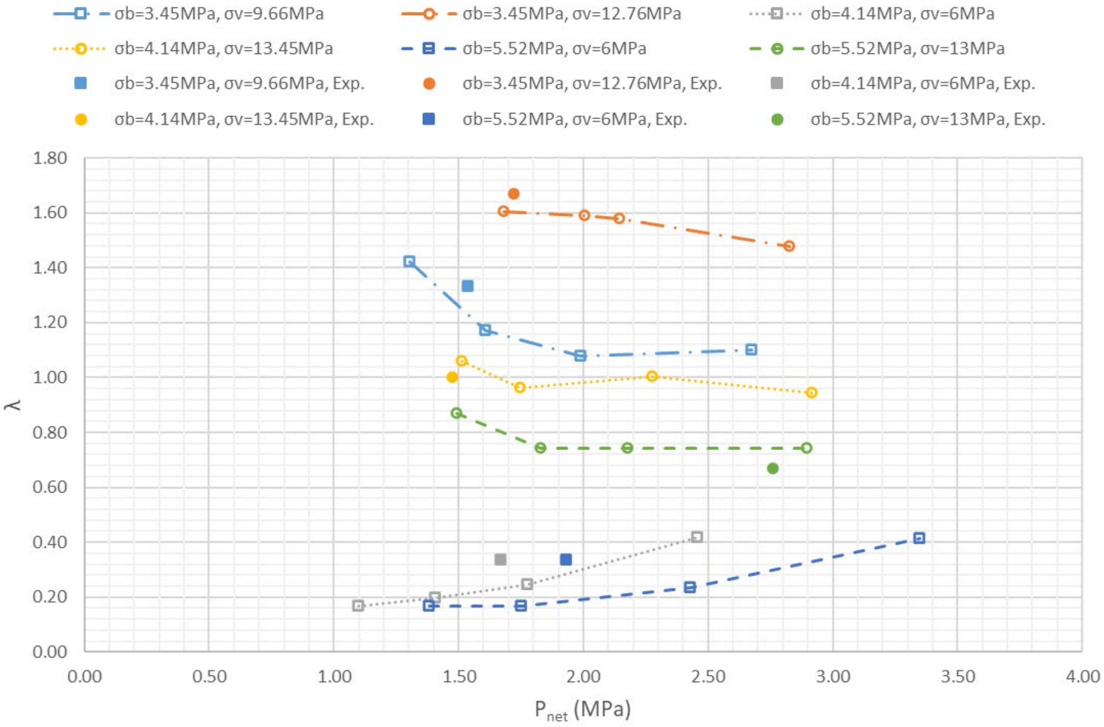

Appendix Figure C-5. The completed height plot of numerical simulation for the PC-PMMA group.

Bibliography

Adachi, J., Siebrits, E. M., Peirce, A., & Desroches, J. (2007). Computer simulation of hydraulic fractures. International Journal of Rock Mechanics and Mining Sciences, 44(5), 739-757.Adachi, J.I. and Peirce, A.P., 2008. Asymptotic analysis of an elasticity equation for a finger-like hydraulic fracture. Journal of Elasticity, 90(1), pp.43-69.

Adachi, J. I., & Peirce, A. P. (2008). Asymptotic analysis of an elasticity equation for a finger-like hydraulic fracture. Journal of Elasticity, 90(1), 43-69.

Adachi, J. I., Detournay, E., & Peirce, A. P. (2010). Analysis of the classical pseudo-3D model for hydraulic fracture with equilibrium height growth across stress barriers. International Journal of Rock Mechanics and Mining Sciences, 47(4), 625-639.

Bennion, D. B., Bennion, D. W., Thomas, F. B., & Bietz, R. F. (1998). Injection water quality-a key factor to successful waterflooding. Journal of Canadian Petroleum Technology, 37(06).

Bunger, A. P., Menand, T., Cruden, A., Zhang, X., & Halls, H. (2013). Analytical predictions for a natural spacing within dyke swarms. Earth and Planetary Science Letters, 375, 270-279.

Cundall, P.A. (2011). Lattice method for modeling brittle, jointed rock, 2nd Int'l FLAC/DEM symposium on continuum and distinct element numerical modeling in geomechanics, 14-16 February, Melbourne, Australia.

Damjanac, B., & Cundall, P.A. (2016). Application of distinct element methods to simulation of hydraulic fracturing in naturally fractured reservoirs. Computers and Geotechnics, 71, 283-294.

Damjanac, B., Detournay, C., & Cundall, P. A. (2016). Application of particle and lattice codes to simulation of hydraulic fracturing. Computational Particle Mechanics, 3(2), 249-261.

Daneshy, A. A. (1978). Hydraulic fracture propagation in layered formations. Society of Petroleum Engineers Journal, 18(01), 33-41.

Daneshy, A. A. (2009). Factors controlling the vertical growth of hydraulic fractures. In SPE Hydraulic fracturing technology conference, January 19-21, 2009, The Woodlands, Texas. SPE-118789.

de Pater, C. J., & Dong, Y. (2009). Fracture containment in soft sands by permeability or strength contrasts. In SPE Hydraulic Fracturing Technology Conference, January 19-21, 2009, The Woodlands, Texas. SPE-119634.

de Souza, A. L. S., Fernandes, P. D., Mendes, R., Rosa, A. J., & Furtado, C. J. A. (2005). The impact of fracture propagation on sweep efficiency during a waterflooding process. In SPE Latin American and Caribbean Petroleum Engineering Conference, June 20-23, 2005, Rio de Janeiro, Brazil. SPE-94704.

Dontsov, E. V., & Peirce, A. P. (2015). An enhanced pseudo-3D model for hydraulic fracturing accounting for viscous height growth, non-local elasticity, and lateral toughness. Engineering Fracture Mechanics, 142, 116-139.

El Rabaa, W., 1987. Hydraulic fracture propagation in the presence of stress variation. SPE Annual Technical Conference and Exhibition, September 27-30, Dallas, Texas. SPE-16898.

Fett, T., & Munz, D. (1997). Stress intensity factors and weight functions (Vol. 1). Computational Mechanics.

Fu, W., Savitski, A. A., & Bunger, A. P. (2018). Analytical criterion predicting the impact of natural fracture strength, height and cemented portion on hydraulic fracture growth. Engineering Fracture Mechanics, 204, 497-516.

Fu, W., Savitski, A. A., Damjanac, B., & Bunger, A. P. (2019). Three-dimensional lattice simulation of hydraulic fracture interaction with natural fractures. Computers and Geotechnics, 107, 214-234.

Gu, H., & Siebrits, E. (2008). Effect of formation modulus contrast on hydraulic fracture height containment. SPE Production & Operations, 23(02), 170-176.

Holder, J., Olson, J. E., & Philip, Z. (2001). Experimental determination of subcritical crack growth parameters in sedimentary rock. Geophysical Research Letters, 28(4), 599-602.

Hustedt, B., Zwarts, D., Bjoerndal, H. P., Al-Masfry, R. A., & van den Hoek, P. J. (2008). Induced fracturing in reservoir simulations: Application of a new coupled simulator to a waterflooding field example. SPE Reservoir Evaluation & Engineering, 11(03), 569-576.

Iesulauro, E. (1995). FRANC2D/L: A crack propagation simulator for plane layered structures. Cornell University, Ithaca, 123.

Jeffrey, R. G., & Bunger, A. (2009). A detailed comparison of experimental and numerical data on hydraulic fracture height growth through stress contrasts. SPE Journal, 14(03), 413-422..

Khristianovic S, Zheltov Y. (1955) Formation of vertical fractures by means of highly viscous fluids. In: Proc 4th world petroleum congress, vol. 2, p. 579– 86.

Montgomery, C.T. and Smith, M.B., 2010. Hydraulic fracturing: History of an enduring technology. Journal of Petroleum Technology, 62(12), pp.26-40.

Nagel, N. B., Sanchez-Nagel, M. A., Zhang, F., Garcia, X., & Lee, B. (2013). Coupled numerical evaluations of the geomechanical interactions between a hydraulic fracture stimulation and a natural fracture system in shale formations. Rock mechanics and rock engineering, 46(3), 581-609.

Nagel, N., Gil, I., Sanchez-Nagel, M., & Damjanac, B. (2011). Simulating hydraulic fracturing in real fractured rocks-overcoming the limits of pseudo3D models. In SPE hydraulic fracturing technology conference. January 24-26, The Woodlands, Texas, USA. SPE-140480.

Ning, L., Shicheng, Z., Yushi, Z., Xinfang, M., Shan, W., & Yinuo, Z. (2018). Experimental analysis of hydraulic fracture growth and acoustic emission response in a layered formation. Rock Mechanics and Rock Engineering, 51(4), 1047-1062..

Noirot, J. C., Van den Hoek, P. J., Zwarts, D., Bjoerndal, H. P., Stewart, G., Drenth, R., ... & Zarafi, A. (2003). Water injection and water flooding under fracturing conditions. In Middle East Oil Show. June 9-12, 2003, Bahrain. SPE-81462.

Nolte, K. G., & Smith, M. B. (1981). Interpretation of fracturing pressures. Journal of Petroleum Technology, 33(09), 1767-1775.

Nolte, K. G., & Economides, M. J. (Eds.). (2000). Reservoir stimulation. John Wiley & Sons..

Nordgren, R. P. (1972). Propagation of a vertical hydraulic fracture. Society of Petroleum Engineers Journal, 12(04), 306-314..

Pagoulatos, A., (2004). Evaluation of multistage triaxial testing on Berea sandstone. Thesis (M.S.)-University of Oklahoma.

Palmer, I. D., & Carroll, H. B. (1983a). Numerical solution for height and elongated hydraulic fractures. In SPE/DOE low permeability gas reservoirs symposium. March 14-16, Denver, Colorado. SPE-11627.

Palmer, I. D., & Carroll, H. B. (1983b). Three-dimensional hydraulic fracture propagation in the presence of stress variations. Society of Petroleum Engineers Journal, 23(06), 870-878..

Peirce, A., & Detournay, E. (2008). An implicit level set method for modeling hydraulically driven fractures. Computer Methods in Applied Mechanics and Engineering, 197(33-40), 2858-2885.

Pierce, M., Cundall, P., Potyondy, D., & Ivars, D. M. (2007). A synthetic rock mass model for jointed rock. In 1st Canada-US Rock Mechanics Symposium. May 27-31, Vancouver, Canada. ARMA-07-042

Perkins, T. K., & Kern, L. R. (1961). Widths of Hydraulic Fractures. JPT: 937-49. Trans., AIME, 222.

Quinn, T. S. (1994). Experimental analysis of permeability barriers to hydraulic fracture propagation. Thesis (Doctoral)-Massachusetts Institute of Technology.

Renshaw, C. E., & Pollard, D. D. (1995). An experimentally verified criterion for propagation across unbounded frictional interfaces in brittle, linear elastic materials. In International journal of rock mechanics and mining sciences & geomechanics abstracts (Vol. 32, No. 3, pp. 237-249). Pergamon.

Savitski, A. A., & Detournay, E. (2002). Propagation of a penny-shaped fluid-driven fracture in an impermeable rock: asymptotic solutions. International journal of solids and structures, 39(26), 6311-6337.

Simonson, E. R., Abou-Sayed, A. S., & Clifton, R. J. (1978). Containment of massive hydraulic fractures. Society of Petroleum Engineers Journal, 18(01), 27-32.

Tada, H., Paris, P. C., & Irwin, G. R. (2000). The stress analysis of crack handbook, The American society of mechanical engineering. New York.

Teufel, L. W., & Clark, J. A. (1984). Hydraulic fracture propagation in layered rock: experimental studies of fracture containment. Society of Petroleum Engineers Journal, 24(01), 19-32.

Thiercelin, M. J., Roegiers, J. C., Boone, T. J., & Ingraffea, A. R. (1987). An investigation of the material parameters that govern the behavior of fractures approaching rock interfaces. In 6th ISRM Congress. August 30-September 3, Montreal, Canada. ISRM-6CONGRESS-1987-049.

Warpinski, N. R., & Teufel, L. W. (1987). Influence of geologic discontinuities on hydraulic fracture propagation (includes associated papers 17011 and 17074). Journal of Petroleum Technology, 39(02), 209-220.

Weng, X. (1992). Incorporation of 2D fluid flow into a pseudo-3D hydraulic fracturing simulator. SPE production engineering, 7(04), 331-337.

Wu, R., Bunger, A. P., Jeffrey, R. G., & Siebrits, E. (2008, June). A comparison of numerical and experimental results of hydraulic fracture growth into a zone of lower confining stress. In The 42nd US rock mechanics symposium (USRMS). June 29-July 2, San Francisco, California. ARMA-08-267.

Xing, P., Yoshioka, K., Adachi, J., El-Fayoumi, A., & Bunger, A. P. (2018a). Laboratory demonstration of hydraulic fracture height growth across weak discontinuitiesHF height growth with weak interfaces. Geophysics, 83(2), MR93-MR105.

Xing, P., Yoshioka, K., Adachi, J., El-Fayoumi, A., Damjanac, B., & Bunger, A. P. (2018b). Lattice simulation of laboratory hydraulic fracture containment in layered reservoirs. Computers and Geotechnics, 100, 62-75.

Zhang, X., Wu, B., Jeffrey, R. G., Connell, L. D., & Zhang, G. (2017). A pseudo-3D model for hydraulic fracture growth in a layered rock. International Journal of Solids and Structures, 115, 208-223.

Zia, H., & Lecampion, B. (2020). PyFrac: A planar 3D hydraulic fracture simulator. Computer Physics Communications, 255, 107368.